NASA-CR-201483

JOINT INSTITUTE FOR AERONAUTICS AND ACOUSTICS

National Aeronautics and
Space Administration
Ames Research Center

Stanford University

JIAA TR 117

EXPERIMENTAL STUDY OF VORTEX BREAKDOWN IN A CYLINDRICAL, SWIRLING FLOW

J. L. Stevens, Z. Z. Celik, B. J. Cantwell, J. M. Lopez

Department of Aeronautics and Astronautics
Stanford University
Stanford, CA 94305

June 1996

Abstract

The stability of a steady, vortical flow in a cylindrical container with one rotating endwall has been experimentally examined to gain insight into the process of vortex breakdown. The dynamics of the flow are governed by the Reynolds number (Re) and the aspect ratio of the cylinder. Re is given by $\Omega R^2/\nu$, where Ω is the speed of rotation of the endwall, R is the cylinder radius, and ν is the kinematic viscosity of the fluid filling the cylinder. The aspect ratio is H/R, where H is the height of the cylinder. Numerical simulation studies disagree whether or not the steady breakdown is stable beyond a critical Reynolds number, Re_c. Previous experimental researches have considered the steady and unsteady flows near Re_c, but have not explored the stability of the steady breakdown structures beyond this value. In this investigation, laser induced fluorescence was utilized to observe both steady and unsteady vortex breakdown at a fixed H/R of 2.5 with Re varying around Re_c. When the Re of a steady flow was slowly increased beyond Re_c, the breakdown structure remained steady even though unsteadiness was possible. In addition, a number of hysteresis events involving the oscillation periods of the unsteady flow were noted. The results show that both steady and unsteady vortex breakdown occur for a limited range of Re above Re_c. Also, with increasing Re, complex flow transformations take place that alter the period at which the unsteady flow oscillates.

Acknowledgements

We would like to thank the many people who have provided invaluable advice and help:

- Wei-Ping Cheng, John Pye, Karl von Ellenrider, and the rest of our research group for providing crucial help with the experiments and analysis.

- The machinists Aldo, Tom, Matt, and Bob for their expertise and help in constructing the experimental apparatus.

- The financial support of NASA's Graduate Student Researcher's Program, and the Joint Institute for Aeronautics and Acoustics.

Table of Contents

List of Tables

List of Figures

Nomenclature

Roman Symbols

AM	amplitude modulation
ASTM	American Society for Testing and Materials
C_1	low-pass filter capacitor
C_2	charge pump capacitor
C_3	lag capacitor
C_4	lead capacitor
cm	centimeter
cS	centiStoke - measure of viscosity 1 cS = 1 mm^2/ sec
D	phase detector pump down signal
D/A	digital to analog converter
DC	direct current
DMM	digital multimeter
e	gain adjustment output

Roman Symbols

e_0	low-pass filter/charge pump output
e_1	lead-lag network output
F(s)	Laplace transform of f(t)
FM	frequency modulation
GPIB	general purpose interface bus
GUI	graphical user interface
H	height of cylinder
HP	Hewlett-Packard
Hz	Hertz - cycles/sec
i_1, i_2	Wheatstone bridge loop currents
in	inch
K	PLL adjustable gain
KAM	Kolmogorov-Arnol'd-Moser
Kohm	kilohm
K_P	plant gain
K_ϕ	phase detector gain
mA	milliAmperes
mg	milligram
min	minute
ml	milliliter
mm	millimeter
mV	milliVolt

Roman Symbols

mW	milliWatt
nm	nanometer
Op amp	operational amplifier
PLL	phase-locked loop
ppm	parts per million
R	radius of cylinder
R_1, R_2, R_3	resistors in Wheatstone bridge for temperature mesurement
RC	resistor-capacitor
Re	Reynolds number
Re_c	critical Reynolds number
R_{P1}	low-pass filter/charge pump resistor
R_{P2}	charge pump resistor
R_{P3}	lag resistor
R_{P4}	lead resistor
R_{P5}	gain input resistor
R_{P6}	gain feedback resistor
rad	radian
rpm	rotations per minute
R_T	thermistor resistance
sec	seconds
t	time variable
T	temperature variable

Roman Symbols

t_{rise}	rise time of plant
T_u	actual temperature minus nominal temperature
U	phase detector pump up signal
V	Volt
v1, v2	computed azimuthal vorticity at R/3, 4H/5 and 2R/3, 4H/5
VCO	voltage-controlled oscillator
vi	virtual instrument (subprogram in LabVIEW)
V_{in}, V_{out}	Wheatstone bridge input and output voltages
w_a	uncertainty in a

Greek Letters

Θ_i	reference phase input to PLL
Θ_o	phase output from encoder
μF	microFarad
μV	microVolt
ν	kinematic viscosity of working fluid
ν_o	nominal viscosity
τ	non-dimensional time, Ωt

Greek Letters

τ_1, τ_2, τ_3	first, second, and third mode periods of oscillation
τ_P	plant time constant
τ_{P1}	charge pump time constant (acts as gain)
τ_{P2}	charge pump time constant (inverse of bandwidth)
τ_{P3}	lag time constant
τ_{P4}	lead time constant
τ_{LP}	low-pass filter time constant
Ω	endwall rotational speed
ω_o	plant output frequency
ω_P	bandwidth of plant

Miscellaneous

°C	degree Centigrade
°K	degree Kelvin
$\frac{\partial a}{\partial b}$	partial differential equation of a with respect to b

Chapter 1

Introduction

1.1 Background

Figure 1-1 depicts a vortex core undergoing breakdown with a recirculation bubble on its axis. The core consists of swirling fluid with an axial velocity imparted to it. When the axial velocity is sufficiently retarded, a stagnation point is created. Several mechanisms may cause the retardation: adverse pressure gradients, diverging nozzles, and friction. In the axisymmetric case, the stagnation point is followed by a recirculation zone and then a second stagnation point which closes the recirculation bubble. The flow can be steady or unsteady as well as three-dimensional. In the latter case, the simple picture depicted in Fig. 1-1 no longer applies and the recirculation bubble can be open to convective exchange of fluid with its surroundings.

The abruptness of the breakdown in the axisymmetric case is explained well by Brown and Lopez[1]. The adverse pressure gradient along the axis allows the core streamlines to diverge causing the axial velocity near the centerline to become slower than the axial velocity outside of the core due to mass conservation (Fig. 1-2). This velocity profile sets up a stronger azimuthal vorticity which opposes the core axial velocity, slowing the core fluid even more. This is a positive feedback system that abruptly turns the core fluid away from the centerline and explains the abruptness of the 'burst'. As the fluid moves away from the centerline, it loses azimuthal velocity in order to conserve angular momentum.

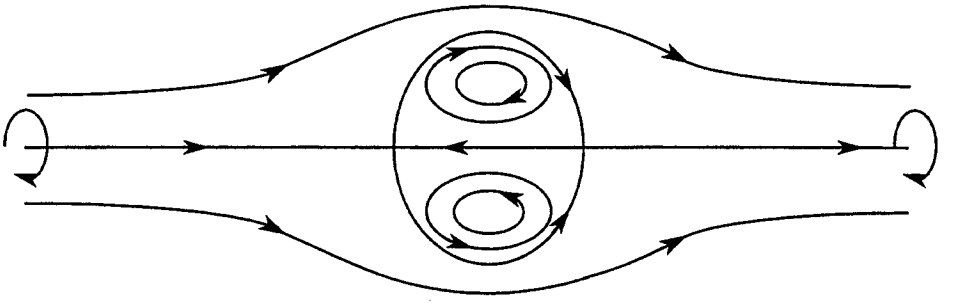

Figure 1-1 Vortex breakdown with recirculation bubbles

The pressure is then sufficient to overcome the centripetal acceleration of the fluid (proportional to azimuthal velocity squared), and turn the flow back towards the centerline, hence, closing the recirculation zone.

1.2 Examples of Vortex Breakdown

Vortex breakdown occurs in many technologically important situations. In some instances, it is encouraged and even necessary. For example, swirl combustors (Fig. 1-3, after Smart and Weber[2]) use the recirculation zone following the breakdown to mix a fuel with oxidizer. The fuel is injected axially and the oxidizer in the surrounding flow mixes through a turbulent, swirling action. In combination with the divergence of the combustion chamber, the swirl causes the vortex tube to burst forming a trailing recirculation zone. Within this zone, the fuel and oxidizer are mixed at rates up to five times higher than rates which occur in a simple jet[3]. The secondary burnout zone is where the rest of the fuel is burned, since not all of the products are consumed in the rich, primary combustion zone.

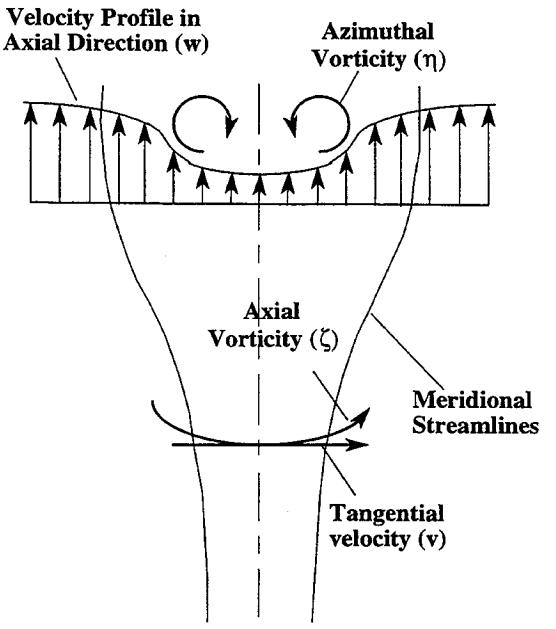

Figure 1-2 Meridional view of axial velocity

Another advantage is that much of the excess heat is carried away by the non-burning, swirling flow. This reduces the heat that the walls of the combustion chamber experience and simplifies the cooling requirements.

Sometimes vortex breakdown can cause a problem and needs to be controlled or removed altogether. When delta-winged aircraft fly at low speeds, they must use a high angle-of-attack to generate sufficient lift. The cost of this lift is an adverse pressure gradient over the upper surface of the wing. When the leading edge vortices encounter the increased pressure, the axial velocity stagnates leading to breakdown (Fig. 1-4 from Van Dyke[4] after H. Werlé *Rech. Aéronaut.* no. 74:23-30, 1960a). This becomes a problem

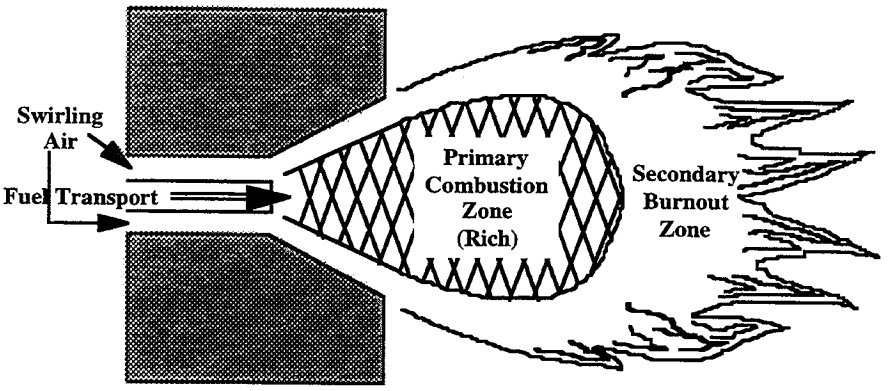

Figure 1-3 Swirl combustor burning pulverized coal

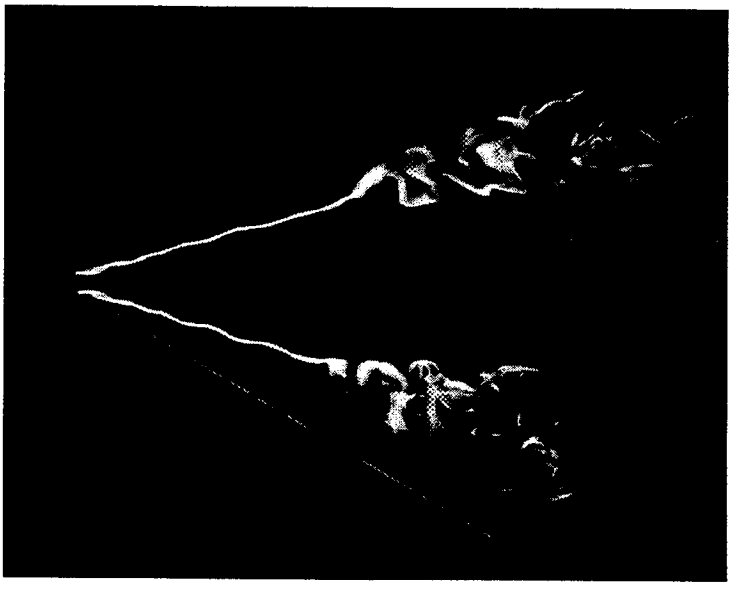

Figure 1-4 Vortex breakdown over a delta wing

during high angle-of-attack maneuvers and also at take-off and landing. The control surfaces become ineffective and this makes management of the aircraft difficult. Also, the aircraft's control surfaces are buffeted by the turbulence caused by the chaotic flow behind the vortex breakdown, further complicating flight control. Moreover, if the breakdowns are asymmetric, the aircraft may be subject to rolling forces.

The wing vortices are manifested by the rolling up of the shear layer over the wing leading edge. The breakdown in these vortices was first studied by Peckham and Atkinson[5]. Harvey[6] points out that large asymmetries in this flow are caused by the continual feeding of vorticity by the shear layer, and shedding at the rear of the wing complicates matters even more. He also determined that the flow is too sensitive to probes, which cause the breakdown to occur unnaturally. More recently, Gursul and Yang[7] have shown the unsteady nature of vortex breakdown location over a delta wing through the use of flow visualization and velocity measurements.

1.3 Vortex Breakdown Studies

1.3.1 Swirling Pipe Flow

Therefore Harvey proposed to study the phenomenon visually in a pipe with guidevanes to create the swirl as shown in Fig. 1-5, which depicts a similar apparatus used by Escudier and Keller[8]. The flow is given an azimuthal component of velocity by the guidevanes, and axial velocity is imparted by gravity and the nozzle located at the end of the center body.

In order to narrow his search for the appropriate values of the governing parameters (swirl velocity controlled by guidevane angle and axial velocity controlled by volume flow rate), Harvey used Squire's[9] criterion for creation of vortex breakdown: the tangent of the swirl angle (tangential velocity / axial velocity) must be between 1.0 and 1.2. Harvey ruled out instability as the cause of vortex breakdown because the recirculation zone,

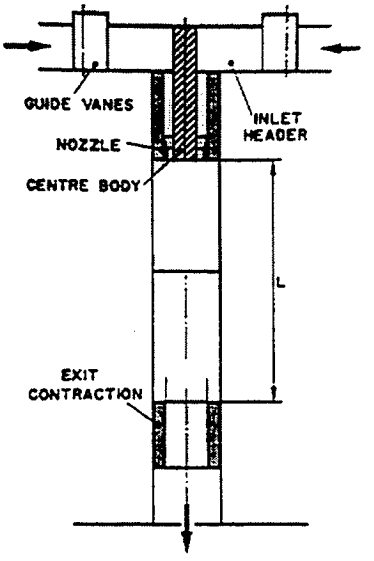

Figure 1-5 Swirl generator

or 'bubble', had a well organized structure and the flow was reversible indicating a 'critical' phenomenon, not an instability. He describes the breakdown as a transition between subcritical and supercritical flows.

As explained by Escudier and Keller[8], the flow is subcritical if the maximum swirl velocity exceeds the maximum axial velocity, which is very similar to Squire's criterion. Two related analogies are shock waves in air and hydraulic-jumps in open-channel flows. Similar to the way a subsonic flow can 'feel' the downstream state, subcritical flows are influenced by the downstream boundary conditions, while supercritical and supersonic flows are independent of these effects. Also, Escudier and Keller pointed out that many investigators have witnessed markedly different flow fields downstream of a vortex breakdown due to the different flow states downstream of the breakdown, and also due to the inherent asymmetries in pipe flow. The asymmetries are a result of the possible asymmetries in the pipe flow entrance and exit velocity profiles[10-13].

According to Escudier[12] the axisymmetric or 'bubble' vortex breakdown is the basic form, and the spiral form is a consequence of instabilities of the bubble form which lead to three dimensionality. Figure 1-6 (from Van Dyke[4] after T. Sarpkaya, *J. Fluid Mech.* 45:545-559, 1971) illustrates the difference between the spiral and bubble types of vortex breakdown. Lambourne and Bryer[14] and Hall[15] observed that in a spiral breakdown, the fluid particles do not spiral although the dye filament does. They inferred that an oscillatory disturbance upstream of the stagnation point sets successive particles on different paths over the stagnant regions. In other words, the dye lines in a spiral breakdown are tracing out streaklines.

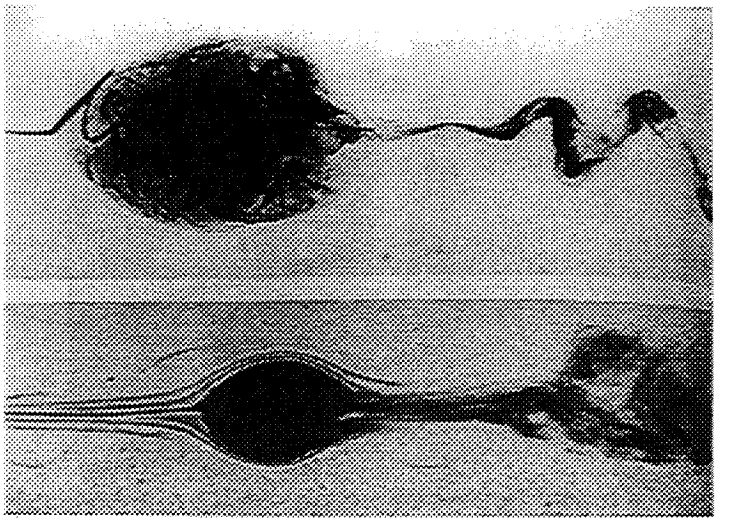

Figure 1-6 Spiral (top) vs. bubble (bottom) breakdown type

1.3.2 Swirling Flow in an Enclosed Cylinder

In order to create a more controlled and nearly axisymmetric vortex flow, an enclosed cylinder is used (Fig. 1-7). The vortex is created by rotating one endwall. An Ekman boundary layer is created on the spinning wall which convects fluid towards the cylinder

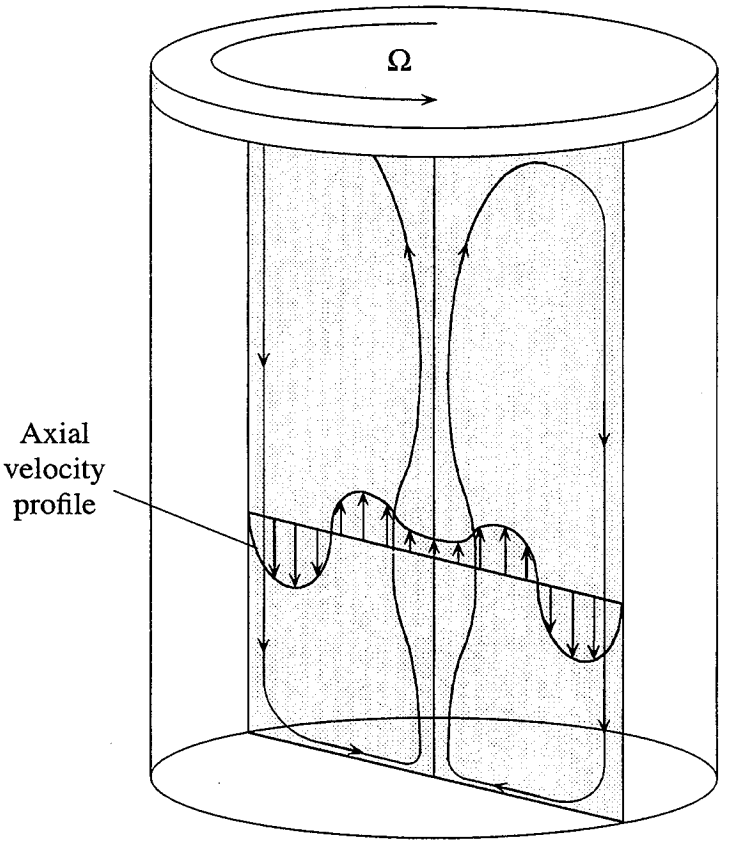

Figure 1-7 Enclosed cylinder flow with a rotating lid

sides. Here the fluid is turned to flow through the Stewartson boundary layer attached to the cylinder walls. Upon reaching the stationary endwall, the fluid is swirled towards the center and picks up azimuthal velocity due to the conservation of angular momentum. Finally the fluid is drawn towards the Ekman layer on the rotating endwall forming a vortex line on the central axis of the cylinder. The momentum deficit at the centerline of the cylinder is attributable to the axial and azimuthal components of velocity imparted to the flow by the boundary layers. In the Eckman layer attached to the spinning disk, the fluid closest to the wall receives more azimuthal velocity than the particles futher away. How-

ever, the greatest radial velocities are imparted to the fluid just outside the boundary layer. As the fluid turns the corner at the edge of the disk, both the azimuthal and axial velocities are retarded by the Stewartson boundary layer along the cylinder wall. Along the lower endwall, the fluid is swirled towards the center and once again, particles in the boundary layer lose velocity. But to conserve angular momentum, the particles just outside of the boundary layer experience an increase in azimuthal velocity. So, once the fluid turns towards the rotating endwall, the fluid on the very axis of the cylinder has lower axial and azimuthal velocities since this fluid is brought out of the boundary layer. Just outside of the boundary layer-vortex core layer, the fluid has more azimuthal and axial velocity. As the disk speed is increased and the disparity between the velocities in the boundary layer and just outside the boundary layer becomes greater, the axial momentum deficit becomes more pronounced. Furthermore, the centripetal acceleration of the particles outside of the central core is enough to overcome the radial pressure gradient, thereby creating bulges in the meridional streamlines along the axis as the fluid particles move to greater radius. As the fluid moves out, it must lose azimuthal velocity to sustain angular momentum. With the corresponding drop in centripetal acceleration, the radial pressure gradient is sufficient to push the fluid back towards the axis, thus creating an isolated bulge in the meridional streamlines. Eventually, the effects of both the momentum deficit (creating stronger and stronger azimuthal vorticity near the axis) and the bulging streamlines cause a stagnation point followed by a recirculation bubble to form on the axis. Further along the axis, this process may repeat itself creating a second and even a third recirculation bubble.

As proof for the basic axisymmetric bubble, two studies have shown how an asymmetric introduction of dye can give the appearance of a spiral even in the enclosed, axisymmetric cylinder flow describe above. Neitzel's[16] numerical calculations show how a very small offset in flow tracer origin (from center to slightly off-center) can transform a bubble region into spiral streaklines. Hourigan, et. al.[17] have gone further to show both numerically and experimentally how "deceptive and illusory flow structures can appear even in

the case of *steady* flow in the *absence* of vortex breakdown." In the experiment, it was noticed that just before the first recirculation bubble appears, the dye line forms a steady spiral streakline even though the dye is injected nominally in the center of the cylinder. But once the critical paramters for the formation of the vortex breakdown had been surpassed, a steady, axisymmetric bubble was formed. The numerical simulations with tracers introduced just slightly off the centerline showed the same spiral form before the bubble developed. Naturally, when the tracers are released exactly on the centerline, no spiral streaklines are evident before the formation of the bubble. This is an important fact to remember when analysis of the results are presented in Chapter 4.

The flow produced inside an enclosed cylinder by the constant rotation of one of its endwalls exhibits a number of complex fluid motions. The dynamics of the flow are determined by two non-dimensional parameters. One of these is the non-dimensional measure of the driving force, the Reynolds number $Re = \Omega R^2/\nu$, where Ω is the speed of rotation of the endwall, R is the radius of the cylinder, and ν is the kinematic viscosity of the fluid. The other governing parameter is the aspect ratio of the cylinder H/R, where H is the height. The earliest published experimental results of the flow exhibiting a region of recirculation on the axis were produced by Vogel[18]. Ronnenberg[19] reported detailed measurements of the entire flow structure for H/R = 1.59 and Re = 1580. Escudier[11] extended Vogel's results and created a stability diagram in H/R, Re - space defining regions of one, two and three breakdown regions, and observed two 'stability' limits (Fig. 1-8). By stable, Escudier refers to the existence of a steady flow. When the steady flow is not stable, it is transformed into an unsteady flow. This unsteadiness is characterized by an oscillation in the upstream stagnation point of the breakdown region, and a stretching out from the core and a folding towards the rotating endwall of the bubbles. In reality, the unsteadiness is apparent in the total flow field with oscillations in velocities, vorticities, etc. However, in visualizations of the flow, the most readily observed indication of the periodic flow is the deformation of the central structure.

There have been numerous computational studies of this flow.[1,13,16,17,20-28] Most of these researchers report numerical simulations based on the axisymmetric Navier-Stokes equations that generally agree with the results obtained by Escudier. The advantage of numerical simulations over experimental data is the amount of detail available for study. In an experimental investigation, it is difficult to measure the desired quantities without disturbing the flow, while a numerical simulation provides very detailed data. However, numerical calculations are always limited to a certain level of numerical accuracy. In the case of an unsteady or unstable flow, the time required for an instability to develop may exceed the time for which the computation can be carried out. However, no matter what the flow, an experiment develops at real time and sampling rates allow the compilation of large amounts of data in a short period of time. Nevertheless, numerical simulations allow the creation of perfect boundary conditions which, at today's current state of machine precision, can never be reproduced flawlessly in a physical apparatus. Therefore, computational shcemes and physical experiments must go hand in hand, playing off each other's advantages to truly begin to understand the complexities evident in nearly all fluid flows.

After validating their simulations using Escudier's results, Brown and Lopez[1] went on to study the vortex breakdown in more detail. The numerical simulation results show that the bulges along the axis are initiated well downstream of the viscous, endwall boundary layer, and are associated with a change in sign of the azimuthal component of vorticity. This suggests that the breakdown characteristics are related to the total head and angular momentum imparted to the flow by the Ekman boundary layer attached to the rotating disk. Upstream of the breakdown, angular momentum is conserved on the stream surfaces. As the fluid moves radially outward around the breakdown, it gains angular momentum, and as it turns back towards the centerline downstream of the bubble, some of the angular momentum is lost. In the region downstream of the breakdown, the flow corresponds to an essentially solid-body rotation of the fluid. Therefore, the breakdown behaves as a transition region from concentrated vortical flow to solid-body rotation.

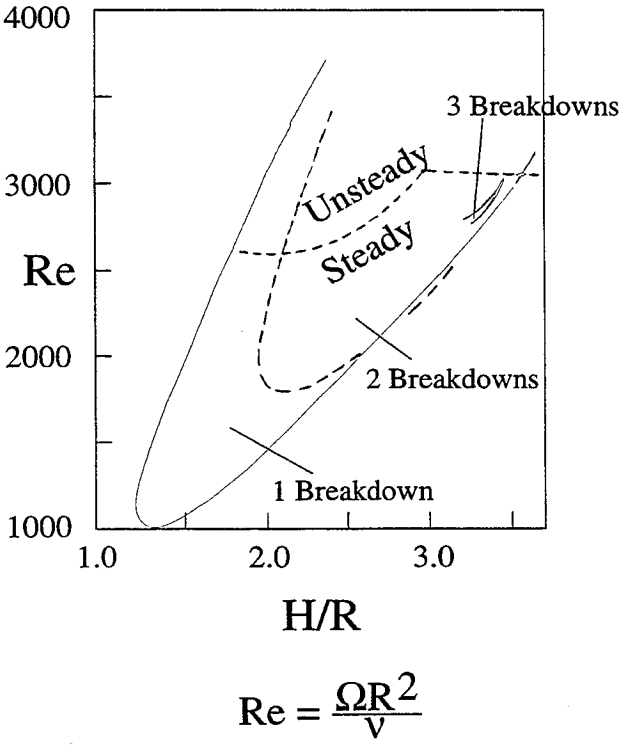

Figure 1-8 Escudier's stability diagram

1.4 Outline of Current Work

The present study has been modeled after the studies of Escudier with the exception of disk placement and motor control. The disk is located above the test fluid rather than below as in Escudier's setup. The motor speed can be changed in nearly infinitesimal increments of rotations-per-minute (rpm) instead of the much coarser adjustment of 1 rpm obtained by Escudier (§ 2.4.1). With a step of 1 rpm and assuming Escudier's maximum viscosity of 60 centi-Stokes (cS), the step in Re is about 16. This is a large jump which, when carried out near an instability boundary, can be considered to perturb the flow sufficiently to destabilize the steady flow, thereby causing the stable unsteady flow to occur.

The most popular view[23,25,27,28] has been that the onset of time-dependence is via a supercritical Hopf bifurcation, where at a critical value of Re, dependent upon the aspect ratio H/R, the steady solution branch loses stability to a time periodic solution branch. For example, Tsitverblit[25], using a combination of perturbation theory and numerical analysis, reports the existence of a steady solution branch reaching into the unsteady region of the flow. The steady solutions were successfully continued into the region where only non-steady flows had been observed in experimental and time-dependent numerical studies. Although Tsitverblit cannot detect a Hopf bifurcation in this continuation analysis, he claims it exists as proven by simulations of the stability of the computed steady solutions with an imposed initial disturbance. The flow did not converge to steady state as it approached Escudier's critical boundary, but became oscillatory. Therefore, Tsitverblit concluded that a Hopf bifurcation had been reached.

Numerical evidence to the contrary, for H/R = 2.5, was recently presented by Lopez and Perry.[24] The steady solutions co-existing with the periodic solutions were found by Lopez and Perry using the time-average of a periodic solution as the initial condition for a time-dependent calculation at the same values of (Re, H/R). A more in-depth study by Lopez[26] also confirms the co-existence of a stable, steady branch and a stable, unsteady branch. The unsteady branch originates from a turning point bifurcation. Lopez claims that Tsitverblit did not observe the stable, steady branch because the initial conditions used were outside the 'basin of attraction' of the steady solutions. There are other problems with the numerical study done by Tsitverblit: coarse spatial resolution and the use of a first-order time stepping algorithm.

The determination of the stability nature of equilibria, such as that of the steady solution branch in the cylindrical flow, is a non-trivial matter. The equilibrium solution is not known analytically, but rather in terms of an equilibrium state of a discrete system which approximates the continuous system. A proper linear stability analysis of the steady solution needs to be done to see if the steady flow is unstable to time-periodic perturbations,

i.e. linearization about the steady solution and checking if there are any eigenvalues with a positive real part and a non-zero imaginary part. A similar, but very detailed analysis for bifurcating Taylor-Couette flow has been carried out by Benjamin.[29,30] More details of this work are brought out and related to current results below and in § 5.2. It has been claimed by Lopez[26] that the unsteady branch is the only axisymmetric flow to be expected in any physical experiment as the basin of attraction of the steady branch is so small. A main focus of this experimental investigation is to examine the nature of the flow in the neighborhood of the bifurcation at H/R = 2.5.

For H/R = 2.5, Lopez[26] monitored the maximum azimuthal vorticity as Re was slowly increased (Fig. 1-9). At a Re ≈ 2669.5, he discovered a turning point bifurcation that produced the stable, unsteady branch that coexists with the stable, steady branch. The unsteady branch is represented by the lower curve which is the value of the time-averaged maximum azimuthal vorticity of the flow. The steady branch is the continuous curve that extends from a Re of zero to approximately 3700. To the right of the graph are three insets that schematically depict several possible forms the bifurcation point can take. The top inset is the turning point bifurcation that represents the event described by Lopez: the steady branch remains stable with increasing Re and the unsteady branch exists as a disjointed solution with a stable and an unstable part represented by the dashed curve. The unstable flow is never realized in numerical simulations or experiments since both naturally converge to either of the stable branches. As described by Benjamin[29], the bifurcation diagram can go through a transformation depending on the symmetry, disturbances and imperfections inherent in the flow. The middle inset is the Hopf, or pitchfork, bifurcation. As Tsitverblit finds, the steady solution becomes unstable at the critical Re and the flow necessarily becomes unsteady. The third inset is the midpoint between the turning and pitchfork bifurcations. The fold in the steady, or primary, solution is seen as hysteresis between two continuous branches of the same steady flow. For instance, if 'A' were a measure of maximum azimuthal vorticity as Lopez uses, then with increasing Re, the value of

azimuthal vorticity would discontinuously change at the bottom of the s-curve as the solution jumped to the upper continuous, stable steady branch. A similar discontinuity would be experienced as the Re was lowered past the upper part of the s-curve, but occurring at a lower Re.

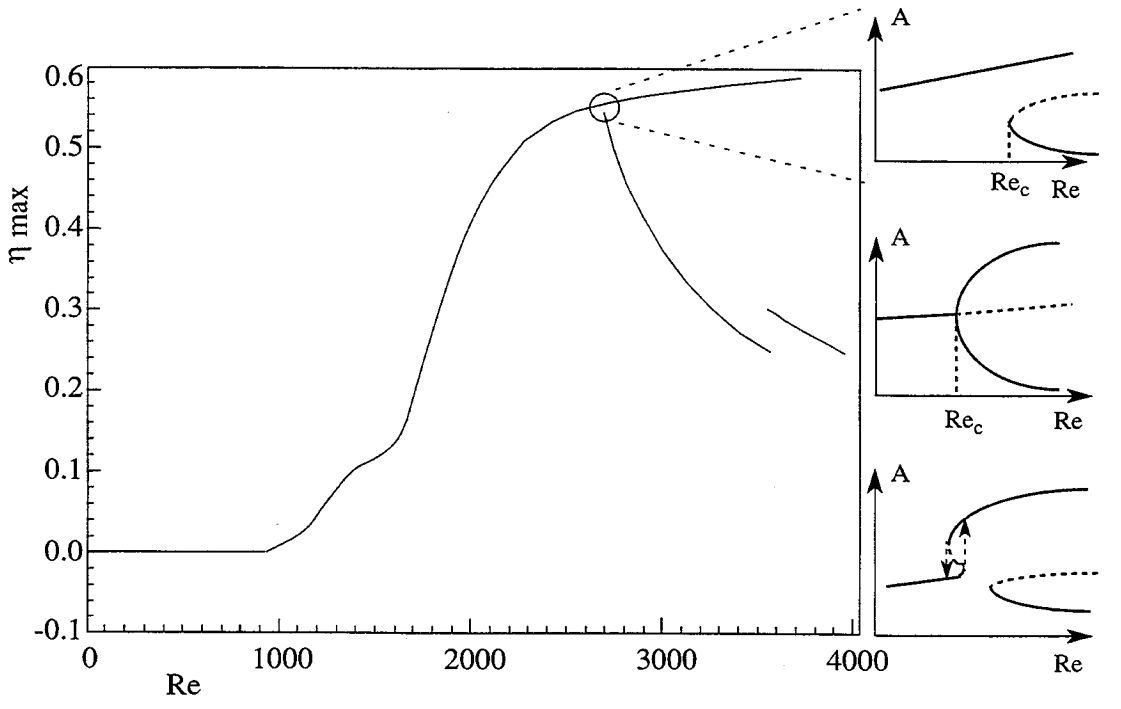

Figure 1-9 Bifurcation of solutions

1.5 Summary of Experiments

1.5.1 Continuation of the Steady Flow

In order to evaluate the numerical studies, a routine was developed that shows the match between previous experimental and numerical simulation characteristics with the characteristics of the current apparatus. All comparisons are done with H/R = 2.5. The first test was to track the development of the initial breakdown, and then match the occurrence of two breakdowns and their subsequent development.

To investigate the oscillatory behavior, the Re is increased through Escudier's critical point. Upon reaching a Re sufficiently above critical, the Re is held constant for thousands of endwall rotations. After observing the steady flow to ensure that no unsteady transitions are occurring, oscillations are induced by disturbing the flow with a relatively large perturbation in Re. At this point, the flow becomes unsteady. This unsteady flow is observed for thousands of endwall rotations to ensure that no transition to steady flow occurs. Each rotation lasts for approximately 0.7 sec. The Re is then reduced in steps until the critical Re is reached. At each step, the flow is observed for thousands of endwall rotations.

From the experiments and numerical simulations, it is apparent that two flow states exist beyond a critical Re number: a stable, steady and a stable, periodic state. In the experiments, steady flow is observed up to Re = 2715 and periodic flow is observed down to Re = 2705. The numerical results indicate a critical Re of approximately 2705 above which the two states exist. This falls within Re = 2705, where the periodic flow exists, and Re = 2702 where only a steady flow was found in the experimental investigation. Escudier[11] reports periodic flow for H/R = 2.5 only for Re > 2680, below which, according to his experiments, only steady flow exists.

1.5.2 Characteristics of Periodic Flow

The unsteady flow at H/R = 2.5 has been explored by us for 2705 < Re < 5000. There are no previous detailed experimental results reported for this range of Re. The motivation for this study is the finding of a second critical Re by Lopez[26] at approximately 3500 where the characteristic frequency of the oscillation changes. This change is reflected in Fig. 1-9 at Re ≈ 3500, where there is a discontinuity in the maximum azimuthal vorticity of the flow. In the experiment, the Re was increased and held fixed similar to the experiment described in § 1.5.1. At each of the holding intervals, the frequency of oscillation was measured. For Re between 2705 and 3400, the characteristic time of oscillation, $\tau = \Omega t$, is approximately 36. Above a Re of 3500, τ changes to approximately 28. These results are consistent with the findings of Lopez[26]. There is also evidence of a hysteresis loop involving the characteristic time of oscillation.

Chapter 2

Experimental Apparatus

In this chapter, the setup used to generate vortex breakdown is described. Details of the supporting equipment are provided along with relevant analysis. The sections are divided into flow support, measuring instruments, flow visualization and recording, experiment management, and ancillary equipment.

2.1 Flow Support

This section includes descriptions of the test fluid, test section, drive motor, and height adjustment mechanism. Figure 2-1 is a schematic of the flow apparatus and will be referred to throughout this chapter and others.

2.1.1 Test Fluid

The working fluid is a 3:1 mixture by volume of glycerin and water. Glycerin is a colorless, oily liquid that is completely miscible with water. This mixture provides a higher viscosity than water alone. With a higher viscosity, a more practical (higher) disk frequency can be used for the same Re allowing a faster evolution of the flow. The drawback of this fluid is the strong dependence of the viscosity upon the temperature (§ 2.2.3).

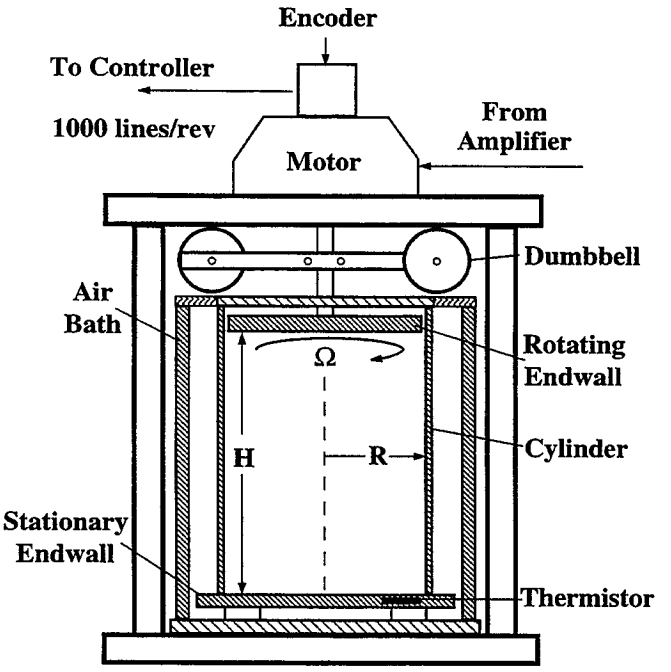

Figure 2-1 Schematic of apparatus

2.1.2 Test Section

Figure 2-2 depicts the test section with both endwalls. The vortex flow is formed within a circular cylinder with a diameter of 19.126 cm. The cylinder has one stationary endwall and one rotating endwall. The non-rotating endwall contains two ports for draining/filling and seven ports for dye injection. The drain/fill holes are located at the outer radius of the endwall. One dye port is positioned in the center of the wall with the other six spread out radially, three on a side. These ports have a diameter of 0.038 cm while the drain/fill holes are 0.318 cm in diameter.

The rotating endwall is a Plexiglas disk attached to a motor by a stainless steel shaft. The disk (as well as the bottom endwall) are made of Plexiglas since the test fluid (glycerin and water) corrodes aluminum. The cylinder has a lid (not shown) made of aluminum that keeps contaminants out of the test section.

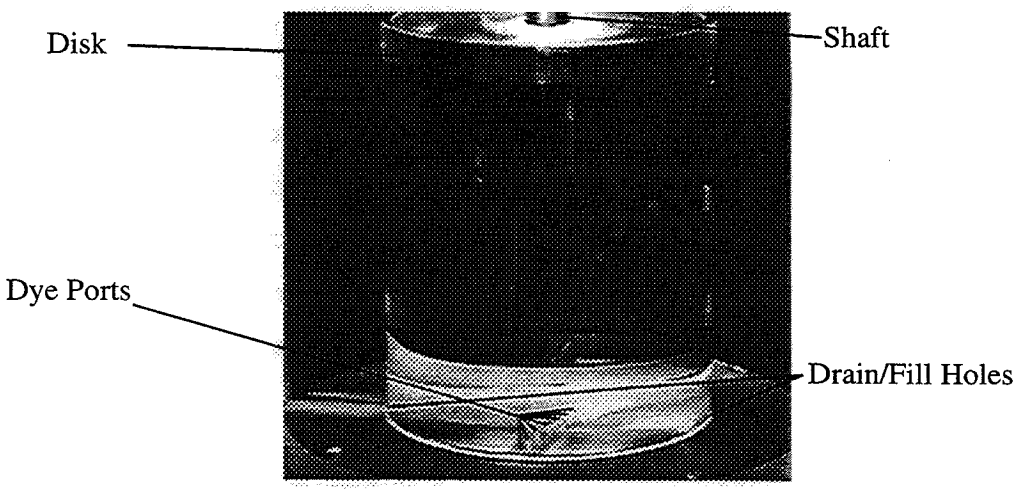

Figure 2-2 Test section

2.1.3 Drive Motor

The drive motor is a PMI Motion Technologies JR16M4CH-1/F9T/ENC servo-motor. This type of motor was considered ideal for this particular application because of the low friction inherent in its pancake design. Instead of having an iron core, the armature is made of several layers of copper conductors in a flat-disk configuration. Since there is no iron, the magnets in the motor do not force the armature into a desired position. Hence, there is no cogging. The motor is sized for experiments at high Reynolds number. Thus, the operating frequency for the present experiment is at the low end of the linear range of the motor and has presented some control challenges.

2.1.4 Height Adjustment Mechanism

The height of the cylinder is variable using linear bearings and brackets at the corners of the aluminum base plate (Fig. 2-3). A weight and pulley system has been incorporated to allow easy height adjustment. Two linear bearings are on each column of the aluminum motor support structure. The lower one is a linear ball bearing which had too much play for accurate height adjustment. A second bearing with a Teflon inner sleeve was manufactured to constrain the set of two bearings to run vertically with very little play. These bearings are attached to aluminum brackets which support the corners of the base plate. By using weights and pulleys with ropes attached to the support brackets, the effective height of the cylinder is continuously adjustable from 14.29 to 28.58 cm. This translates into a height-to-radius ratio (H/R) range of 1.5 to 3.0. On two diagonally opposing supports, between the two bearings, are clamps which secure the cylinder at the desired height.

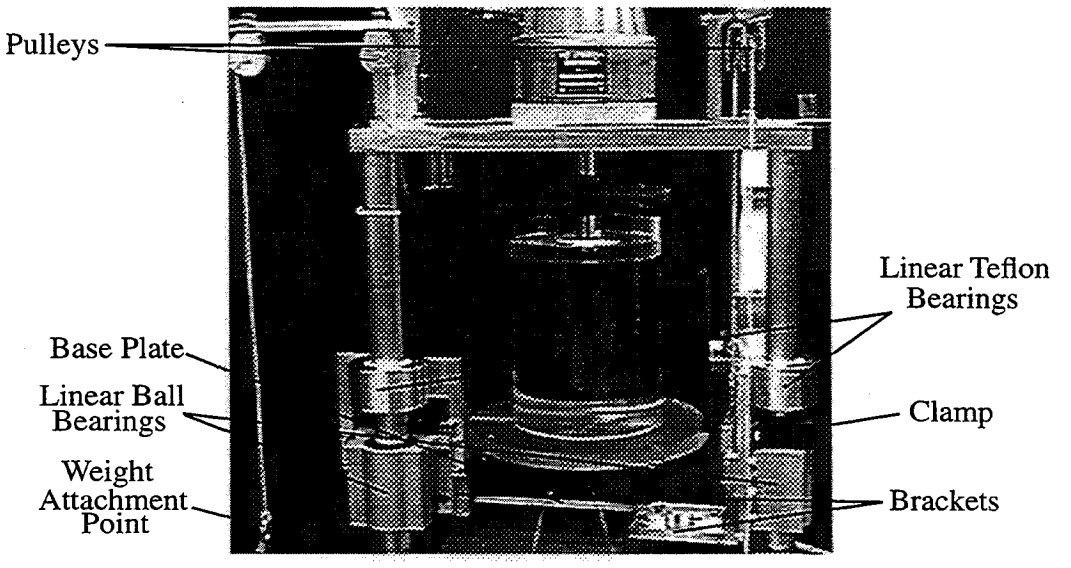

Figure 2-3 Height adjustment mechanism

2.2 Measuring Instruments

Several types of measurements are necessary to determine at which point in parameter space (Re, H/R) the experiment is operating. To determine the H/R ratio, the height of the disk and radius of the cylinder are accurately measured. The Re is a more difficult parameter to quantify because it requires accurate knowledge of the angular velocity of the disk, radius of the cylinder and viscosity of the test fluid. The latter requires accurate measurement of the temperature. The motor voltage and current are also monitored.

2.2.1 Height and Radius

The height of the cylinder is the distance between the lower endwall and the bottom of the rotating disk. By holding a scale parallel to the cylinder wall, the height is determined to within 0.04 cm.

The radius of the cylinder is measured with a vernier caliper precise to 0.003 cm (0.001 in). The thickness of the Plexiglas cylinder may vary up to 0.03 cm over its surface.

2.2.2 Disk Frequency

Attached to the motor shaft is an optical encoder with 1000 lines of resolution. On each rotation of the disk, the encoder outputs 1000 equally spaced pulses. The encoder signal is read by a Hewlett-Packard 34401A Digital Multimeter (DMM). On frequency mode, the DMM is capable of reading to a hundreth (0.010) of a Hertz (Hz). Although the disk runs a thousand times slower than the frequency produced by the function generator, the clock signal is not steady to less than a tenth of a Hz. Therefore, the disk speed is read to a ten-thousandth (0.0001) of a Hz, although the measurement is better by one order of magnitude.

2.2.3 Viscosity

As noted by Escudier[11], the viscosity of the test fluid is very sensitive to temperature which must be carefully monitored. The viscosity changes by approximately 5 % per degree Centigrade (°C). The test section was enclosed in a water bath in an endeavor to keep the operating temperature constant. This method did not work to satisfaction since the bath did not maintain a reasonably constant temperature. During the day, from about six a.m. to eleven p.m., air-conditioning keeps the room at a comfortable, but not very constant, temperature. Depending on how the air is circulated throughout the laboratory, changes in temperature up to 1 °C are experienced over a time scale of approximately fifteen minutes. Therefore, the water bath was abandoned in favor of a totally enclosed air bath. Since air has a low thermal conductivity, its insulation properties are good. Once the air-conditioning is turned off, it is no longer feasible to operate the experiment since no reasonable temperature can be maintained. Although the temperature fluctuations are small within the test cylinder, it is still necessary to know the viscosity over a range of temperatures since the operating temperature is not known before hand. A linear fit of viscosity vs. temperature is created for each experiment. In this fashion, the viscosity is determined simply by measuring the temperature in the test section.

A sample of the fluid in the test section is siphoned to the lower timing mark of a size 200 (for viscosities between 20 and 100 centi-Stokes (cS)) Cannon-Fenske Routine Viscometer. The viscometer is then suspended in a water bath with an insulating top. (The water bath is the original, aluminum-bottomed test section cylinder.) The two upper tubes must be within 1° of vertical. A level capable of measuring within this limit is used to insure the proper alignment of the instrument. The meniscus of the test fluid is then drawn past the first timing mark and allowed to fall. The viscosity of the fluid is determined in cS by multiplying the number of seconds the meniscus takes to fall from the upper to the lower timing marks by the viscometer constant (0.1014 cS per second for experiment

operating temperatures). During the whole procedure the temperature must be prevented from varying by more than 0.01 °C. This measurement procedure conforms to ASTM Standards D 445 and D 446.

2.2.4 Temperature

Several methods for measuring temperature were tried. The first attempt was made using E type thermocouples. The sensor is a junction of nickel-chromium and copper-nickel metals. When heated to a certain temperature, these two metals create a known potential. The voltage output of this sensor is approximately 0.06 mV per °C[31]. The resolution of the voltage measurement device is 0.04 mV. Therefore, using this thermocouple, the temperature can be measured in increments of ~ 0.7 °C. Since the viscosity of the fluid changes ~ 5 % per °C, this reflects a 3.5 % uncertainty in viscosity alone.

A more precise instrument for measuring temperature is the thermistor. The resistance of this device depends on the temperature. Table 2-1[31] shows the temperature dependence of the Omega Engineering part number 44004 thermistor. The recommended curve fit is given as:

$$\frac{1}{T} = A + B \cdot \ln R_T + C \cdot (\ln R_T)^3 \qquad (2\text{-}1)$$

Table 2-1 Thermistor resistance vs. temperature

T (°C)	R_T (ohms)
15	3539
16	3378
17	3226
18	3081
19	2944
20	2814

Table 2-1 Thermistor resistance vs. temperature

T (°C)	R_T (ohms)
21	2690
22	2572
23	2460
24	2354
25	2252

Using Equ. (2-1), the values can be fitted such that the resolution for temperature is ± 0.01 °C[31] or better. Figure 2-4 displays the curve fit with the following values for A, B, and C:

$$A = 1.474e-03$$
$$B = 2.370e-04$$
$$C = 1.091e-07$$

A Wheatstone bridge circuit (Fig. 2-5) enables the accurate determination of the thermistor resistance. R_1, R_2, and R_3 can be calculated such that the resolution in temperature is adequate. V_{out} is given by:

$$V_{out} = V_{in} \cdot \frac{R_2 \cdot R_T - R_1 \cdot R_3}{(R_1 + R_2) \cdot (R_3 + R_T)} \tag{2-2}$$

Since the thermistors are self-heating, it's important to limit the power through the device. By limiting the current to 0.5 mA at 25 °C, there should be negligible self-heating. From Figure 2-5, i_2 is given by:

$$i_2 = \frac{V_{in}}{R_3 + R_T} \tag{2-3}$$

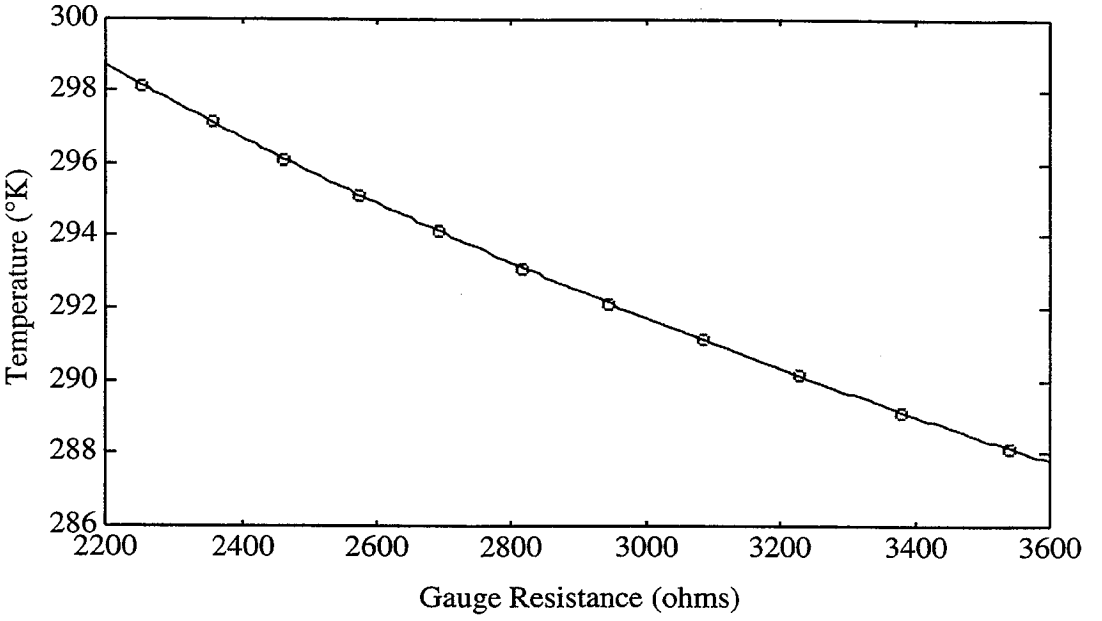

Figure 2-4 Curve fit for thermistor resistance values

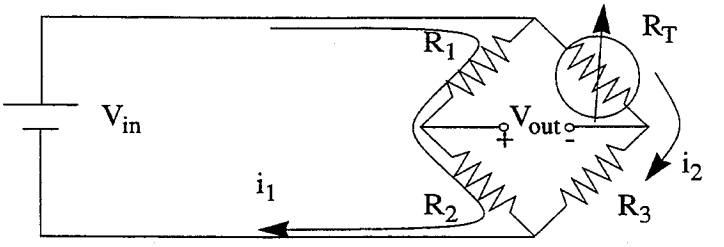

Figure 2-5 Wheatstone bridge circuit for thermistor

By setting Equ. (2-3) equal to 0.5 mA, using the value for R_T at 25 °C, and assuming an input voltage of 2 V, R_3 is found to be 1748 ohms. Another assumption is to set V_{out} equal to zero when the temperature is 20 °C. From Equ. (2-2), the following relation is found:

$$R_1 \cdot R_3 = R_2 \cdot R_{T20} \tag{2-4}$$

where R_{T20} is the value of R_T at 20 °C. From Equ. (2-4), the ratio of R_1 to R_2 is found to be 1.61. Therefore, R_1 was chosen to be 16100 ohms and R_2 was chosen to be 10000 ohms. Using these values in Equ. (2-2), V_{out} equals -108 mV at 25 °C and 105 mV at 15 °C. With this 213 mV range over a 10 °C temperature difference and data acquisition set for a full scale of 2.5 V with 16-bit resolution (discussed in § 2.2.5), a resolution of $\frac{2.5V}{2^{16}} \cdot \frac{10°C}{213mV} \cong 0.002°C$ is achievable. This is more than satisfactory since the 44004 thermistor is known to be precise to ± 0.004 °C.

The power the thermistor experiences is given by $i_2^2 R_T$. At 25 °C i_2 is 0.5 mA and R_T is 2252 ohms giving a power of 0.56 milliWatts (mW). The power required to raise a thermistor 1 °C above the surrounding temperature is 8 mW/°C in a well stirred oil bath or 1 mW/°C in still air.[31] Since the thermistor is immersed in glycerin/water, the dissipation value should be between 1 and 8 mW/°C. Assuming a value of 4 mW/°C, the thermistor will measure a temperature 0.14 °C above ambient. But as long as both thermistors agree well with one another, an accurate reading of viscosity is obtainable by measuring the temperature in the test section and calculating the viscosity from the viscosity vs. temperature calibration curve created for each experiment.

2.2.5 Voltage and Current

Both voltage and current are read by the on-board computer data acquisition card. Manufactured by National Instruments, the NB-MIO-16XH is capable of reading analog voltages with a resolution of 16 bits over a range of 20 V. The board also has amplifiers which can achieve gains of 1, 2, 4, and 8. At a gain of 8, the effective full scale reading is reduced to 2.5 V. With the 16 bit resolution, this translates into a maximum voltage resolution of 38 μV.

The voltage between the motor terminals is read directly by the board. Since this voltage is usually greater than 4, but no more than 10 volts, a gain of 1 is used. This gives a precision of 305 μV.

Reading the current is a more difficult task since the board cannot take a current input. Therefore a current shunt manufactured by Hewlett-Packard (model 34330A) with an output of 1 mV/A is utilized. The current never exceeds 0.5 A which produces a voltage of 0.5 mV from the shunt allowing a gain of 8 on the data acquisition board to be used. This leads to a precision of 38 mA in current.

2.3 Flow Visualization and Recording

Several items are necessary to view the flow. Since the fluid is clear, a dye is used to make the flow structure visible. The dye is fluorescent and can be illuminated with a laser. To make a record of the qualitative (and some quantitative) aspects of the flow, a camcorder documents the experiments. Video frames are captured for analysis by a frame grabber video board installed on the computer (MacIntosh IIci).

2.3.1 Fluorescein Dye

Fluorescein is a water soluble powder that has a deep yellow color. However, when light with a wavelength between 400 and 500 nm illuminates the dye, the substance radiates in the green spectrum. The injected dye is made using 200 mg of Fluorescein powder

dissolved in 100 ml of the glycerin/water solution. Twenty-five drops of this concentrated dye are mixed with 300 ml of glycerin/water solution to create the dye solution. The final concentration is 5.4 ppm by weight of Fluorescein powder in the solution that is injected into the vortex column.

2.3.2 Dye Injection

A Harvard Apparatus infusion pump (model 975) can drive one or two syringes at 30 different speeds, 1 being the fastest and 30 the slowest. The volume flow rate depends on the diameter of the syringe. Since the dye is injected directly into the vortex column, it is important to keep the pump rate slow enough as not to disturb the flow. But it is also important to keep it high enough so that there is enough dye to be sufficiently illuminated by the laser. Through trial and error, with the given dye concentration and laser power, the range of pump rates between 19 and 24 (0.11 and 0.02 cm^3/minute) was found to be adequate for a 50 ml syringe. Nineteen gives the best fluorescence, but twenty-four allows longer experiment runs since the dye is introduced more slowly and contamination of the cylinder fluid occurs more slowly. These volume flow rates translate into exit velocities from 0.3 to 1.6 cm/sec through a 0.038 cm hole.

2.3.3 Dye Illumination

A thin sheet of light is needed to fluoresce a cross-section of the flow. This sheet is produced using a Helium-Cadmium (He-Cd) laser (wavelength = 442 nm) and several optical lenses and mirrors. Figure 2-6 shows the optical arrangement. The beam is first directed through a steering mirror (two mirrors set 90° apart on a vertical shaft) to change the height and direction of the laser light. The plano-convex lens (focal length of 622 mm) focuses the beam so that it will be narrowest in the middle of the test section. By passing the beam through a cylindrical lens, the light is spread into a sheet which is directed

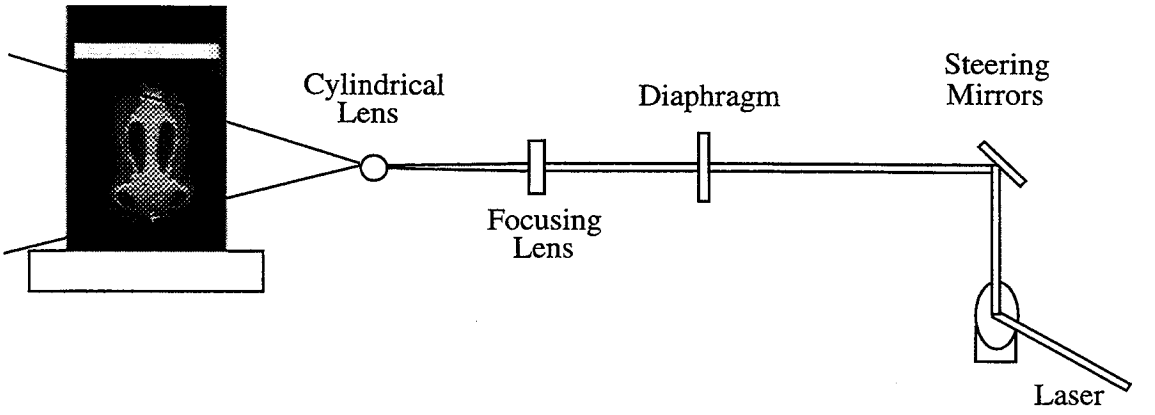

Figure 2-6 Optical arrangement

through the center of the cylinder. The cross-section of the flow is made visible when the dye fluoresces. The diaphragm cuts back on the reflections from the lenses and cylinder sides.

2.3.4 Recording an Experiment

A Canon L2 Hi8 video camcorder is used to record the experiments. The high recording quality of the Hi8 system allows detailed visuals of the flow in action. Also the low light capabilities of the camera are indispensable for this experiment. Since the dye must flow continuously for hours on end, it's necessary to keep the concentration of the dye as low as possible. The fluorescence is strong enough to see by eye, but an ordinary video camera would not be sensitive enough to pick up the fluorescent light. Initially the camcorder is electronically shuttered to an eighth (1/8) of a second. (Electronic shuttering is a built-in function of the camera.) After the experiment has run for a while, more of the flow fluoresces making it necessary to change the shutter's open period to a shorter time. The reflections of the laser light from the cylinder walls and small particles in the flow are filtered out by a yellow filter (Y 52) placed in front of the camera lens.

Besides having the camera record the session, some live images are captured directly to computer memory. The frame grabber board is black & white and captures one frame at a time. By digitizing the picture live, the image quality is enhanced.

2.4 Experiment Management

There are several aspects of controlling and monitoring an experiment. For a precise disk rotation rate, a phase-locked loop (PLL) controls the frequency of the motor. This frequency is updated using a slow modulation signal generated through LabVIEW2™. LabVIEW is a graphical programming language that interfaces with the data acquisition board allowing voltages to be inputted and outputted in a number of ways. The program also interfaces through GPIB and serial ports on the computer. Using LabVIEW, all of the measured quantities are digitized and stored.

2.4.1 Phase-Locked Loop Motor Controller

In a PLL circuit, the elements are a phase detector, loop filter, and voltage controlled oscillator (VCO)[32,33]. In the current set up, the phase detector is the Motorola MC4044 Phase-Frequency Detector chip; the loop filter is constructed from common resistor-capacitor (RC) networks; and the VCO consists of a linear power amplifier, servo motor, and optical encoder. Appendix A describes the circuit in detail.

The optical encoder produces one-thousand pulses per revolution of the motor. The PLL actually controls the instantaneous position of the motor by having the phase detector compare the encoder signal with a clock signal set at one-thousand times the desired motor frequency. The detector outputs two error signals that are proportional to the phase difference between the encoder and clock signals. These error signals are then directed through the RC network with operational amplifiers which transform the signals into DC voltages that are applied to the power amplifier. The power amplifier supplies the appropriate voltage and current to run the motor at a very constant angular velocity.

The clock signal is produced using a function generator (HP model 3312A) set to square wave output. This signal is modulated to produce frequency ramps that can increase or decrease the Re of the experiment. The modulation signal is created through LabVIEW2 giving excellent control over the shape, speed, and coarseness of the ramp. A subprogram, or sub vi (virtual instrument), loads a digital array into a buffer. The buffer is accessed by the D/A converter and puts out a voltage depending on the value of the current element in the array. The 12-bit D/A can output between -10 and 10 volts. Therefore, the smallest voltage step possible is 4.9 mV. The step and range in frequency is controlled by the position of the ΔF (change in frequency) knob on the function generator.

2.4.2 LabVIEW Control Program

LabVIEW allows easy control and reading of experiment parameters using a graphical user interface (GUI) that simplifies communications between the computer and the experimental control and measurement devices. The flow chart in Figure 2-7 shows how the Experiment Manager program works. First, one of the analog output channels is set to two volts to supply the thermistor Wheatstone bridge network. Then the program sets up the duration of the frequency sweep and the time between updates in the frequency. This also allows indirect control of the step in Re per unit time. Next, both the frame grabber board and the DMM are set up to acquire images and frequency respectively.

At this point, if the 'Save Run?' option is chosen, a file is created and the user is prompted for the file name. If saving is not wanted, the program continues without creating a data file. The point 'A' in the flow chart marks a return point. If the frequency is to be held, then the program halts the modulation voltage sweep. 'Resume' will start the sweep after a hold has been executed. The next section of the program is the actual data acquisition.

The 'DATA GRAB' sub vi reads the following quantities continuously until the sample period is over: frequency modulation voltage, thermistor supply voltage, fluid thermistor voltage, room thermistor voltage, motor current as measured by the current shunt, motor terminal voltage, and the disk frequency as read by the DMM.

After the sample period is over, the measured quantities are averaged. Using these values, both the viscosity and Reynolds number are calculated. If the 'Grab Image and Save' option is chosen, the frame grabber is instructed to take a snapshot of the flow and the program saves it with the current Re as the file name. If 'Display Image' is chosen, the frame grabber takes a snapshot and the program displays the image in its own window.

If one-hundred sample periods have been completed and the 'Save Run?' option was chosen at the beginning, the data is saved and the data array in the computer memory is cleared for new values. If the 'Stop' option is not selected, the program returns to point 'A' where the frequency modulation sweep options are monitored and the data queries are executed again. If 'Stop' is selected, the program checks to see if the 'Save Run?' option was selected at the beginning of the experiment. If 'Save Run?' was chosen, the data is saved and the data array is cleared. If the data is not to be saved, the program simply resets the DMM and sets the thermistor supply voltage back to zero. Note that the modulation voltage is not set to zero. Therefore, if the program accidentally quits, the flow state is preserved.

2.5 Ancillary Equipment

A few more pieces of equipment are necessary to ensure that the experiment is carried out properly. These include filters for the fluid, an oscilloscope, a flywheel, and a counter. An ordinary fish tank filter with activated charcoal removes the Fluorescein dye from the glycerin/water solution. After approximately two weeks of constant filtering, the fluid can be used in two or three experiments before filtering becomes necessary again. Another filter is used to catch small particles in the fluid so that laser scatter is reduced. The filtering

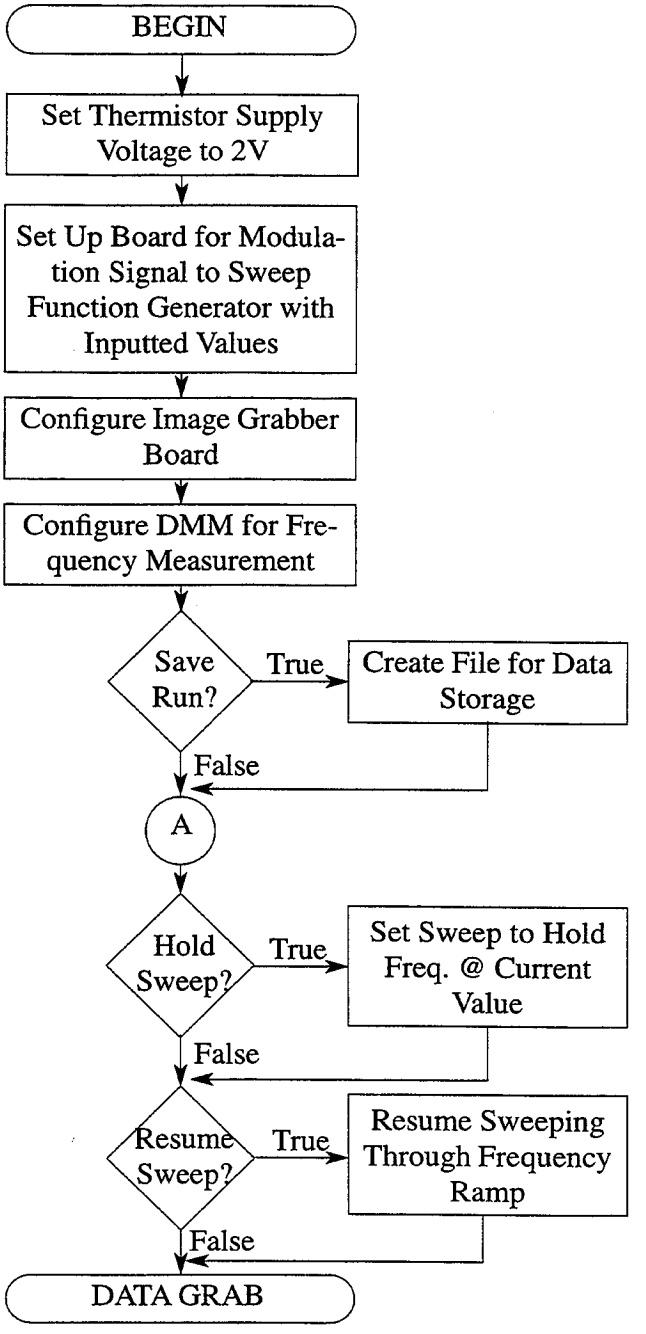

Figure 2-7 Experiment Manager flow chart

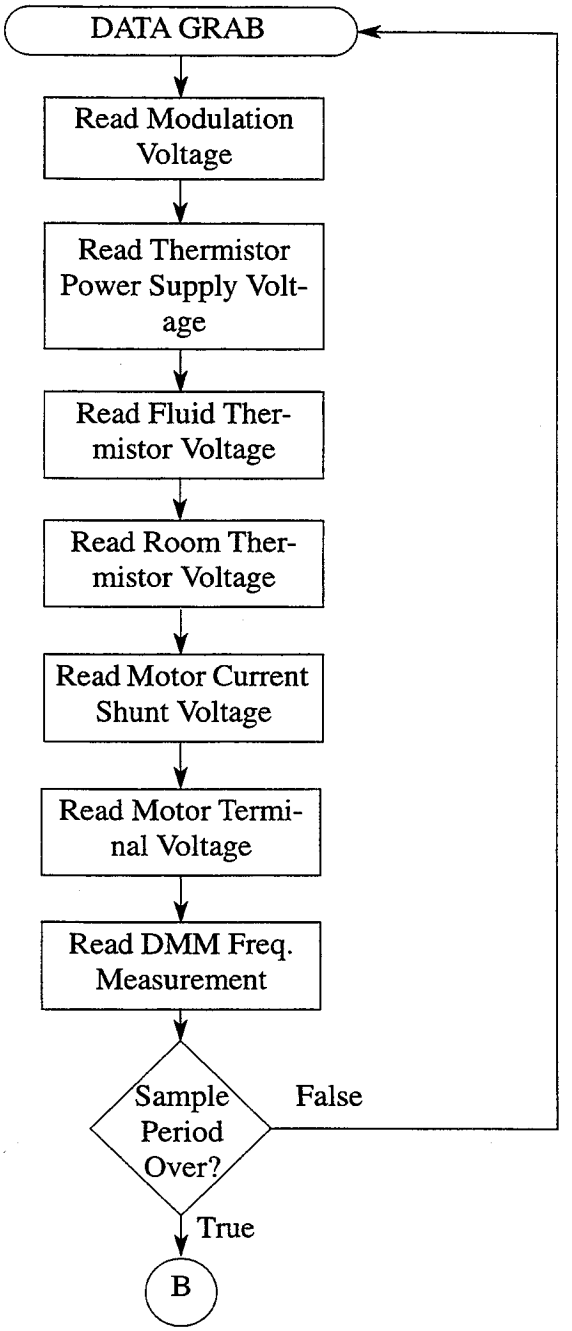

Figure 2-6 (Continued) Experiment Manager flow chart

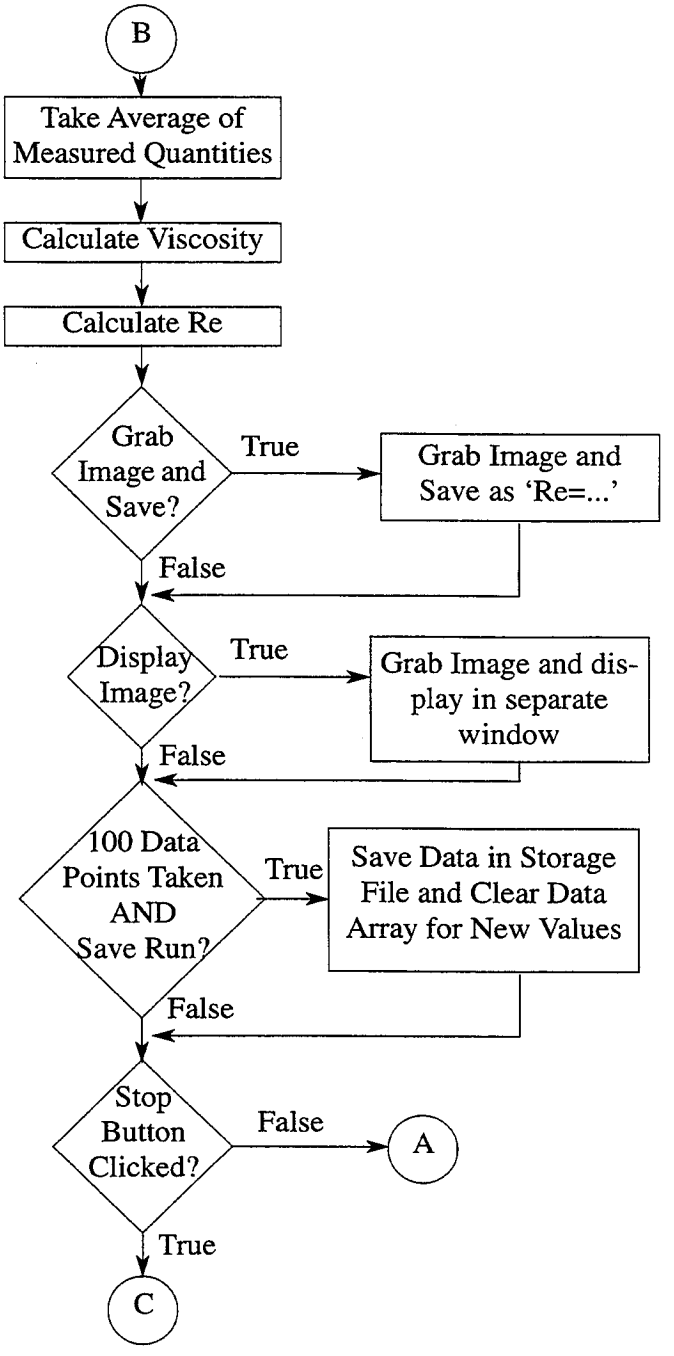

Figure 2-6 (Continued) Experiment Manager flow chart

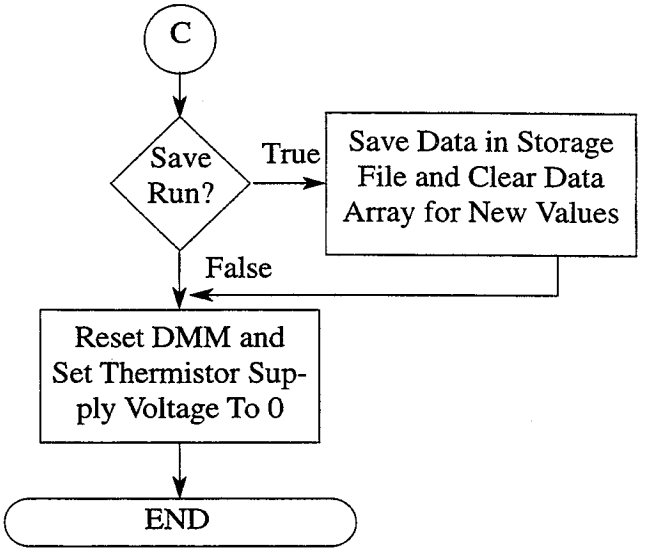

Figure 2-6 (Continued) Experiment Manager flow chart

is done prior to filling the test cylinder. This crucial filter procedure was found necessary for preventing particles in the flow from clogging the capillary tube of the viscometer. If the fluid from the test section is filtered again, prior to filling the viscometer, the fluid will have different properties since the filter paper has a tendency to leech water from the solution.

The oscilloscope monitors the motor shaft encoder and clock signals to ensure that the motor speed is locked as well as possible. By triggering on the clock signal, the encoder signal can be studied for variations from the desired signal. A flywheel (a.k.a. dumbbell) is attached to the motor shaft to damp out high frequency jitter in the motor speed. An HP model 5315B universal counter measures the reference clock output frequency and allows precise tuning of the function generator.

Chapter 3

Experimental Considerations

This chapter explores the techniques used to set up the equipment and examines the accuracies of measurements. It is important to minimize the disturbances and deviations from axisymmetry inherent in the flow since comparisons are made to numerical simulations which do not have these imperfections. The uncertainties in parameter measurements determine how closely the Re and aspect ratio (H/R) of the experiment are estimated.

3.1 Minimization of Perturbations

Although the overall experiment is a complex integration of equipment and measuring instruments, the actual creation of the recirculation bubbles is done with only one moving part: the rotating endwall. The rotating endwall drives the flow and also contributes extraneous disturbances. There are a number of ways these perturbations can be created. The angular velocity of the disk has some jitter about the desired rotation rate. Also, the disk may not be perfectly aligned and may exhibit a slight wobble. The dye injection system also disturbs the flow to a certain extent depending on the smoothness and velocity of the dye injection process.

3.1.1 Disk Jitter

The phase-locked loop (PLL) motor controller (Appendix A) does a good job of controlling the disk rotation, but is not perfect. The motor controller is the most complex system in the experiment and is susceptible to the most problems. In theory, a PLL will control an oscillator with zero error and no deviation from the mean velocity. However in this experiment, the oscillator is in fact a DC motor which is subject to frictional torques, particularly when operated at low speed. Normally, friction can be overcome if it is predictable and smooth. However, at low rotation speeds the friction in the motor is highly non-linear. At a few points in the rotation position, large friction areas are present, whereas most of the rotation is dominated by very low friction. These large friction areas are abrupt and cause the motor to brake. Upon entering a friction region, the controller reacts quickly and corrects the error by applying more voltage. As the friction region passes, the controller senses this and reduces the voltage swiftly. Although the circuit is fast, it is not fast enough to zero out the jitter caused by the abrupt voltage swings necessary to keep the motor speed locked onto the reference signal. In theory, the circuit can be fine tuned to damp out this jitter. But due to the physical limitations, the PLL cannot be designed for this speed since this frequency coincides with the reference frequency. If the PLL were allowed to operate at the reference frequency, the signal would feed through the control loop and destroy any attempt at controlling the motor.

The jitter was unacceptable without some modifications to the system. The friction forces were too strong and affected the motor too quickly. Therefore, the influence of these non-linear forces had to be greatly reduced. Since the angular acceleration (change in angular velocity) of the disk is proportional to the applied torque divided by the inertia of the disk, increasing the inertia and/or decreasing the friction torque will decrease the angular acceleration. This is analogous to a light car and a heavy car crossing a bump in the road. The heavier car will roll over the bump with a smaller decrease in velocity than the lighter car would in the same situation. Increasing the inertia is easier to implement than

decreasing the friction. In this case, a fly 'dumbbell' has been added to the disk shaft (see Fig. 2-1). Addition of a flywheel to the motor shaft has a destabilizing effect on the PLL system since the added inertia changes the dynamic characteristics of the loop. After tweaking the PLL circuitry, the motor jitter was reduced to acceptable, although non-zero, levels.

3.1.2 Disk Wobble

The disk was machined after attachment to its own shaft and has very little inherent wobble. Some wobble is introduced when the disk shaft is attached to the motor shaft. There are four set screws that protrude through the disk shaft to squeeze the motor shaft. Care must be taken to tighten the screws properly to ensure that the disk stays on with very little wobble, especially since there is a heavy dumbbell attached to the shaft.

By measuring the runout at the edge of the disk with a dial gauge precise to 0.0003 cm (0.0001 in), most of the wobble can be removed by slowly turning the disk and tightening the correct set screw in the correct order. After careful alignment, the disk has 0.0013 cm of wobble at the edge. This corresponds to less than 0.01° of tilt (Fig. 3-1).

3.1.3 Dye Injection System

Early experiments showed that the flow was extremely sensitive to the dye injection rate. Using a medium setting on the infusion pump, the Re was set to ramp slowly. Knowing that the first recirculation bubble occurs relatively close to the stationary endwall, it was uncharacteristic to see the bubble appear closer to the rotating endwall. After this observation, the dye injection rate was lowered. Accordingly, the bubble appeared to move away from the rotating endwall. The injection rate was lowered until no further movement of the bubble was apparent. Adequate dye injection rates vary from 0.02 to 0.11 cm^3/min corresponding to flow velocities from 0.3 to 1.6 cm/sec.

By injecting the dye at a high rate, momentum is added to the core. This extra momentum overcomes the retarding effects of the azimuthal vorticity for a longer distance along the core, delaying the formation of the bubble to a point closer to the rotating disk.

The infusion pump that injects the dye is a hospital grade system. Since it is used in critical situations, the pump has a very precise rate of injection. The only time any amount of unsteadiness appears while the pump is depressing the syringe is when the resistance is large. The resistance can become large if the fluid is very viscous, the pump rate is too high, or the line is crimped. When any of these situations occur, the gears in the pump backlash on every revolution causing a pulse to be sent through the injection port. Since the fluid is not too viscous and the pump rates must be kept low so as not to affect the flow, backlash can be eliminated with careful arrangement of the injection tube.

3.2 Minimization of Non-Axisymmetries

Asymmetries can appear in the flow due to poor alignment of the disk with the center of the cylinder, or if the non-rotating endwall is not leveled with the rotating endwall. In the first case, one side of the recirculation bubble will be stretched radially more than the other side destroying the axisymmetry. The latter case causes azimuthal waves to appear. (These imperfections are examined more fully in Chapter 5: Discussion.) Figure 3-1 shows the alignment parameters, but not to scale.

3.2.1 Disk Centering

The cylinder has a nominal diameter of 19.126 cm and varies as much as ±0.005 cm. The disk has a diameter of 18.791 cm. Therefore, the gap between the cylinder wall and the edge of the disk is nominally 0.168±0.003 cm due to the imperfections in the cylinder. Since the gap can be as small as 0.165 cm, a 0.160 cm diameter pin gauge is used to center the disk in the cylinder. By tapping the Plexiglas endwall that the cylinder rests on with a rubber mallet, the disk and cylinder can be centered to ±0.008 cm.

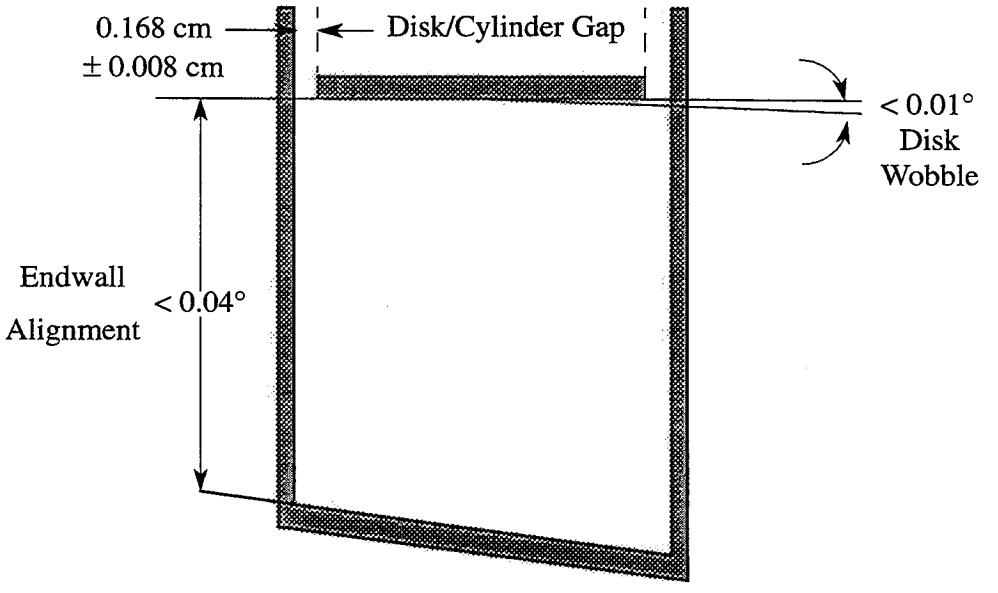

Figure 3-1 Disk alignment parameters

The limits on the cylinder diameter brings up another problem: How smooth and circular is the cylinder throughout its height? The cylinder has been measured at some points and is found to have variations in the diameter of up to 0.08%. A complete topology of the interior of the cylinder is not known due to the cost in determining the contours. Conceivably, this will affect the form of the flow, but to what degree is unknown.

3.2.2 Endwall Alignment

The rotating endwall is aligned with the non-rotating endwall using an electronic level accurate to ±0.01°. The cylinder is secured to the aluminum bottom plate with four bolts around the perimeter of the stationary endwall (outside of the cylinder). By carefully raising the bottom plate via the brackets attached to the linear bearings, the two endwalls are aligned to within 0.03° of each other.

3.3 Measurement Accuracies

Measuring the experiment parameters accurately is important in determining where the flow is located in terms of (Re, H/R) space. By knowing the parameters, accurate comparisons can be made with other experiments and numerical simulations.

3.3.1 Length Measurements

The height and radius of the disk are the only two length measurements. The accuracy of the height measurement is 0.04 cm. During these experiments H/R is kept constant at 2.5. The nominal radius of the cylinder is 9.563 cm. Therefore, the height is required to be 23.91 cm. Since the resolution is only 0.04 cm, the uncertainty in the measurement is 0.17 %. The accuracy of the radius measurement is better at 0.003 cm (0.001 in). Therefore, the uncertainty in this measurement is 0.03%.

3.3.2 Disk Frequency

Due to angle dependent frictional torques which arise at low Ω, the motor exhibited small residual phase variations leading to speed variations on the order of 0.003 Hz (0.18 rpm). These are greatly reduced by a dumbbell-shaped flywheel attached to the motor shaft (§ 3.1.1). When compared with an HP model 5315B universal counter and an HP model 34401A multi-meter, the two signals were found not to vary by more than 2×10^{-7} Hz. Hence, the motor frequency remains within 0.0002 Hz of the desired frequency (reference frequency divided by 1000). The nominal operating disk frequency for the experiments is between 1.3 and 1.4 Hz. The frequency variations are approximately 0.02%, but the error in reading the speed is small at ~ 0.008% due to a combination of factors: the precision of the frequency measurement devices (§ 2.2.2) and the large number of lines per revolution output by the encoder. Therefore, the error in disk frequency is represented by the variations in control of the disk.

3.3.3 Viscosity Measurement

The viscosity accuracy depends on two measurements: viscosity and temperature. Temperature accuracy is important since the viscosity of the test fluid is inferred from the temperature reading in the cylinder.

In the ASTM Standard D 445, the viscometer uncertainty is given as ~ 0.35%. The error due to temperature accuracy is not so important as the error due to temperature repeatability. The accuracy is not important because the thermistors used to measure the temperature are calibrated against each other. Therefore, knowing how the two thermistors compare with one another will give the uncertainty in viscosity due to temperature measurement accuracy. Using the uncertainty method given by Holman[34], we can write viscosity, ν, as a function of some nominal viscosity, ν_o, and the actual temperature minus the nominal temperature, T_u:

$$\nu = \nu_o + B \cdot T_u \tag{3-1}$$

where B is the slope of the ν vs. T plot with a value of ~ -0.016 $cm^2/sec/°C$. The quantity ν_o has a nominal value of 0.285 cm^2/sec with an uncertainty of 0.35%. T_u is nominally zero (0) with an uncertainty of 0.004 °C. (The thermistors compare to ±0.004 °C.) The partial derivatives of Equ. (3-1) with respect to ν_o and T_u are needed to compute total uncertainty in ν. $\frac{\partial \nu}{\partial \nu_o} = 1$ and $\frac{\partial \nu}{\partial T_u} = B = -0.016 \frac{cm^2}{sec\,°C}$. The uncertainty in ν follows:

$$w_\nu = \left[\left(\frac{\partial \nu}{\partial \nu_o} \cdot w_{\nu_o} \right)^2 + \left(\frac{\partial \nu}{\partial T_u} \cdot w_{T_u} \right)^2 \right]^{1/2} \tag{3-2}$$

$$= \left[(1)^2 (0.0035 \cdot 0.285)^2 + (-0.016)^2 (0.004)^2 \right]^{1/2}$$

$$= 1.00 \times 10^{-3} \frac{cm^2}{sec}$$

The absolute uncertainty in viscosity is 0.35% which includes temperature effects.

3.4 Parameter Uncertainties

There are two types of uncertainties: absolute and relative. Absolute uncertainties give an estimate of how well the calculations of the parameters match the true values. Comparisons with other studies are made by taking into account how well the measurements predict the absolute parameters. Relative uncertainties, however, give a measure of the precision of the calculated parameters. Control of the experiment can be inferred from the values of these relative calculation errors.

3.4.1 Absolute Uncertainty

All of the measurement errors are taken into account to calculate the absolute uncertainty in Re and H/R. In summary, these accuracies are given in Table 3-1.

Table 3-1 Parameter uncertainties

Measurement	Accuracy (w)	Nominal value
R	0.003 cm	9.563 cm
H	0.04 cm	23.91 cm
Ω	0.0013 rad/s	8.304 rad/s
ν	0.0010 cm^2/s	0.285 cm^2/s
T	0.004 °C	23.0 °C

The partial derivatives of $Re = \Omega R^2/\nu$ are as follow:

$$\frac{\partial Re}{\partial R} = \frac{2\Omega R}{\nu} \tag{3-3}$$

$$\frac{\partial Re}{\partial \Omega} = \frac{R^2}{\nu} \tag{3-4}$$

$$\frac{\partial Re}{\partial \nu} = -\frac{\Omega R^2}{\nu^2} \tag{3-5}$$

Using Equs. (3-3), (3-4), and (3-5) to calculate the absolute uncertainty in Re, the following equation is obtained:

$$w_{Re} = \left[\left(\frac{2\Omega R}{\nu}\right)^2 (w_R)^2 + \left(\frac{R^2}{\nu}\right)^2 (w_\Omega)^2 + \left(-\frac{\Omega R^2}{\nu^2}\right)^2 (w_\nu)^2\right]^{1/2} \tag{3-6}$$

Inserting the values from Table 3-1 into Equ. (3-6), the uncertainty in Re is found to be 9.5 or approximately 0.36%. As can be seen, the majority of the doubt comes from the viscosity measurement.

The absolute uncertainty in H/R is calculated in a similar manner:

$$w_{H/R} = \left[\left(\frac{1}{R}\right)^2 (w_H)^2 + \left(-\frac{H}{R^2}\right)^2 (w_R)^2\right]^{1/2} \tag{3-7}$$

Substituting the values from Table 3-1 into Equ. (3-7), the uncertainty in H/R is calculated to be 0.004 or close to 0.17%, mostly due to the coarse measurement of H.

3.4.2 Relative Uncertainty

In the calculation of the quality of relative estimates, the uncertainty in parameters whose value do not change during a particular experiment is excluded in the analysis. The measurements that affect the relative uncertainty in Re are endwall speed and fluid temperature. Effects of fluid temperature measurement error are reflected in the viscosity estimate. The uncertainty in viscosity due to error in the viscometer is ignored for this analysis since the same instrument bias applies for all of the experiments and does not change for the duration of an experiment. H and R are held constant for the experiments, hence, they are excluded from the computation of relative uncertainty.

First, the effect of temperature measurement precision on the uncertainty of viscosity must be investigated. From Equ. (3-2), w_ν is calculated by assuming that $w\nu_o = 0$ and by substituting the appropriate values from Table 3-1. Therefore, solely due to temperature effects, the uncertainty in viscosity is 64×10^{-6} cm^2/sec or close to 0.002%.

Thus, using $w_R = 0$ cm and $w_\nu = 64 \times 10^{-6}$ cm^2/sec in Equ. (3-6), the relative uncertainty in Re is found to be 0.7 (0.03%). There is no relative uncertainty for H/R since H and R remain constant for the duration of the experiment.

Chapter 4

Experimental Results

4.1 Comparison of Initial Flow Structures

Some confidence is gained in the estimate of Re by comparing the values of Re at which certain flow structures appear with those of Escudier[11]. Since most numerical simulations have concurred with this sequence of events, this is deemed a good reliability test for the moment. Later on this assumption will be re-examined. Figure 4-1 shows the same sequence Escudier produced in his Fig. 4. Recall that the current flow is upside down relative to Escudier's flow, and beware that, in subsequent figures, the inverse of the captured images is shown so as to reduce the amount of black. Image processing techniques are discussed in Appendix C.

At a Re of 1918, there is clearly one bubble formed with a hint of a second one. As the Re increases, the second bubble takes shape and grows rapidly as evidenced by the flow at Re's of 1942, 1994, and 2126. As the bubble grows it moves downward towards the first bubble. Eventually, the upper bubble merges with the lower one at a Re slightly less than 2494. This sequence of events is identical to previous numerical and experimental results.

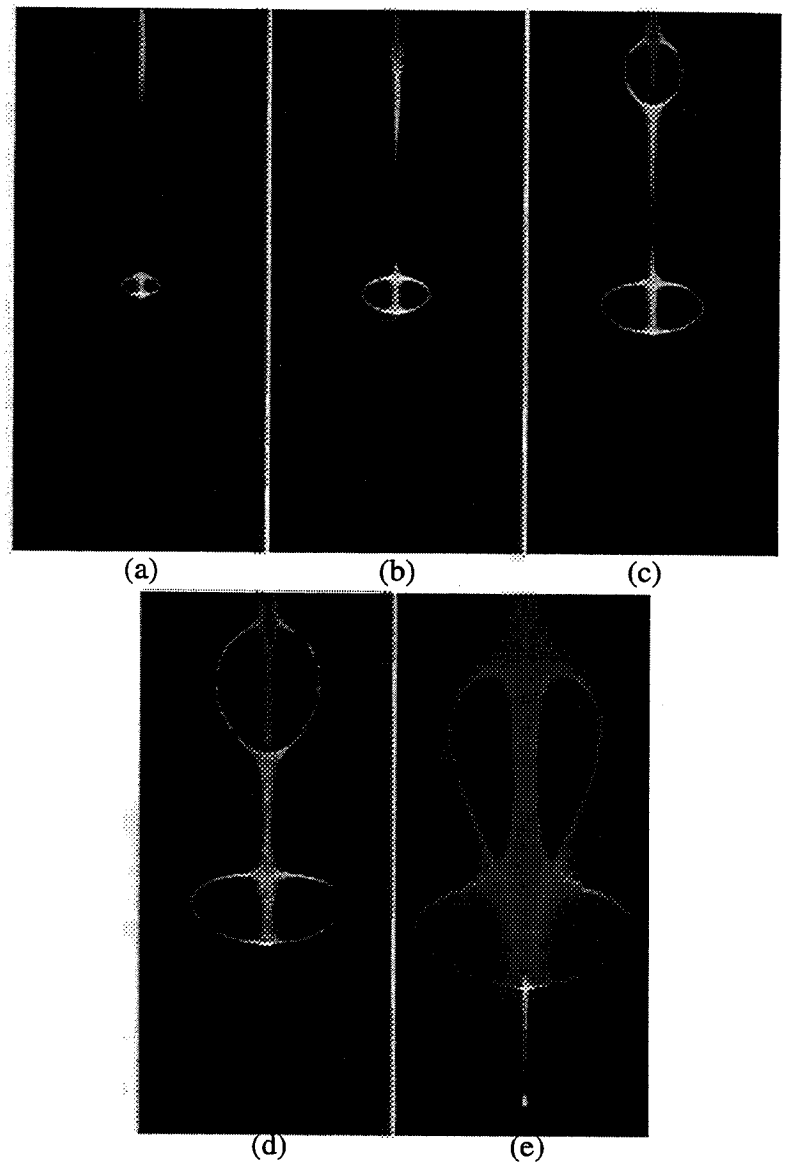

Figure 4-1 Structures for flows at a Re of (a) 1918, (b) 1942, (c) 1994, (d) 2126, and (e) 2494

4.2 Continuation of the Steady Flow

The usual view[23,25,27,28] has been that the onset of time-dependence occurs via a supercritical Hopf bifurcation where, at a critical value of the Re, dependent upon the aspect ratio, the steady solution branch loses stability to a time-periodic solution branch. Numerical evidence to the contrary was recently presented by Lopez and Perry[24] and Lopez.[26] In this work the steady solution branch from a second-order-accurate time integration of the axisymmetric Navier-Stokes equations was continued in Re beyond the Re where time-periodic solutions – following an impulsive start from rest – were previously found to be unique.

Here, results from an experimental investigation are reported where both steady and time-periodic flows were observed for several thousand endwall rotations at the same Re and H/R values. Our study supports the numerical findings[26] that the steady branch is stable beyond the Re where the time-periodic branch exists, and hence, the conclusion that the onset of time-dependence is not via a supercritical Hopf bifurcation.

Although results from one experiment are presented, the following described behavior was found to be robust after repeating the experiment several times. Appendix B describes three similar experiments.

Figure 4-2(a) shows the Re history of one experimental run. Figure 4-2(b) will be discussed after the periodic nature of the flow is described. Initially, Re was held at 2650 to allow transients to die out. The ramp was then started and allowed to increase over about one hour. Upon reaching Re = 2715 ($\Omega = 8.9077$ rad/sec, $\nu = 0.3001$ cm^2/sec), the ramp was halted and the flow allowed to develop. The flow remained steady for approximately 2400 endwall rotations (approximately 1.5×10^4 non-dimensional time units, where time is scaled by $1/\Omega$). At this point, small azimuthal oscillations became apparent. These oscillations are characterized by an asymmetric stretching and contracting of thin fingers of dye (fringes) at the downstream end of the second recirculation bubble. (The streamwise

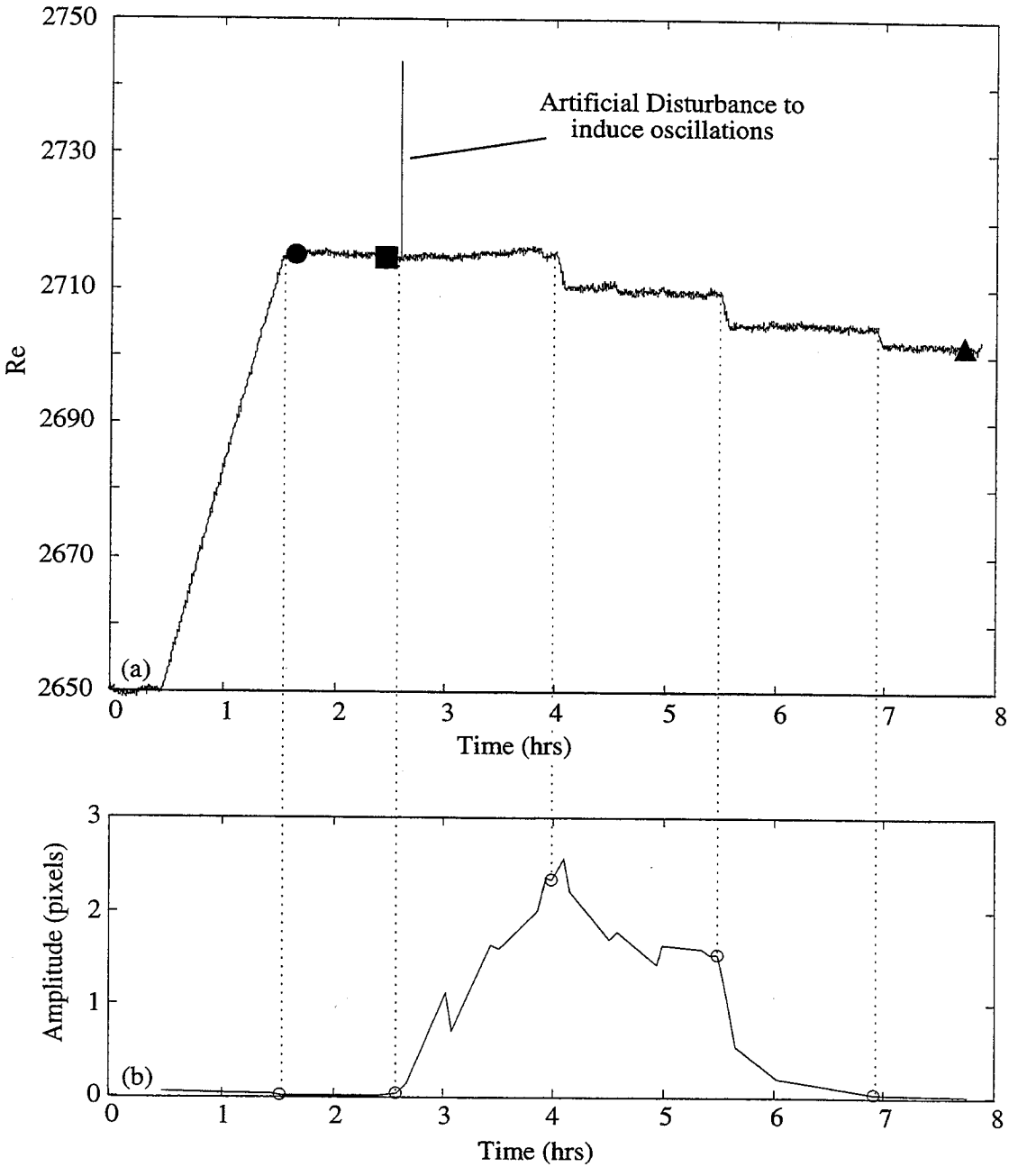

Figure 4-2 (a) Experiment Re history. ●, ■, and ▲ denote times of Fig. 4-3(a), Fig. 4-3(b), and Fig. 4-6, respectively. (b) Oscillation amplitude of hyperbolic fixed point during experiment.

direction is the axial direction from the stationary to the rotating endwall.) It is believed that this is an apparatus induced disturbance of the stable, *steady* solution and not a characteristic of the stable, *unsteady* solution. The rotational oscillations may be caused by small imperfections of the cylinder and misalignment of the centers of the disk and cylinder. An earlier series of runs showed more oscillations of this form, which were considerably reduced by realigning the rotating endwall. These oscillations are very different in nature to the axial oscillations reported below and by Escudier.[11] The fringe oscillations were watched for another 3000 rotations. Although the magnitude grew slightly, these azimuthal waves never progressed to the full, unsteady oscillatory motion. In another experiment, when Re was increased beyond 2720, the flow did not remain steady for more than 500 endwall rotations. The periodic motion would begin with an asymmetric folding and stretching of the upstream bubble around the downstream bubble. Eventually (~ 1200 endwall rotations later), the large, symmetric oscillations ensued.

It is important to point out that for Re = 2715 the downstream fringes were moving, but the bubbles did not migrate axially as they do for the unsteady flow. Figure 4-3 depicts the flow at the beginning and end of the constant Re flow. In Fig. 4-3(b), the upper fringe pattern is asymmetric and rotates in the azimuthal direction. During this whole time sequence, 5400 endwall rotations, the first stagnation point on the axis remained stationary. The temperature change between Fig. 4-3(a) and Fig. 4-3(b) was no more than the precision of the gauges (0.004 °C).

After the 5400 endwall rotations at Re = 2715, a controlled, large amplitude disturbance was applied to the steady flow. The Re was momentarily increased to 2744 and then reduced back to 2715. Unsteady oscillations began immediately and are characterized by an axial movement of the bubbles and a periodic stretching and folding of the upstream recirculation bubble around the downstream bubble. Figure 4-2(a) gives the time history of Re and Figure 4-2(b) gives the amplitude of the axial distance travelled by the bubble during one period of the oscillation. (Relative motions are measured by taking the cross-

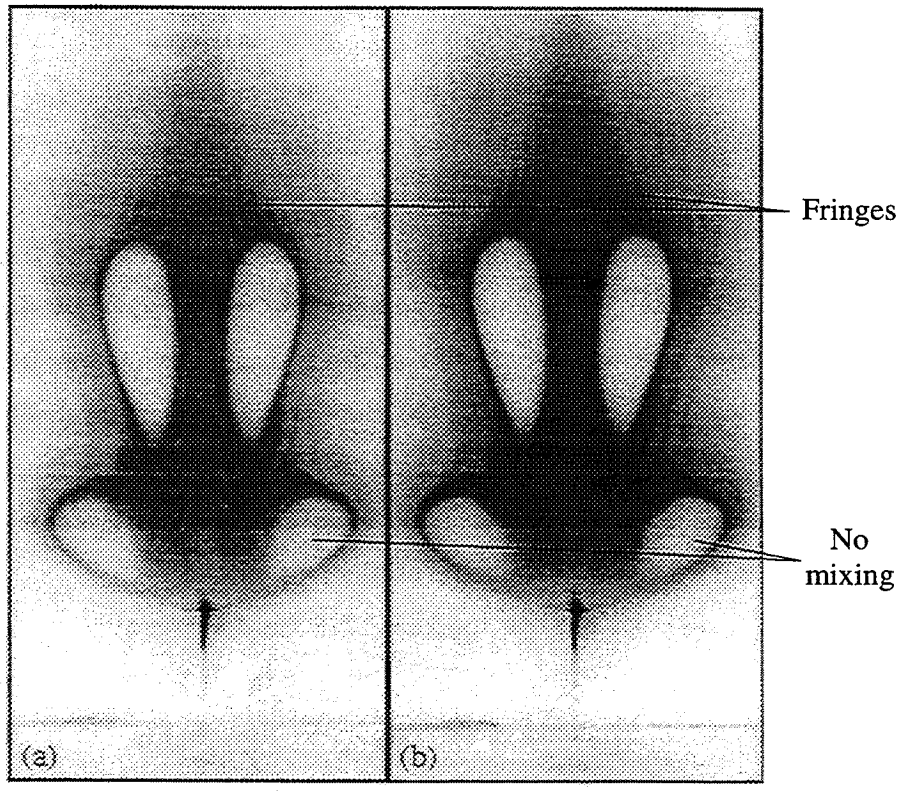

Figure 4-3 Re = 2715, H/R = 2.5; steady flows at (a) 5 and (b) 5400 endwall rotations from beginning of constant Re.

correlation between successive digital images. The change in the peak position of the cross-correlation is a good measure of the relative amplitude of oscillation. Appendix C describes the image processing techniques more fully.) This axial motion of the bubble is also depicted by Lopez and Perry[24] in the computations of the unstable manifold of the upstream hyperbolic fixed point of the flow (the periodic analog of the steady stagnation point). These oscillations reached a constant amplitude and were observed for about 7200 endwall rotations. Figure 4-4 portrays a non-dimensional period of this flow (using $1/\Omega$ as the time scale).

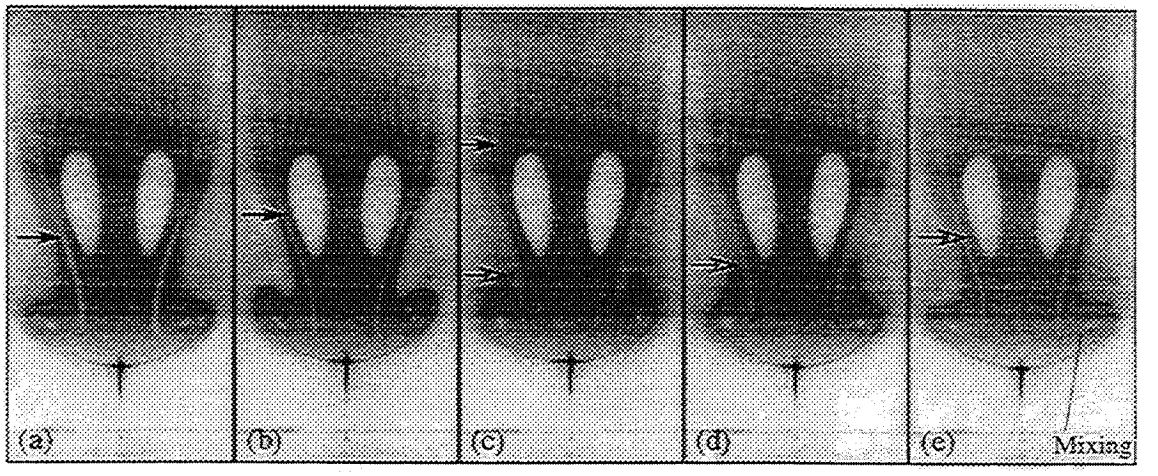

Figure 4-4 Unsteady flow, Re = 2690 and H/R = 2.5, at non-dimensional times Ωt (a) 0, (b) 9.2, (c) 18.4, (d) 27.3, (e) 36.5. Note the mixing, and the stretching and folding of the upstream recirculation bubble.

In Fig. 4-5, a close-up view of one side of the upstream recirculation bubble is shown over two complete periods. Due to the quality of the visualizations of the flow, this image is taken from a different experiment (§ B.2) that better displays the features within the recirculation bubble. After some digital enhancement of the images has been done, it is evident that regions within the bubble are kept clear of dye. Furthermore, the two outer zones of clear fluid are seen to orbit the central one completing a revolution for every two periods of the fundamental vertical oscillation. This phenomena is also observed in the numerical computations of Lopez & Perry[24] as depicted in their Fig. 6(a). Commonly known as KAM tori (after Kolmogorov-Arnol'd-Moser) and cantori, these regions are barriers across which fluid cannot pass.[35,24] Cantori provide only partial barriers to the flow, allowing small amounts of mixing over long periods of time. Evidence of KAM/can-

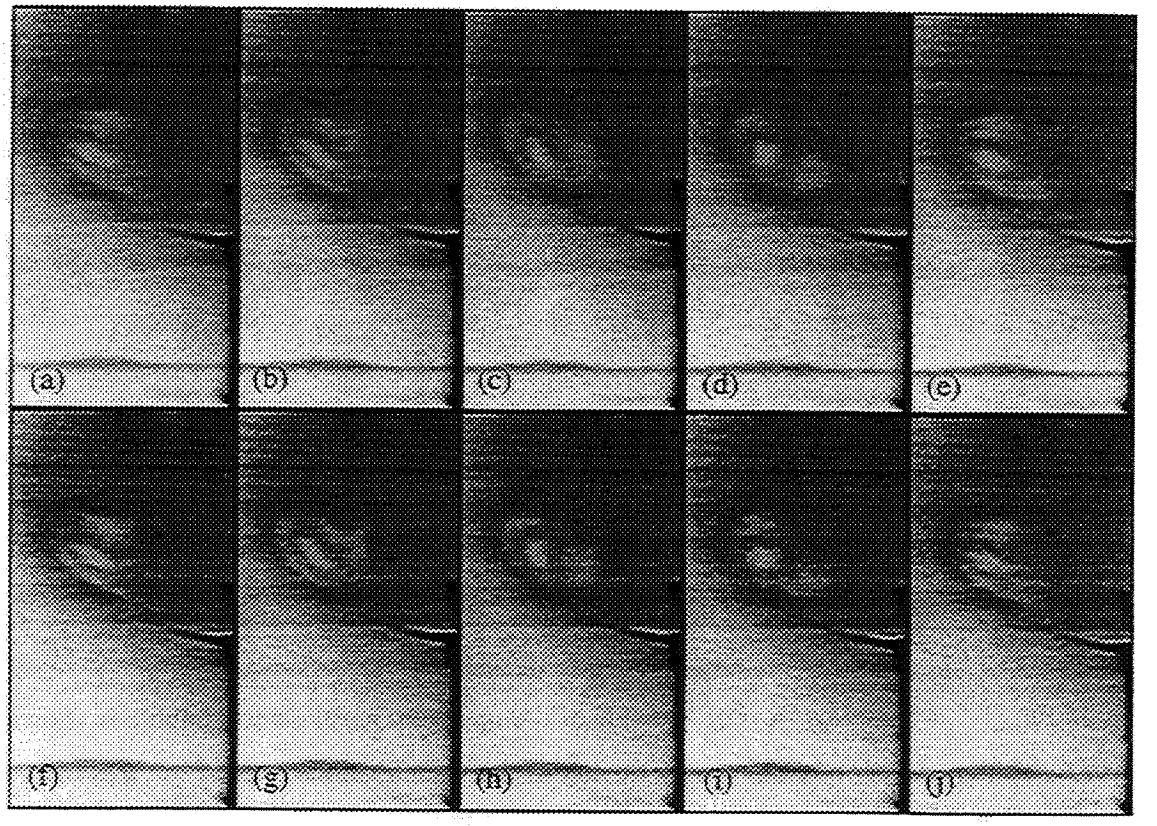

Figure 4-5 Close-up view of one side of the upstream recirculation bubble for Re slightly greater than Re_c and H/R = 2.5, at non-dimensional times Ωt (a) 0, (b) 8.1, (c) 16.1, (d) 24.2, (e) 32.3, (f) 40.3, (g) 48.4, (h) 56.5, (i) 64.5, (j) 72.6.

tori can be seen in Fig. 4-4 in the upstream, or lower, bubble. While mixing is going on inside the bubble, a small region of clear fluid can be seen into which no dye has penetrated.

Re was then reduced and held at several lower values: 2710, 2705, and 2702. At Re = 2710 (Ω = 8.8788 rad/sec, ν = 0.2996 cm^2/sec), the amplitude of the oscillations was smaller. This periodic flow was observed for 7200 endwall rotations. At Re = 2705 (Ω = 8.8624 rad/sec, ν = 0.2997 cm^2/sec), the amplitude reduced further and the

oscillations appeared asymmetric, although the hyperbolic fixed point continued oscillating very slightly and the bubbles were stretched and folded. At Re = 2705, the flow seemed to be shifting between the steady and unsteady flow states, most likely due to apparatus induced disturbances of the flow (see § 5.1). These fluctuations were observed for 6900 endwall rotations. Upon reducing Re to 2702 ($\Omega = 8.8580$ rad/sec, $\nu = 0.2997$ cm^2/sec), the flow became completely steady within 4000 endwall rotations (Fig. 4-6).

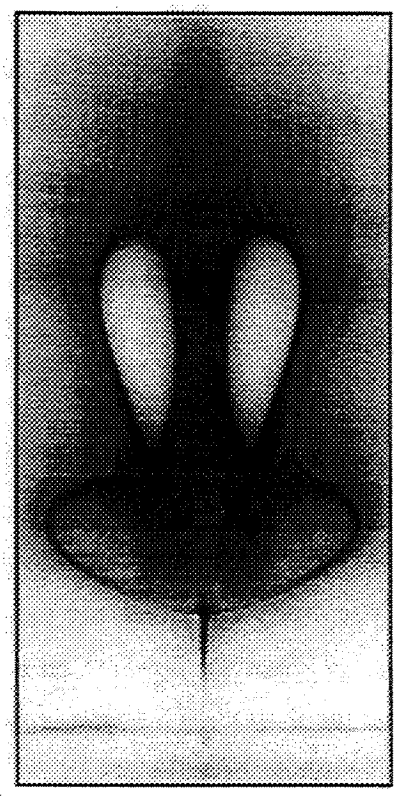

Figure 4-6 Re = 2702, H/R = 2.5; 4000 endwall rotations after reducing from 2705.

Some of the asymmetry observed in the experiment has been attributed to imperfections in the alignment of the cylinder and disk, and some is attributable to the cylinder not being perfectly cylindrical. These would contribute *real* asymmetries to the flow, as

opposed to *apparent* asymmetries. Even very small imperfections in the alignment of the dye injection port with the cylinder axis can provide an apparent asymmetry to the structure.[16,17,24]

The experiments were not able to continue the steady branch beyond Re = 2720, whereas in the computations it was continued to Re ≈ 3700, and not continued further due to the cost. The higher the Re, the smaller the increment in Re has to be to prevent the associated perturbation from upsetting the steady flow. It should be remembered that the perturbation levels in the apparatus have a finite value and are always applied to the flow through motor speed variations, temperature fluctuations, and geometry imperfections. In contrast, the main perturbation in the computations is due to the initial condition at a different Re. This is only present at t = 0 and can be made arbitrarily small; of course, the effects of truncation and round-off are always present. It is then not surprising that the continuation of the steady branch in the computations can be carried further than in the experiment.

4.3 Characteristics of Periodic Flow

In previous experimental investigations in a closed circular cylinder[11,27], it has been reported that the flow remains axisymmetric until well into the unsteady flow domain. The evolution of this flow has not been fully described, nor the dependence of oscillation frequency upon Re. This section describes the flow region from a Re of 2800 to approximately 5200. It is observed that the flow loses axisymmetry, but not to a degree to where the flow structures cannot be identified.

In these experiments, Re was slowly varied and held at several values as shown in Fig. 4-7. At each level, Re was held constant for at least 4500 endwall rotations (i.e., $\approx 2.8 \times 10^4$ non-dimensional time units). As the experiment evolved, dramatic changes occurred in the stretching and folding of the leading recirculation zone. For larger Re, the stretching becomes more pronounced. This is most visible in the upstream bubble region,

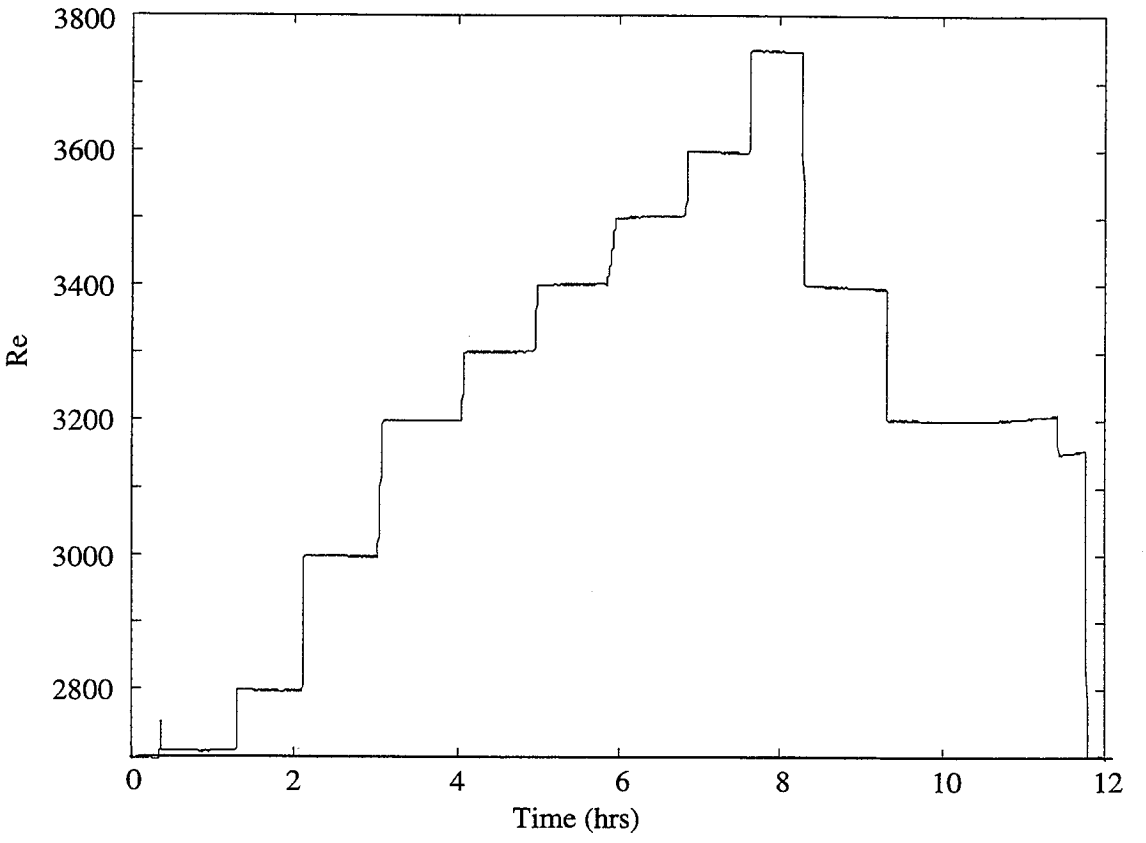

Figure 4-7 Experiment Re history for 2700 < Re < 3750.

which is stretched more with the lobes reaching farther along the axis. The cross-section of the bubble clearly indicates the stretching and folding of the dye-sheet forming the elongated lobes (fringes) typical of chaotic advection in a periodic flow (e.g. Re = 2800 in Fig. 4-8).

Upon reaching Re = 3000 (Fig. 4-9), several observations are made. First, it seems as if the dye-line emanating from the stationary endwall is precessing about the axis of the cylinder. As discussed previously (§ 1.3.2, page 9), even a small misalignment of the dye

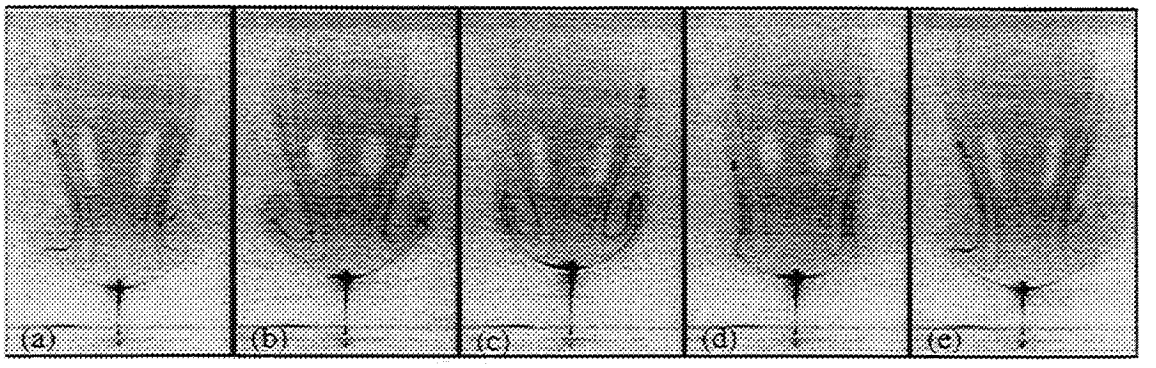

Figure 4-8 Re = 2800, H/R = 2.5 at Ωt (a) 0, (b) 9.2, (c) 18.3, (d) 27.5, and (e) 36.7.

injection port with the cylinder axis will cause apparent asymmetries.[16,17,24] Evidence that the flow is still axisymmetric is provided by the symmetric stretching and folding of the upstream bubble. Eventually, with increasing Re, this is not the case and asymmetries appear along the entire length of the breakdown structure.

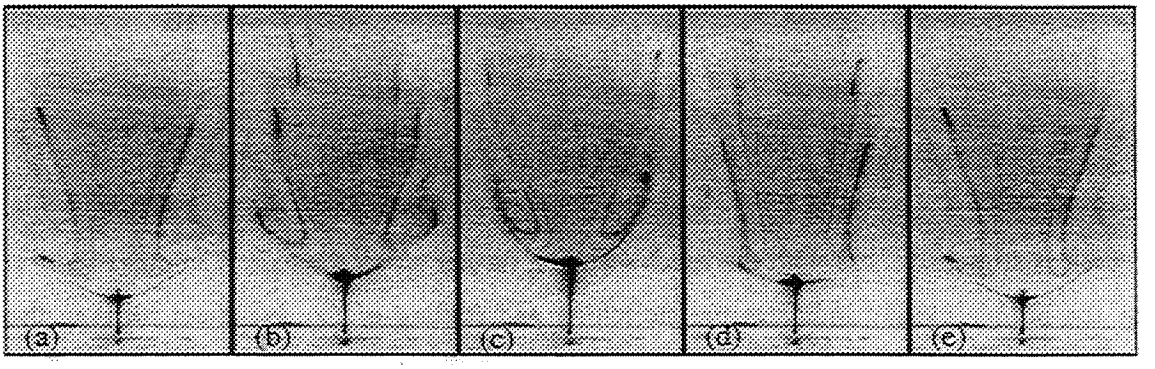

Figure 4-9 Re = 3000, H/R = 2.5 at Ωt (a) 0, (b) 9.2, (c) 18.3, (d) 27.1, and (e) 36.3.

The second observation when Re = 3000 is that the regions devoid of dye (presumably delineated by either KAM tori or cantori) in the downstream bubble have been considerably reduced in size. The KAM tori/cantori of the upstream bubble are no longer detectable by Re ≈ 2750; periodic orbits have broken up into higher order islands and there is increased tangling of the stable and unstable manifolds of the hyperbolic fixed points that dyed fluid is able to penetrate deeply, but not completely, into the inner-most regions of the bubble. By Re = 3200, the KAM tori and/or cantori have essentially disappeared, yet the breakdown structure still oscillates symmetrically as shown in Fig. 4-10.

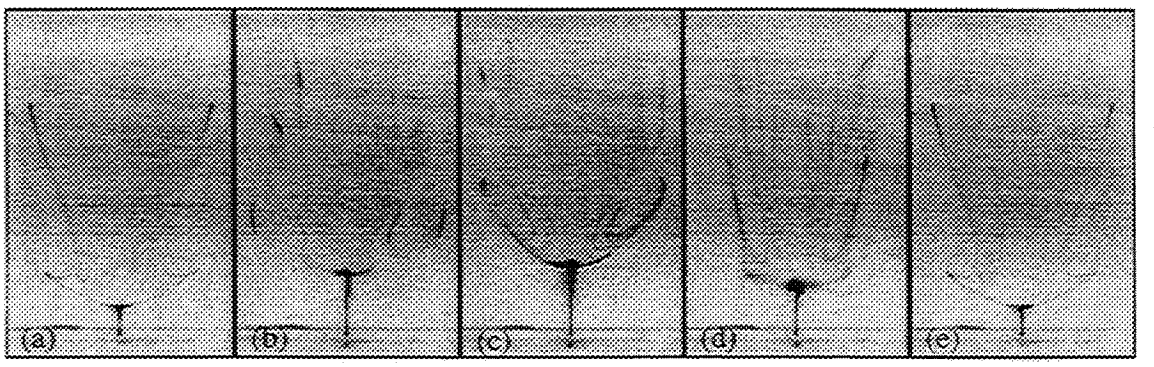

Figure 4-10 Re = 3200, H/R = 2.5 at Ωt (a) 0, (b) 9.0, (c) 18.1, (d) 27.1, and (e) 36.2.

Some asymmetries of the breakdown structure appear at Re ≈ 3400, just before a fundamental period change from $\tau_1 \approx 36$ to $\tau_3 \approx 57$ takes place in the region $3400 < Re < 3500$. The non-axisymmetric oscillation is manifested through the slightly uneven stretching of the upstream bubble. One side of the bubble reaches full extension just ahead of the other side. This asymmetry may arise due to the impending change in the characteristic period of the flow. The new fundamental frequency can be seen in Fig. 4-11. This figure shows the oscillation of the hyperbolic fixed point at Re = 3500 along with the power spectral density of the signal. It is observed from the power spectrum that the fundamental frequency of 0.01732 ($\tau_3 \approx 57$) is accompanied by a signal with a frequency of

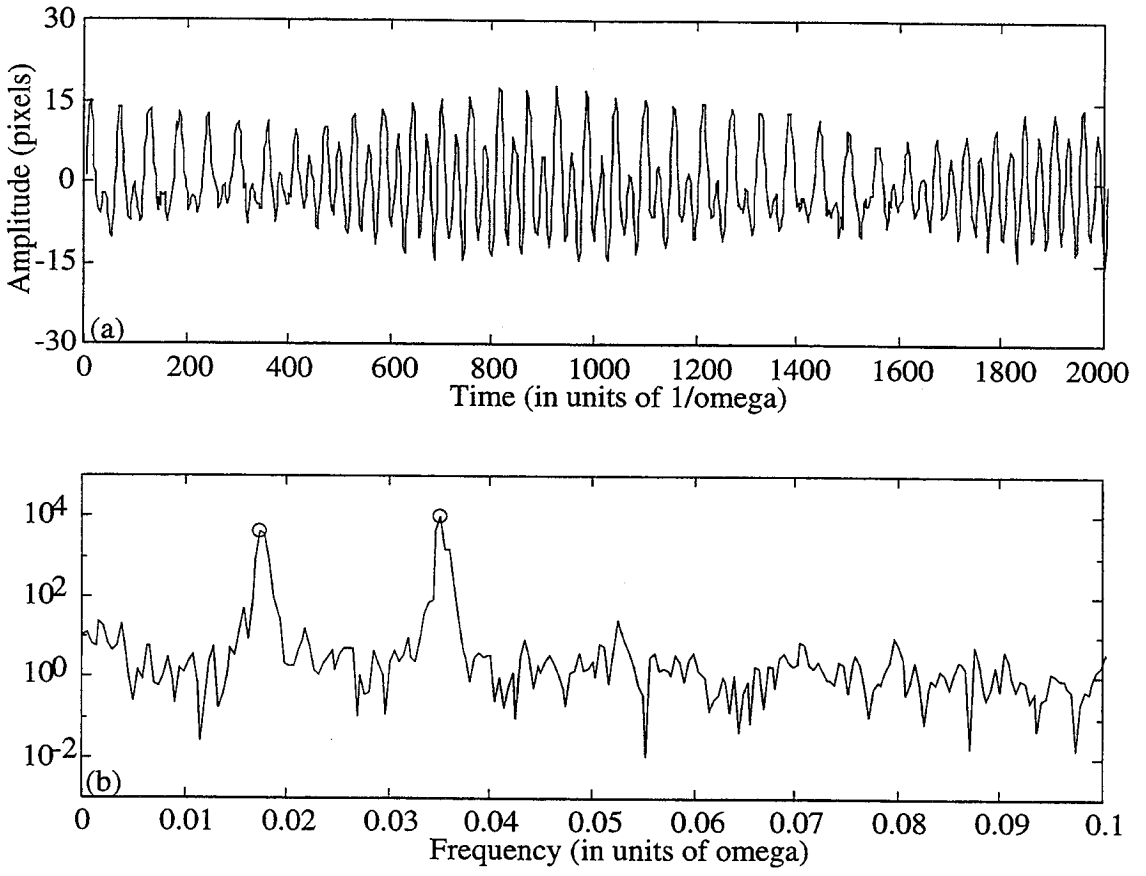

Figure 4-11 Re = 3500, H/R = 2.5 (a) Position of hyperbolic fixed point vs. Ωt, and (b) Power spectral density of signal.

0.03505 ($\tau_2 \approx 28$); this resembles a period doubling of τ_2, but is merely a harmonic. The distinction between a period doubling and an independent third flow is discussed later in this section. At a Re of 3600, the flow features from Re = 3500 are retained with similar frequencies. Another frequency, incommensurate with τ_3, is also apparent in the signals at these Re with a value approximated to be 0.0009 ($\tau \approx 1100$) that does not show strongly in

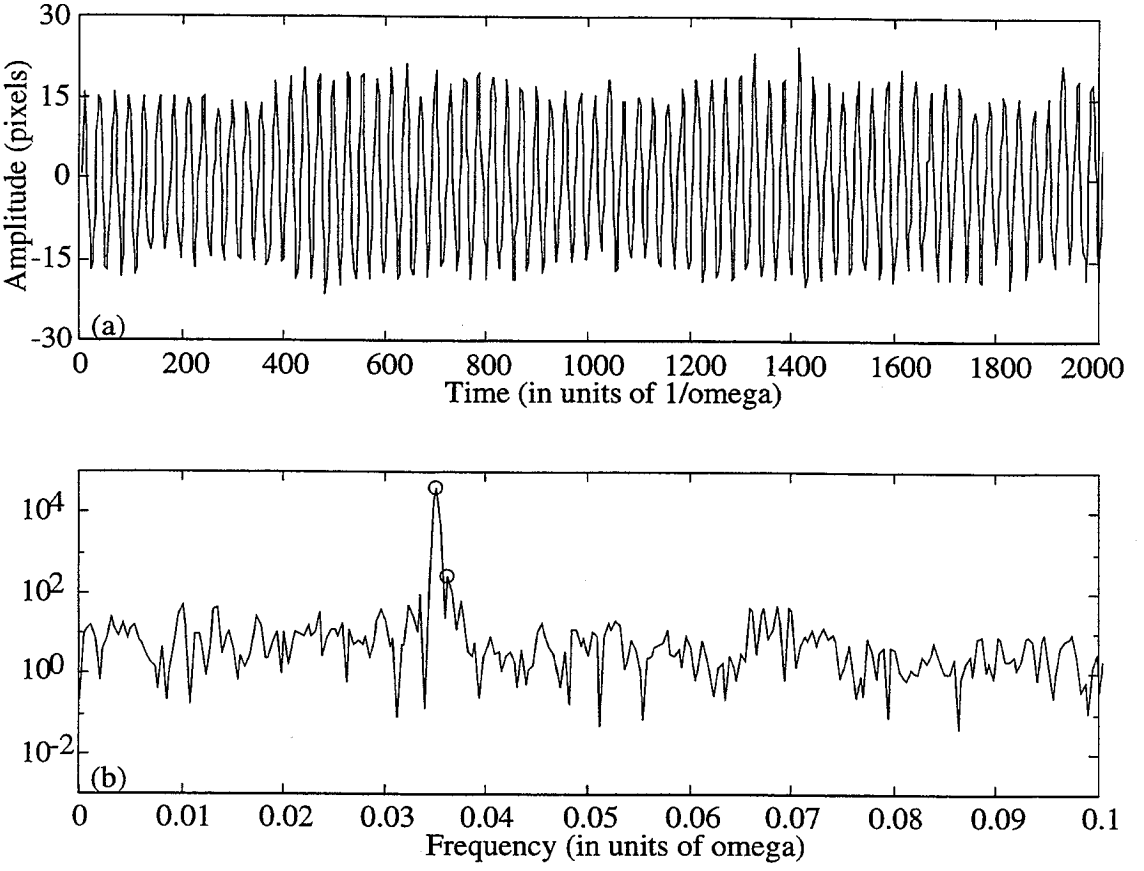

Figure 4-12 Re = 3750, H/R = 2.5 (a) Position of hyperbolic fixed point vs. Ωt, and (b) Power spectral density of signal.

the power spectral density because there are not enough cycles to resolve this low frequency. The frequency is evident in Fig. 4-11 as a long period modulation of the signal. It also shows up indirectly in the power spectral density as side-bands on the fundamental.

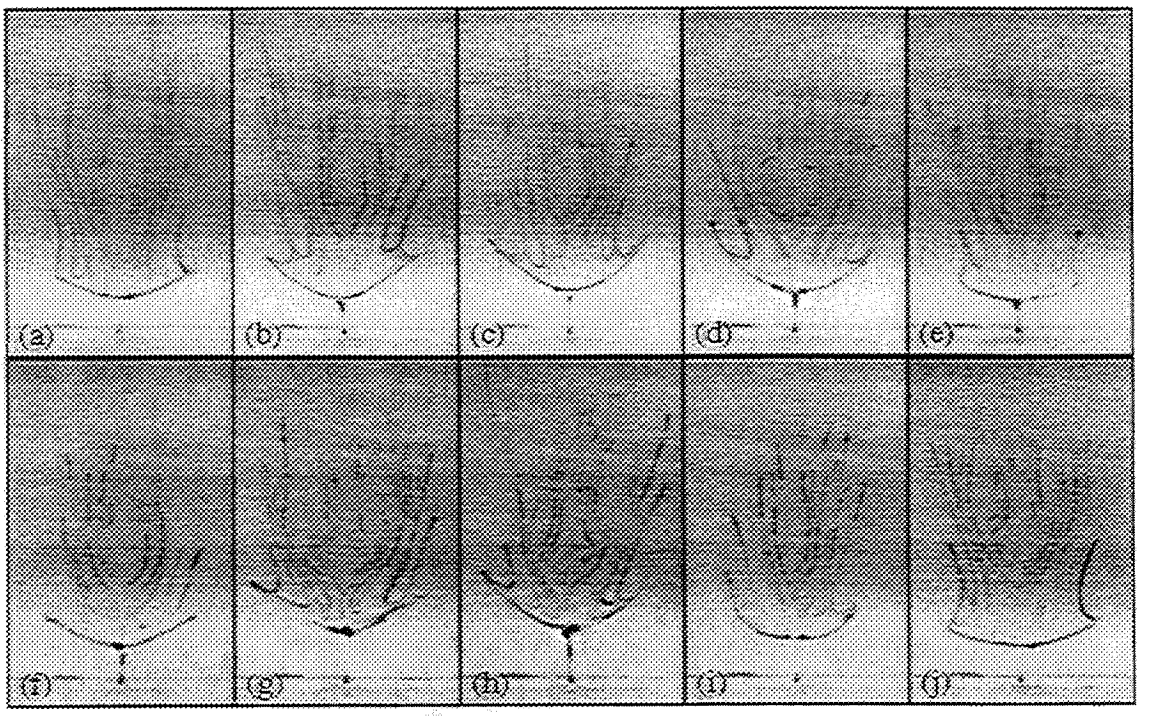

Figure 4-13 Re = 3600, H/R = 2.5 at times Ωt (a) 0, (b) 6.5, (c) 12.6, (d) 19.1, (e) 26.4, (f) 32.9, (g) 39.3, (h) 45.4, (i) 51.9, (j) 58.4.

Once a Re of 3750 is achieved, there is evidence that the τ_3 period and low frequency wave have died out. As seen in Fig. 4-12, the character of the oscillations has changed and the dominant frequencies are concentrated almost on top of each other at frequencies of 0.03503 and 0.03618 (τ = 28.5 and 27.6).

Although the flow contains many, but a finite, number of frequencies at Re's between 3400 and 3750, the breakdown structure retains a high degree of symmetry. Figure 4-13 is a sequence of images at Re = 3600 showing a complete cycle for the τ_3 = 57 mode of oscillation. This figure shows how evenly the unstable manifolds of the bubble are stretched and folded along the downstream part of the breakdown structure. Also shown in

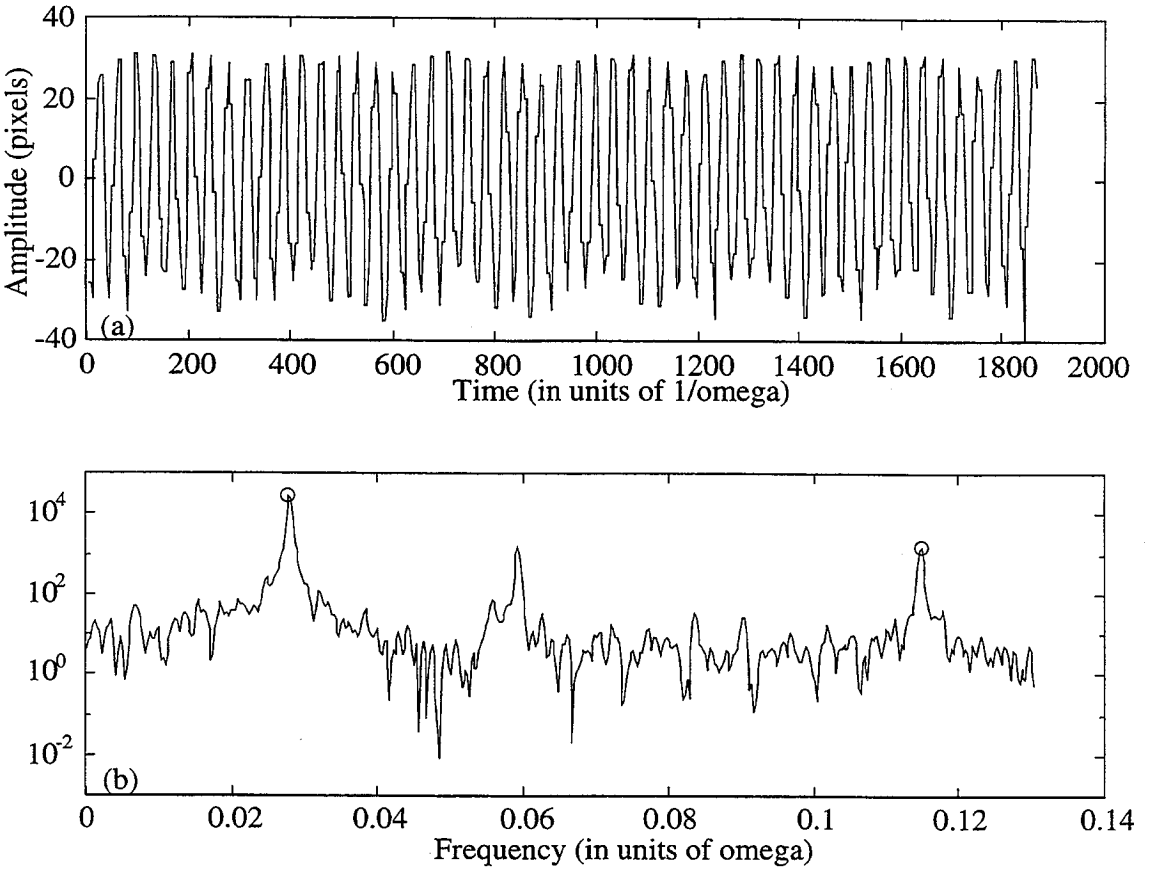

Figure 4-14 Re = 3400, H/R = 2.5 approached from lower Re (a) Position of hyperbolic fixed point vs. Ωt, and (b) Power spectral density of signal.

Fig. 4-13 is the jagged appearance of the recirculation bubble which is characteristic of the flow with a fundamental period of $\tau = 28.6$ in agreement with Fig. 6(b) of Lopez and Perry.[24]

After observing the flow at Re = 3750, the Re is reduced to 3400. Two observations are made. First, the fundamental period is τ_3 instead of τ_1 as it was when Re = 3400 was approached from lower Re. Second, the structure is affected by the long period signal as

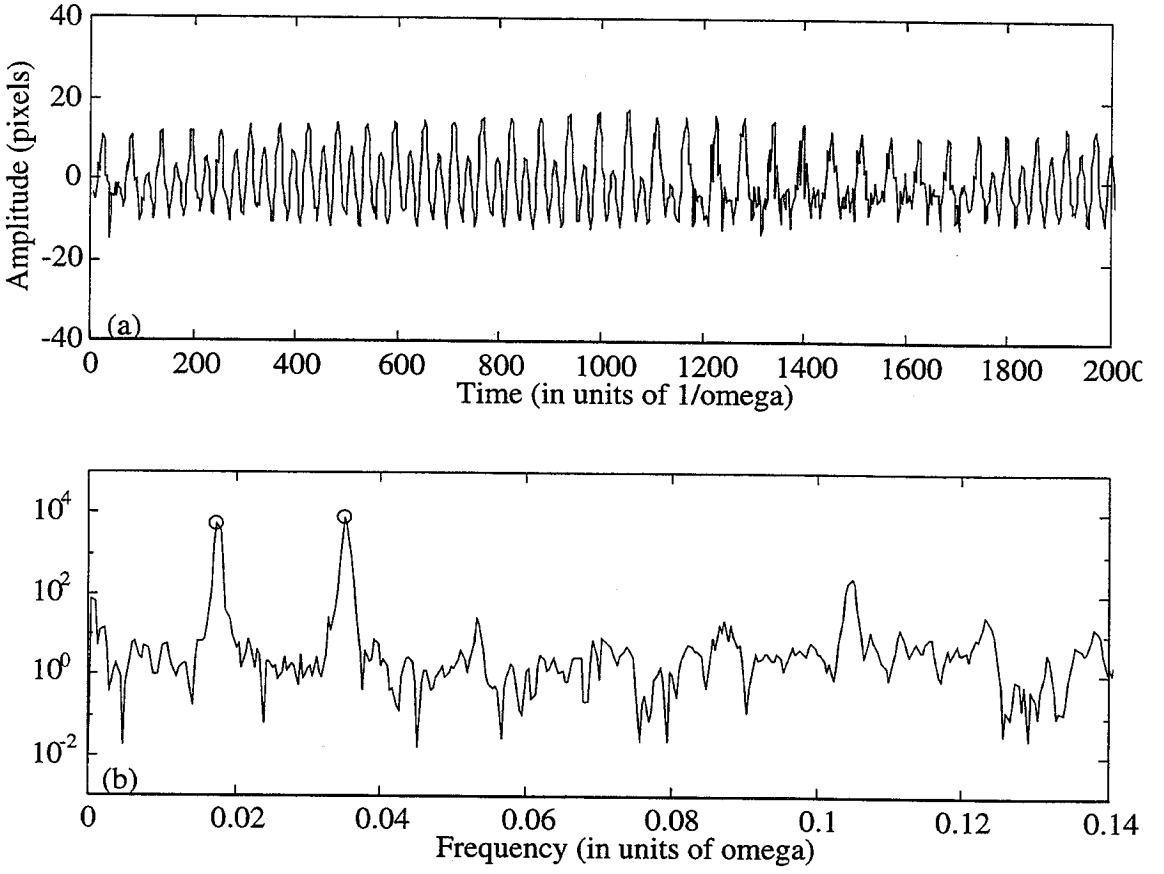

Figure 4-15 Re = 3400, H/R = 2.5 approached from higher Re (a) Position of hyperbolic fixed point vs. Ωt, and (b) Power spectral density of signal.

were the flows at Re of 3500 and 3600. Figures 4-14 and 4-15 show the two states at a Re of 3400 represented by the signal and the power spectral density. Figure 4-14 is the state as approached from lower Re, and Fig. 4-15 is the state as approached from higher Re.

Upon reducing the Re to 3200, the fundamental period remains at τ_3, but hints of the τ_1 period are beginning to show (Fig. 4-16). Reduction to Re = 3150 restores $\tau_1 = 36.2$ as the fundamental period.

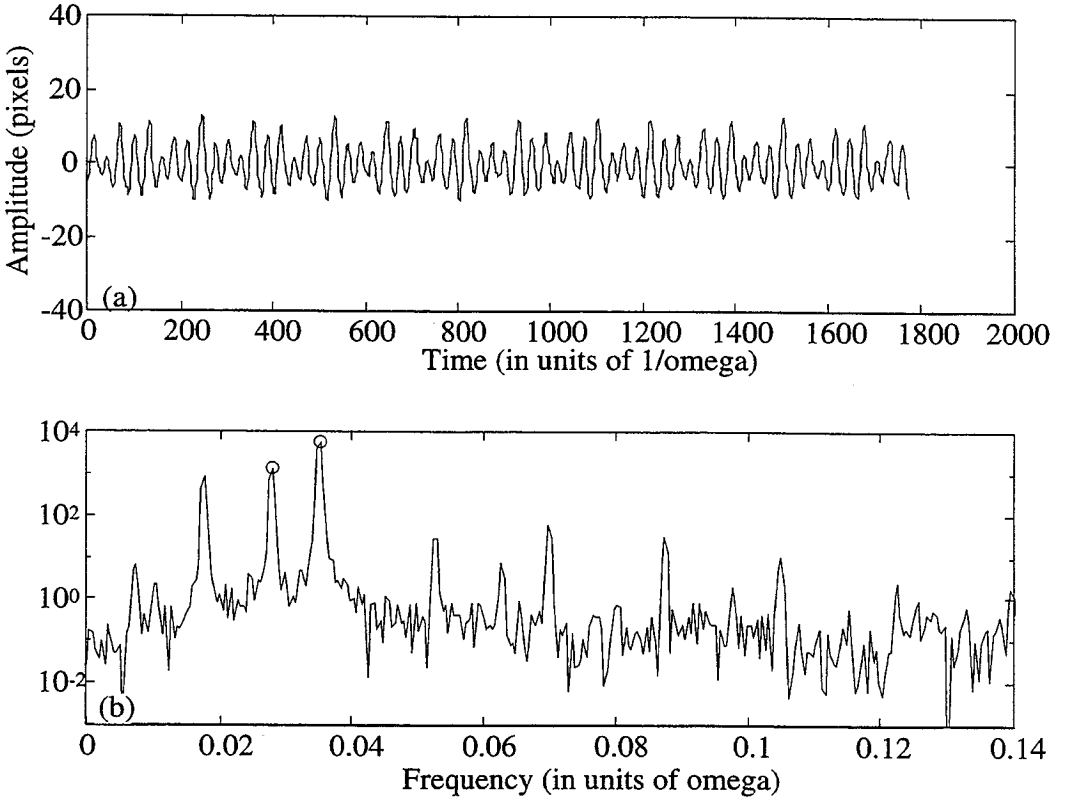

Figure 4-16 Re = 3200, H/R = 2.5 approached from higher Re (a) Position of hyperbolic fixed point vs. Ωt, and (b) Power spectral density of signal.

A separate experiment was conducted to search for hysteresis between τ_2 and τ_3 flows. The Re was slowly reduced from 3800 to 3600 and observed at points in between. The results of the downward sweep revealed that the τ_2 flow continues down to Re = 3625, below which the τ_3 period becomes dominant. The next part of this experiment revealed that the quasi-periodic τ_3 flow exists up to a Re between 3650 and 3675. With this addi-

tional information about the existence of the oscillation periods, a complete hysteresis diagram is drawn in Fig. 4-17. The most recent results of Lopez are also given. These data will be published in the near future.[36]

The distinction between a period doubling of the τ_2 flow and a distinct τ_3 flow is now addressed using results from the numerical simulations of Lopez. The observation that the τ_3 flow has a period twice that of the τ_2 flow suggests that they are related by a period doubling bifurcation. However, an examination of the phase portraits from the computed solutions reveals that the two flows are not connected by a supercritical period doubling bifurcation. If they were related in this way, then the τ_2 and τ_3 flow phase portraits would merge near the Re above which τ_3 dies out and τ_2 exists (Re $\approx$ 3730 for the computations). Figure 4-18 demonstrates that this is not the case. Figure 4-18(a) shows the phase portraits of the τ_2 oscillations for $3500 < Re < 4000$, and Fig. 4-18(b) gives the phase portrait of the τ_3 oscillations for Re = 3725. The notation v1 represents the azimuthal vorticity at one-third the radius and four-fifths the height, and v2 represents the azimuthal vorticity at two-thirds the radius and four-fifths the height of the cylinder. The phase portrait of the τ_2, Re = 3700 flow is radically different from that of the τ_3, Re = 3725 flow. Figure 4-19 shows phase portraits of the τ_1 flows and the τ_3 flow at Re = 3225. As shown, the two limit cycles for the Re $\approx$ 3200 flows also do not resemble each other. Neither the computational nor the experimental approach is able to unambiguously distinguish between disconnected branches and subcritically connected branches. Therefore, all that can be concluded is that none of the three periodic branches are connected via supercritical bifurcations.

At the Re examined here, the three-dimensional effects are small allowing extraction of useful data. Eventually, however, the three-dimensional perturbations prevent relevant analysis of the flow. The seemingly non-axisymmetric stretching of the upstream bubble leads to a more pronounced precession of the breakdown structure about the cylinder axis. This effect is not prominent for $Re < 4000$. The precession seems to cause the dye to be concentrated alternately on the axis of the cylinder then in the branches of the breakdown

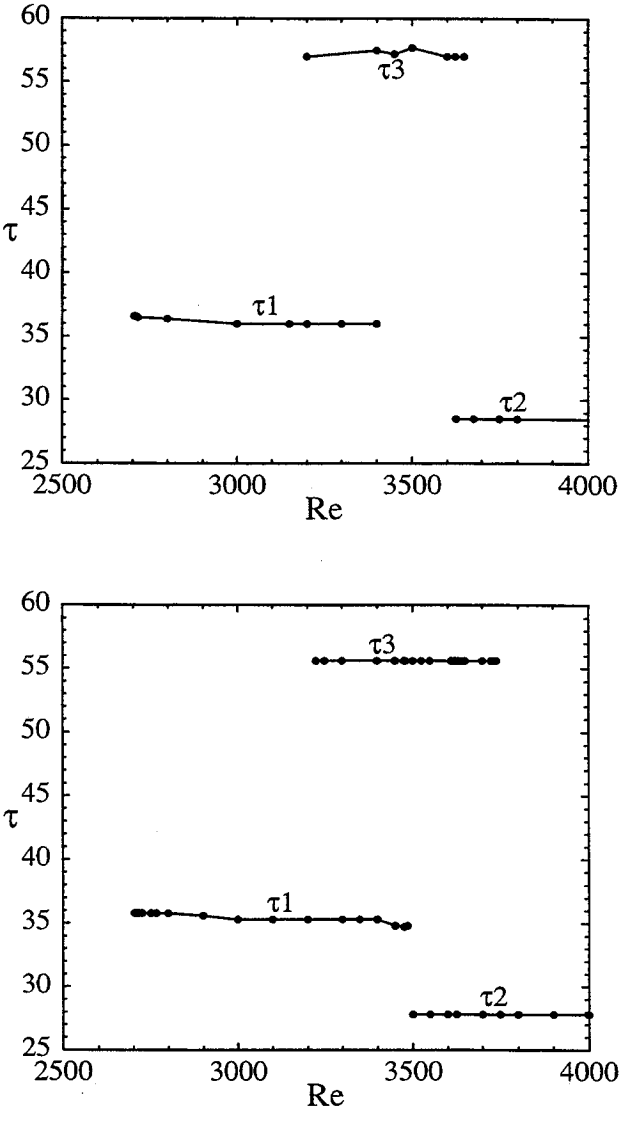

Figure 4-17 Hysteresis of oscillation periods. (a) experimental results, (b) numerical simulation data

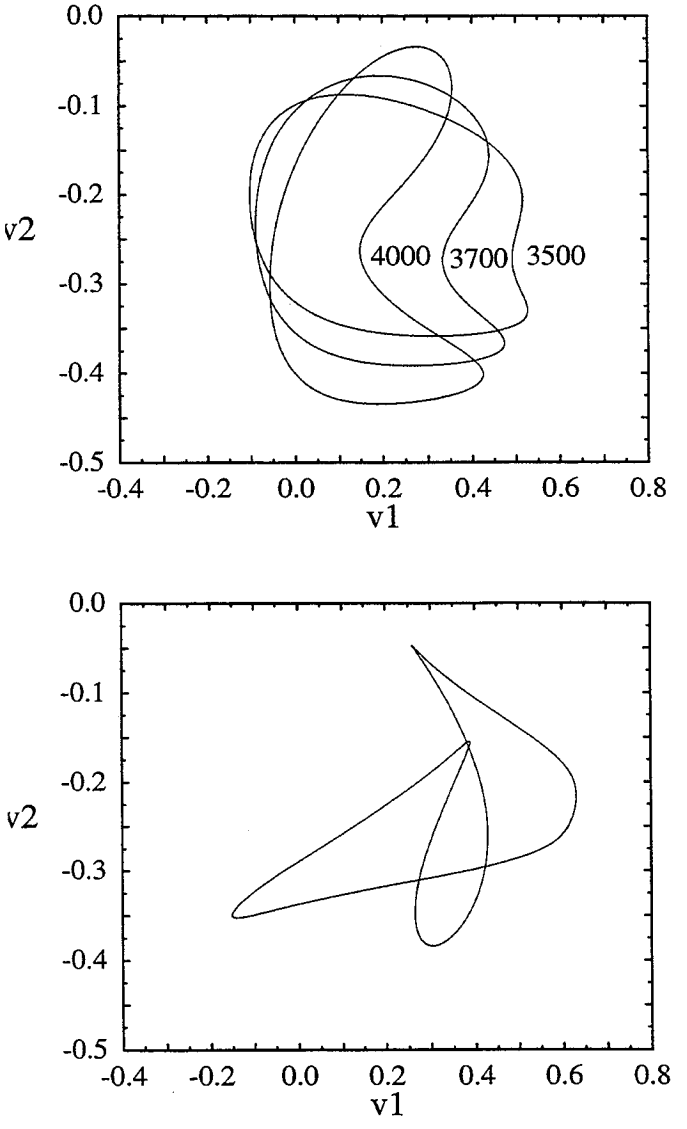

Figure 4-18 a) τ_2 limit cycles in (v1, v2) phase space for H/R = 2.5 and $3500 \leq Re \leq 4000$.
b) τ_3 limit cycles in (v1, v2) phase space for H/R = 2.5 and Re = 3730.

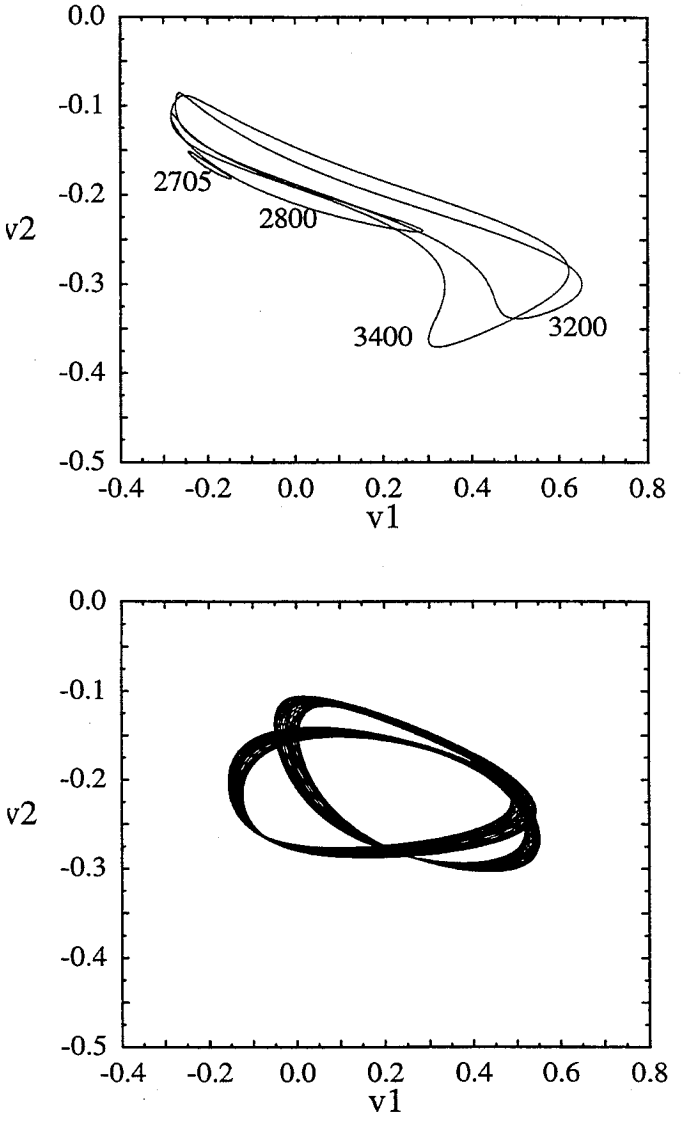

Figure 4-19 a) τ_1 limit cycles in (v1, v2) phase space for H/R = 2.5 and $2705 \leq Re \leq 3200$.
b) τ_3 limit cycles in (v1, v2) phase space for H/R = 2.5 and Re = 3225.

structure. Actually, the structure precesses about the center of the cylinder, and therefore, travels back and forth through the laser sheet. When the axis of the structure coincides with the laser sheet, the tree-like structure of the lower Re flow is visible. However, when the core of the breakdown structure is out of the laser sheet, the only fluoresced dye is located at the edges of the branches (or even further from the breakdown core) giving the impression of dye concentrated on the axis of the cylinder. Since this experiment did not continue beyond Re ≈ 3750, images are taken from a similar experiment that extended Re up to 7000. Figure 4-20 shows different stages of the precession of the structure about the cylinder axis over about 1400 non-dimensional time units. By Re ≈ 4700, the flow has become very three-dimensional and no useful data can be inferred from the images except that the non-dimensional period remains at ≈ 28 up to Re ≈ 5200. Beyond this Re, extraction of relevant data is very difficult.

The observation that the non-dimensional frequencies of the oscillations are essentially, to within measurement error bounds, independent of Re (the dynamic governing parameter) in both the experiments and the numerical simulations at H/R = 2.5, along with the observation from the numerical model[37] that the frequencies do vary with H/R (the kinematic governing parameter), suggest that the frequencies are modes of the finite cylinder, with the frequency for Re < 3500 being more fundamental than that of the higher mode found for Re > 3500. Furthermore, the ratio τ_1/τ_2 is approximately the ratio of the height to the diameter of the cylinder, or H/2R = 1.25. This seems to indicate a mode change from horizontal to vertical since the lower mode frequency ($1/\tau_1$) is shorter than the higher mode frequency ($1/\tau_2$), and the diameter (horizontal length) is shorter than the height (vertical length).

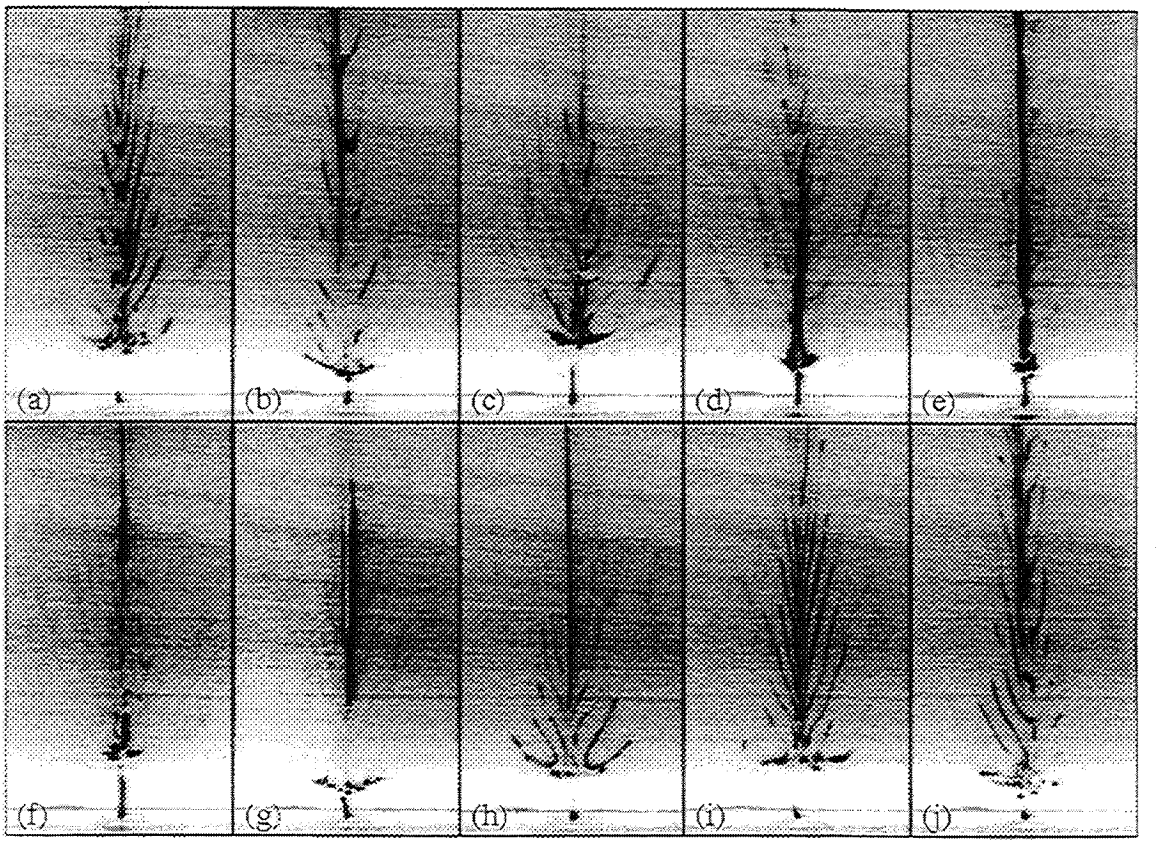

Figure 4-20 Re ≈ 4400 at Ωt (a) 0, (b) 154, (c) 308, (d) 463, (e) 617, (f)771, (g) 925, (h) 1080, (i) 1234, (j) 1388.

Chapter 5

Discussion

5.1 Characterization of Flow Imperfections

Due to the simplicity of the flow set up, many numerical studies have been implemented as an exercise in flow transition/bifurcation investigations.[13,20-28,37] Surprisingly, not many have considered in detail the transition from a steady to a periodic flow. The most detailed numerical studies have been done by Lopez. Unfortunately, no experimental results were available for comparison until the present work. Either the experimental (or numerical) investigator had assumed that the transition from steady to periodic flow occurred through a supercritical Hopf bifurcation based upon earlier work; or the nature of the equipment precluded investigation of this subtle region due to built in handicaps such as coarse motor control, unaccounted viscosity fluctuations through temperature deviations and geometrical imperfections. The effects of each of these perturbations send the system into largely unknown territory in terms of the bifurcation process, but through the diligent minimization of each of these disturbances, the consequences of each can be inferred.

A large effort has been put into precise motor control through the use of a phase-locked loop (PLL) controller (§ 2.4.1). Not only was smooth rotation required, but the ability to (nearly) continuously alter the rotation rate was indispensable. The results of a coarse adjustment are readily observed from the present work and that of Escudier.[11] (It is

not the purpose of this discussion to detract from the work of Escudier since it represents the most thorough and precise experiment of this type over a large range of the invariant space, and indeed, has greatly influenced the current study.) In the case of Escudier, the penalty for a coarse controller is the absence of any extension of the steady flow beyond the critical Reynolds number, Re_c. Even with the current level of precision, there were occasions, when the PLL was not accurately tuned, that the steady branch soon decayed into the periodic flow. The stability of the steady branch is so precarious that any type of relatively large disturbance will destabilize the flow. Although the PLL does an excellent job, the rotation cannot be completely disturbance free. At one point, with a disturbance on the order of one magnitude larger than the current jitter size, it was impossible to preserve steady flow above Re_c for more than a few thousand time units (measured in $1/\Omega$). The best obtainable fluctuation in motor speed causes a continuous perturbation of ~0.4 in Re.

Temperature fluctuations cause similar departures from the ideal as does motor jitter. This is readily seen through the relationship of Re with disk speed and temperature. The Re is directly proportional to both these parameters. This is easily verified with the motor speed since it appears explicitly in the calculation of Re. Temperature fluctuations are manifested through kinematic viscosity fluctuations in the determination of Re. Since viscosity is proportional to the negative of the temperature (Re is inversely proportional to viscosity), the Re is ultimately proportional to temperature. As temperature increases (decreases) there is a proportional decrease (increase) in viscosity. Therefore, a rise (or fall) in temperature causes a subsequent proportional rise (or fall) in Re. Due to the large thermal mass of the fluid, these fluctuations do not happen on the time scale of the disk speed fluctuations, but instead cause a continuous perturbation in Re through the constant increase or decrease in temperature. Any change in Re must be followed by a period of tranquility in order to allow transients associated with the change to die out. Obviously, this tranquil period never occurs, so the temperature perturbations are reduced by thermally isolating the experiment from the ambient environment. In a sense, the thermal box

adds thermal mass to the fluid and changes in temperature occur only over a very long time scale which can be further manipulated by adjusting the ambient temperature appropriately to influence the direction of change. With these measures, changes in temperature, and ultimately Re, can be made quite small if not negligible.

There are many types of geometrical imperfections, of which a few can be adjusted: alignment of disk and cylinder centers, disk wobble and endwall alignment. When the centers of the disk and cylinder are misaligned, the flow is no longer axisymmetric. This non-axisymmetry is observed in the radial stretching of one side of the breakdown structure. The fluid particles no longer follow a circular path with respect to a radial cross-section. Therefore, the fluid particle properties no longer depend only on axial and radial position, but also depend on the azimuthal position; the flow becomes three-dimensional to a certain extent. Effects are seen as a non-axisymmetric stretching and folding of the recirculation bubbles for the periodic flow state.

Disk wobble and endwall alignment present similar perturbations through a varying effective cylinder height. In either case, as the disk turns, the fluid is periodically forced downward besides being advected towards the cylinder walls. This type of forcing produces azimuthal waves throughout the cylinder. Visually, the structure supports the waves as a non-axisymmetric stretching and contracting of the fringes of dye at the downstream ends of the bubbles. Indeed, for large wobble and/or misalignment, these waves persist even for Re well below the first critical point. One would assume that the frequency of these waves would match the frequency of the disk except that the oscillatory nature of the enclosed fluid only allows modes of the cylinder to exist. Therefore, these waves have the same frequency as the unsteady flow itself. Since it is impossible to perfectly align the endwalls and have no wobble, this type of perturbation will always be present. At lower Re (below ~3000), the azimuthal waves caused by wobble/alignment are not visible but certainly present. As the Re increases, the boundary layer thickness decreases (boundary

layer thickness is proportional to $Re^{-1/2}$) corresponding to a larger effective wobble. This may be the cause of the apparent loss of axisymmetric oscillating flow at Re greater than ~3400.

Evidently, the point at which three-dimensional effects and eventually turbulence takes over is affected by the imperfections in the conditions used to implement this flow. In the case of experiments, the imperfections arise through many avenues including geometrical, thermal, dynamical and visualization properties. Numerical simulations generate perturbations in the choice of time-step size, grid resolution, and accuracy of Navier-Stokes approximations. Truncation and round-off errors contribute to the imperfect realization of the flow as well. As can be seen, a truly ideal flow of this type cannot be created either experimentally or numerically.

5.2 Bifurcation Events

Now that it has been established that the ideal flow has not been studied, the discussion turns towards non-ideal events near bifurcation points. A very thorough study of these phenomena has been carried out by Benjamin[29,30] especially with regard to Taylor-Couette flow. A general overview of these bifurcation events has been presented by Drazin and Reid[38] who tie together some of the work done in relation to hydrodynamic stability over the last few decades. In theory, for an ideal, viscous, and symmetric flow, the development of the flow as one of the parameters is varied (usually the Re) will exhibit a Hopf bifurcation event when the steady flow loses stability and periodicity prevails. However, this state is a specific condition and not the generic characteristic displayed by most realizable systems.

In order to pursue this reasoning, the Hopf bifurcation must be described, particularly the supercritical form which is generally believed to dominate this flow. The varying parameter will be Re, although this is not necessarily the case for all viscous flows. At low values of the Re, a stable and steady flow exists, but as Re is increased to a critical value, a

bifurcation event occurs. For supercritical bifurcations, the steady solution is no longer stable and the solution branches onto periodic curves as shown in Fig. 5-1.[38] The ordinate represents the amplitude of a parameter in the flow (e.g. position of hyperbolic fixed point, velocity at a point in the flow, vorticity at a point in the flow, etc.), and the abscissa delineates Re. However, this diagram undergoes a transformation when perturbation or imperfections are introduced. Even a break in the symmetry of the flow will cause an alteration in the bifurcation diagram. This morphogenesis is best diagrammed by Benjamin[29] and is reproduced here as interpreted by Drazin and Reid[38] in Fig. 5-2. The solid curves represent stable flows whereas the dashed ones imply unstable solutions. This morphogenesis of events is the general result found by Benjamin, but confirmed in a finite Taylor-Couette experiment with the morphogenesis parameter being the width between the endwalls. (a) shows that the primary solution continues with increasing Re indefinitely unless a destabilizing perturbation is applied causing the solution to "jump" to the lower part of the 'c' curve (secondary solution). In (b), the primary locus becomes folded with an unstable solution between the upper and lower portions of the 's' curve. This signals a hysteresis loop with respect to Re in the flow. (c) portrays a transcritical bifurcation which is probably the closest thing to a supercritical Hopf bifurcation this flow would experience. (d) is similar to (a), but flipped with respect to the abscissa.

> Thus the primary solution of an imperfect system does not become unstable at all; it changes continuously with R slowly as R increases below R_c and more rapidly as R increases above R_c. In short, there is no abrupt change in the character of the primary solution as R increases. The other stable solution, called the secondary solution, which exists for $R \geq R_1$, can be realized only by a strong disturbance of the primary solution. If R decreases slowly after the secondary solution has been realized, then one expects a 'catastrophe', or sudden transition to the primary solution, as R decreases through R_1.
>
> (From Drazin and Reid, p 413) Here, R is Re and $R_1 = \mathrm{Re}_c + \varepsilon$.

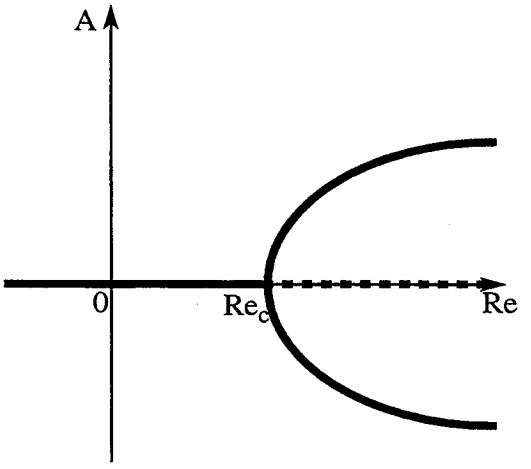

Figure 5-1 Supercritical bifurcation. – Stable, -- unstable.

Now it can be seen that cylindrical swirling flow exhibits much more complicated bifurcation phenomena than originally thought. Similar to Taylor-Couette flow, it may be possible that the bifurcation events change as H/R is varied. Presently, there are no known studies conducted on this topic. Furthermore, it is difficult, maybe even impossible, to say which of the diagrams in Fig. 5-2 represent the bifurcation phenomena encountered in this study.

Let's recall the salient features near the first critical Re ($2702 < Re < 2705$): hysteresis between a steady and unsteady flow, a relatively smooth transition from unsteady to steady flow as Re is reduced from above 2705, and no steady flow above $Re \approx 2720$ for any significant time. Because of the hysteresis event encountered, one would be inclined to point out diagram (b) as most representative due to the hysteresis present in the 's' curve. Yet, this would imply hysteresis between two slightly different steady states instead of one steady and one unsteady solution. Perhaps (c) is more characteristic of the flow. Indeed, if the upper curve represents unsteady flow, then hysteresis is accounted for and the primary

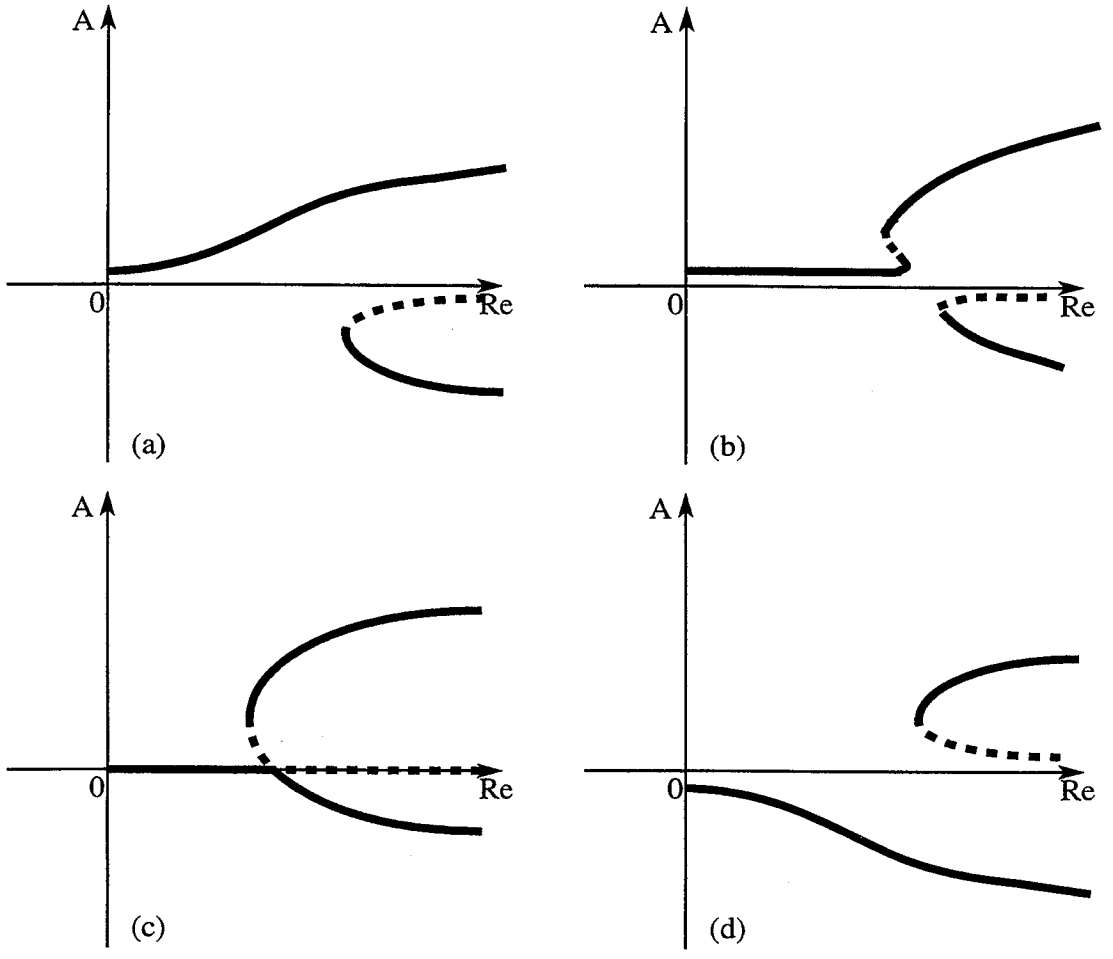

Figure 5-2 Sketch of the morphogenesis of the bifurcation curves for imperfect supercritical stability as the imperfection changes.

solution would end at Re ≈ 2715 with the upper, stable unsteady branch reaching back to Re ≈ 2705. But the transition from unsteady to steady flow would be an abrupt jump in amplitude, unlike the smooth transition witnessed. Diagrams (a) and (d) seem to offer the best alternative. If the basin of attraction of the steady solution at Re > 2705 decreases with increasing Re, it may be hypothesized that the always present minimum perturbation level in the experiment is too great to allow the steady flow to survive above 2720 for any

reasonable amount of time. Lopez's study[26] showed the existence of a steady solution up to a Re of at least 3700. His investigation also showed that the basin of attraction shrinks as Re is increased evidenced by the smaller allowable increase to preserve the steady flow at higher Re.

5.3 Influence of Imperfections upon Bifurcation Sequence

The discussion now turns to connecting the various imperfections with the possible transformation in the bifurcation sequence. First to be examined is the disk jitter, which provides a continuous perturbation to the flow and may destabilize the steady solution allowing periodic structures to appear. Large jitter will certainly destroy the steady solution almost as soon as Re_c is surpassed giving the appearance of a supercritical or slightly transcritical bifurcation. The steady branch will be deemed unstable since no significant amount of time would pass before unsteady flow dominates.

Since temperature fluctuations happen on a long time scale, their effects are usually nullified. But, if one is not careful, the temperature rise or fall may provide a destabilizing or stabilizing effect, respectively, if allowed to occur continuously without precautions to keep the Re held steady at the desired point. From these imperfections no helpful insights can be drawn as to the effect upon the bifurcation events.

For the non-axisymmetric flow (disk and cylinder centers misaligned), the steady flow seemed more stable beyond the critical Re than did the more axisymmetric flow. The evidence is inconclusive since in re-aligning the disk, it may be that some other parameters were made less ideal, but the offset flow seemed better able to withstand the same perturbation level endured by the centered flow. Perhaps this type of offset increases the domain of attraction of the steady flow by moving the primary solution curve farther from the secondary solution curve.

Periodic forcing (disk wobble/non-parallel endwalls) seem to cause the most apparent change in the bifurcation sequence. Since the forcing manifested itself in the fluid not at the frequency of the disk but at the fundamental frequency of the cylinder, the unsteady flow was being encouraged through the excitation of its fundamental mode. (This could also be the case for disk jitter since it also would excite the fundamental mode.) Forcing of the unsteady flow would severely limit the range and duration of the steady flow beyond Re_c. This would resemble at least transcritical bifurcation if not supercritical Hopf bifurcation.

Although there are definite imperfections in the circular cylinder, it is impossible with the given results to formulate the effects upon bifurcation events since no other cylinder was included in the experiment.

Chapter 6

Conclusions

In light of the discussion of the previous chapter, it stands to reason to expect a much more complicated flow transformation sequence than seen before. Indeed, although the experiments reported herein dealt only with one slice of a rich and diverse flow domain – namely, H/R = 2.5 – it has been found that the cylinder with one rotating endwall supports hysteresial flows with at least primary, secondary, and tertiary branches. These findings have never been observed in previous experimental investigations of this type.

6.1 Continuation of the Steady Flow

The first set of experiments lend support to the recent numerical results of Lopez.[26] It is apparent that two flow states exist beyond a critical Reynolds number: a stable steady and a stable periodic state. Steady flow is observed up to Re = 2715 and periodic flow exists down to Re = 2705. Lopez[26] originally reports a critical Re of approximately 2670 above which two states exist. In more recent numerical simulations not yet published, Lopez has used a stretched grid to resolve the boundary layer flow better and reduced the time-step size, which in turn affected the critical Re, the most recent being 2705 in very good agreement with the experiments. Although the experiments cannot sustain a steady flow for long periods beyond Re = 2720, Lopez has extended the steady solution to

Re = 2800. It is suspected that the steady branch extends further, but due to the cost in computing the solutions, Lopez has not done so. In his earlier work with a regular grid and larger time-step, Lopez[26] was able to extend the steady branch to a Re of 3700.

Escudier[11] reports periodic flow at H/R = 2.5 only for Re > 2680, but does not find any steady flow above this Re. Tsitverblit[25] ultimately finds that the steady flow loses stability to a periodic flow for 2630 < Re < 2650. He finds that the two solutions do not exist at the same Re. This estimate of Re_c is low, indicating a coarse time-step and, therefore, a large perturbation. Upon reducing the time-step and refining the mesh, some numerical studies[27,39] found an upward modification of Re_c.

6.2 Characteristics of Periodic Flow

The second set of experiments regards the nature of the oscillation of the unsteady flow. These investigations further support the concept of complicated flow processes introduced earlier. Not only were two other regions of hysteresis found – between two periodic flows this time – but a third periodic flow was discovered. Periodic flow with $\tau \approx 36.1$ exists up to Re ≈ 3400. Between a Re of 3400 and 3500, the period of oscillation changes to $\tau \approx 57.3$ (§ 4.3). Oscillations with $\tau \approx 57.3$ exist up to Re ≈ 3675 at which point a pure period of $\tau \approx 28.6$ exists in the flow. Reducing the Re showed a return of $\tau \approx 57.3$ for $3600 \leq Re \leq 3200$. Reducing Re to 3150 restores $\tau \approx 36.1$ as the oscillation period for the flow. Lopez has numerically duplicated these results in a paper soon to be published[36], with more precise values of the critical Reynolds numbers.

In summary, the known regions of hysteresis are listed in the table below:

Table 6-1 Hysteresis events for H/R = 2.5 (τ_1=36.1, τ_2=28.6, and τ_3=57.3)

Re range	Possible τ
2705 - 2715	0 and τ_1
3200 - 3400	τ_1 and τ_3
3625 - 3675	τ_2 and τ_3

Appendix A

Phase-Locked Loop (PLL) Motor Controller

PLL's have been around for quite some time used in applications such as FM receivers, color television, missile tracking loops, space telemetry, and AM demodulation.[32] The superior speed control accuracy of the PLL, which regulates motor frequency up to 0.002% of the desired frequency[33], has proven ideal to use in this situation. In a normal servo-motor control loop, the feedback is provided by a tachometer in the form of a voltage proportional to the frequency of the motor. Therefore, the speed accuracy is dependent on the quality of the signal provided by the tachometer which is a generator attached to the motor shaft in this case. The tachometer voltage is inherently noisy and greatly limits the resolution of the signal. In a PLL, however, the feedback is a digital signal that precludes distortion due to noise, thereby providing a very accurate indication of position which is compared to a reference position. If the reference position is continuously ramped, the result is a very accurate frequency. Since the output is locked to the reference signal, the motor is forced to rotate at the same accurate frequency as the reference.

The basic block diagram of the PLL is shown in Fig. A-1. The voltage controlled oscillator (VCO) signal is compared with the reference signal by the phase detector. Depending on which signal is leading in phase, the output voltage of the phase detector is either increased or decreased. The output signal, or error signal, has noise and the refer-

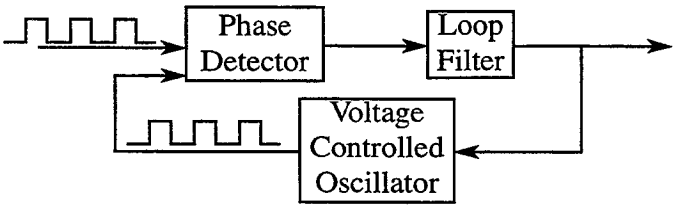

Figure A-1 Block diagram of PLL

ence signal removed by the loop filter which also determines the stability and dynamic performance of the loop. The filtered voltage drives the VCO and alters its frequency in such a way as to minimize the phase error between the VCO and reference signals.

In this application the VCO is the motor/encoder combination, and the loop filter has three jobs: conversion of the digital commands from the phase detector to analog voltages, removal of high frequency and noise signals, and stabilization of the loop. With the addition of the dumbbell, the loop stabilization became more sophisticated. Figure A-2 depicts the block diagram of the motor controller loop.

For the phase detector, a Motorola MC4044 phase-frequency detector chip is used. As given by the chip's data sheet, the transfer function of the phase detector, K_ϕ, is approximately 0.12 volts/rad and can be written as:

$$\frac{D-U}{\Theta_i} = K_\phi \tag{A-1}$$

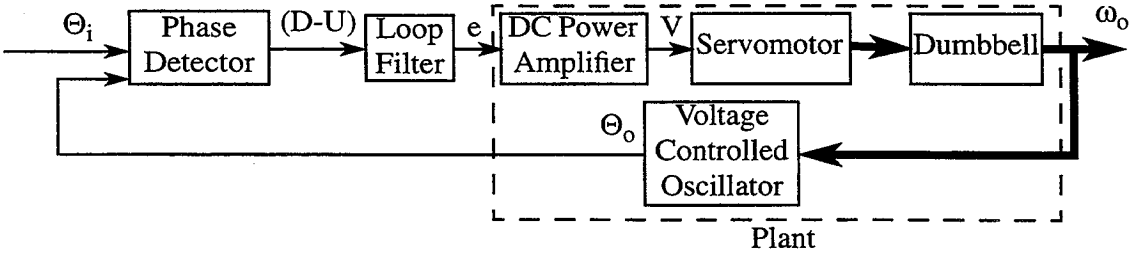

Figure A-2 Block diagram of motor control system

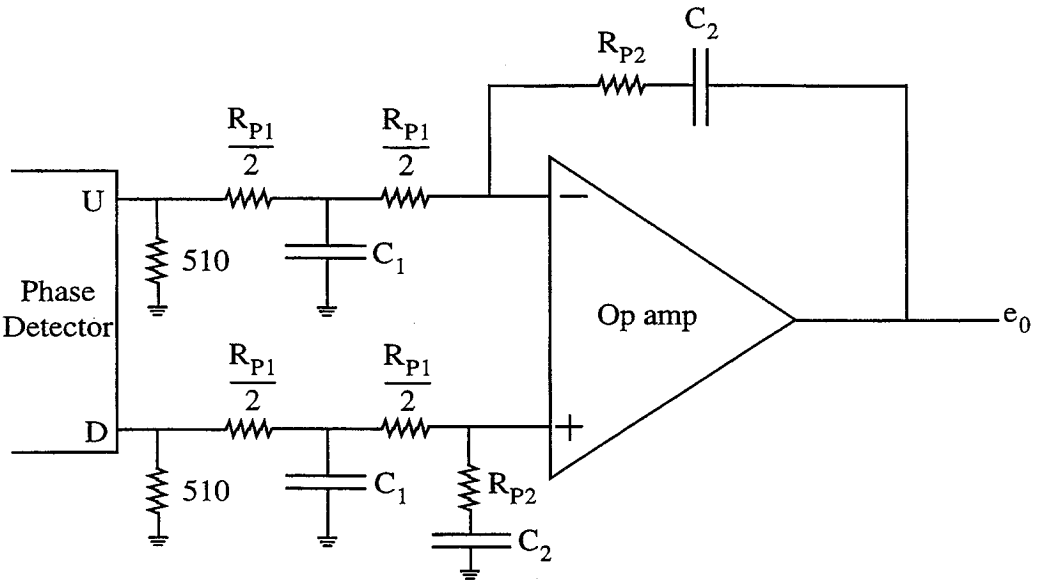

Figure A-3 Low-pass filter/charge pump network

The filter is made up of several circuits: a combination low-pass filter and charge pump, a lead-lag filter, and a gain adjustment network. The job of the low-pass filter/ charge pump is to convert the digital signals from the phase detector to an analog signal without high frequency components. Figure A-3 is a schematic of the low-pass filter/ charge pump circuit. The transfer function is found to be:

$$\frac{e_o}{D-U} = \frac{1+\tau_{P2}s}{\tau_{P1}s\,(1+\tau_{LP}s)} \tag{A-2}$$

where

$$\tau_{LP} = \frac{R_{P1}C_1}{4}$$

$$\tau_{P1} = R_{P1}C_2$$

and

$$\tau_{P2} = R_{P2}C_2$$

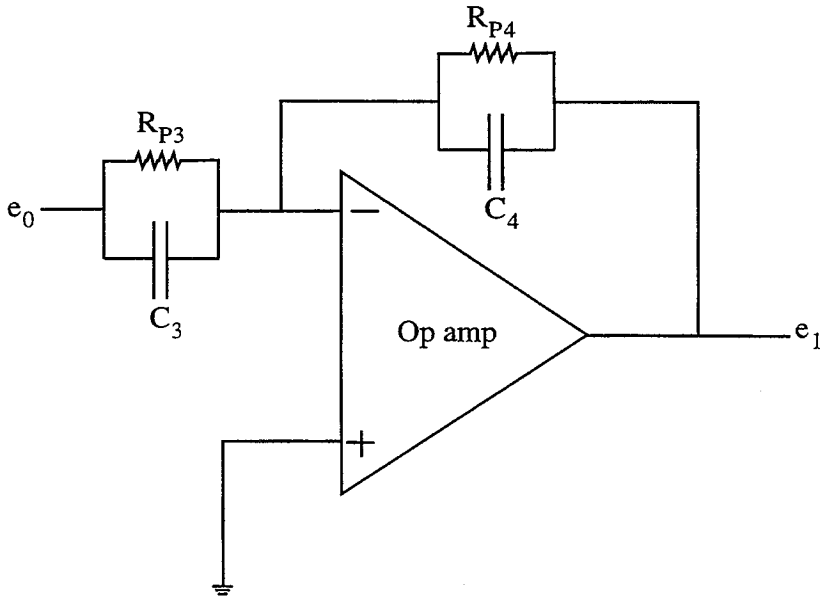

Figure A-4 Lead-lag filter circuit

The lead-lag filter is shown in Fig. A-4 and can be represented by the following transfer function:

$$\frac{e_1}{e_0} = -\frac{C_3}{C_4} \cdot \frac{(1 + \tau_{P4}s)}{(1 + \tau_{P3}s)} \tag{A-3}$$

where

$$\tau_{P3} = R_{P3}C_3$$

and

$$\tau_{P4} = R_{P4}C_4$$

Figure A-5 depicts the gain adjustment circuit and has a relatively simple transfer function:

$$\frac{e}{e_1} = -\frac{R_{P6}}{R_{P5}} \tag{A-4}$$

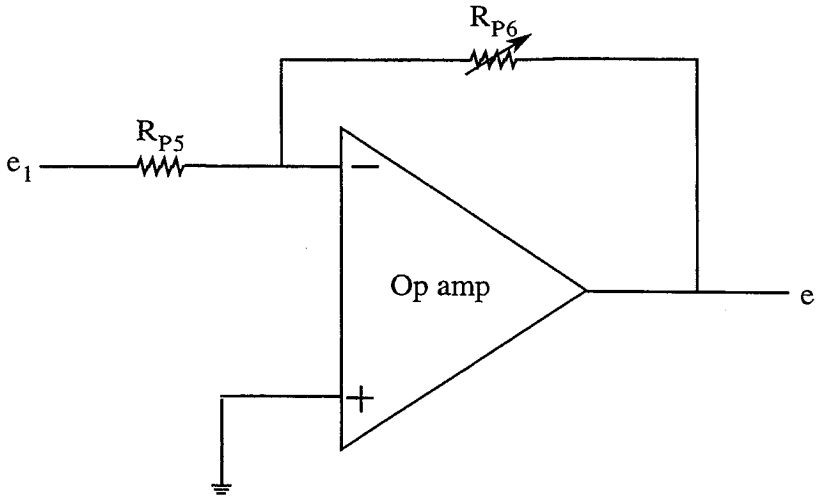

Figure A-5 Gain adjustment schematic

The transfer function for the plant, which includes the power amplifier, servomotor, dumbbell and encoder, was determined experimentally. A step input voltage was applied to the plant, and the response was measured via the encoder output which is shown in Fig. A-6. The gain and bandwidth can be calculated from the plot. First, the gain is found by dividing the steady output frequency (4.4 rad/sec) by the steady input voltage (0.4894 V) giving a value of K_P = 9.0 rad/sec/V. The bandwidth is calculated by measuring the rise time, t_{rise}, defined as the time the motor speed takes to increase from ten percent of the final value to ninety percent of the final value.[40] From Fig. A-6, t_{rise}= 2.45 s. The bandwidth of the plant is given as[41]:

$$\omega_P = \frac{0.7\pi}{t_{rise}} = 0.90\frac{rad}{sec}$$

Therefore, the transfer function of the plant is:

$$\frac{\omega_o}{e} = \frac{K_P}{(1 + \tau_P s)} \tag{A-5}$$

where

$$\tau_P = \frac{1}{\omega_P}$$

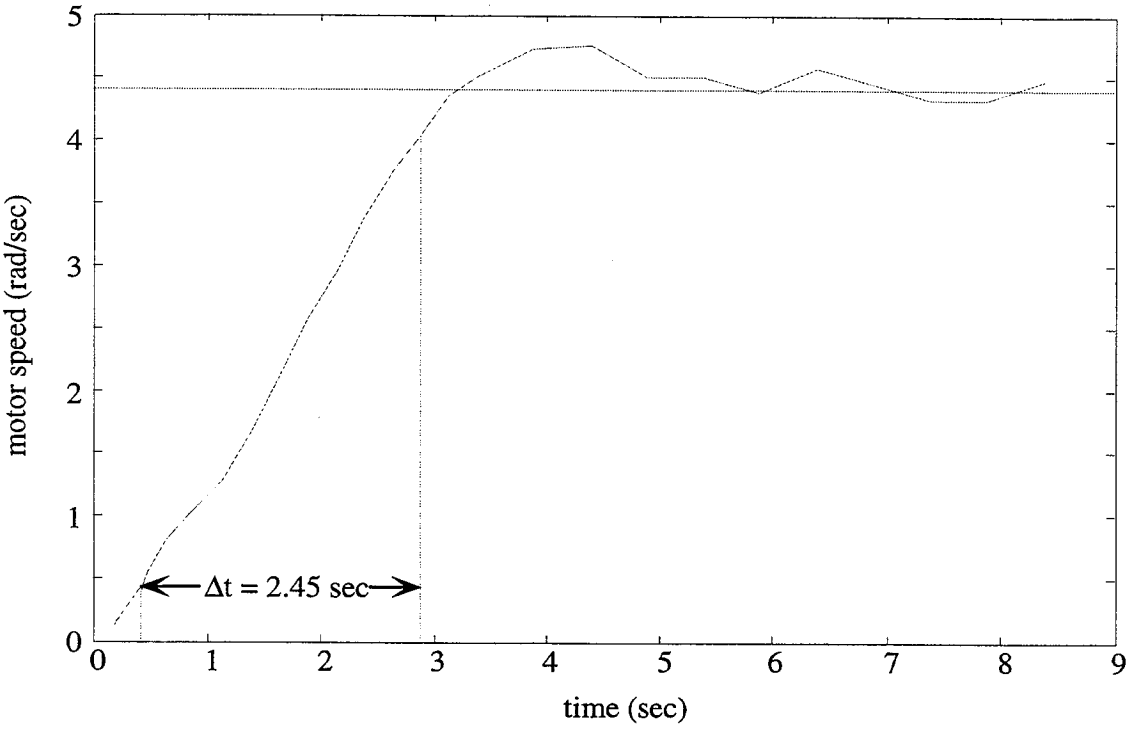

Figure A-6 Motor response to a step input of 0.4894 V at t = 0 sec.

Although the encoder is included in the plant, the integration performed by this device was negated by differentiating the data for ease of analysis. The integration must be re-introduced by including a 1/s term in the complete transfer function. By assembling the individual component transfer functions from Equ. (A-2) to Equ. (A-5) and including the integration at the end, the overall transfer function can be written as:

$$\frac{\Theta_o}{\Theta_i} = \left(\frac{D-U}{\Theta_i}\right)\cdot\left(\frac{e_0}{D-U}\right)\cdot\left(\frac{e_1}{e_0}\right)\cdot\left(\frac{e}{e_1}\right)\cdot\left(\frac{\omega_o}{e}\right)\cdot\left(\frac{\Theta_o}{\omega_o}\right)$$

$$= K_\phi \cdot \frac{1+\tau_{P2}s}{\tau_{P1}s\,(1+\tau_{LP}s)} \cdot \frac{C_3}{C_4}\frac{(1+\tau_{P4}s)}{(1+\tau_{P3}s)} \cdot \frac{R_{P6}}{R_{P5}} \cdot \frac{K_P}{(1+\tau_P s)} \cdot \frac{1}{s}$$

In Table A-1, the values of the PLL components can be found. After appropriate substitutions and rewriting in the root locus form, the transfer function becomes:

$$\frac{\Theta_o}{\Theta_i} = 0.196\,K\,\frac{(s+0.30)\,(s+416)}{s^2\,(s+0.90)\,(s+2.0)\,(s+119)} \qquad \text{(A-6)}$$

where

$$K = \frac{R_{P6}}{R_{P5}}$$

Table A-1 PLL component values

Component	Value	Comments
K_ϕ	0.12 V/rad	phase detector gain
K_P	9.0 rad/sec/V	plant gain
R_{P1}	200 Kohms	low-pass/charge pump resistor
R_{P2}	33.3 Kohms	low-pass/charge pump resistor
R_{P3}	4.99 Kohms	lag resistor
R_{P4}	51.1 ohms	lead resistor
R_{P5}	540 ohms	gain adjustment resistor

Table A-1 PLL component values

Component	Value	Comments
R_{p6}	26 Kohms ± 25 Kohms	gain circuit potentiometer in series with 1 Kohm resistor
C_1	0.168 μF	low-pass capacitor
C_2	100 μF	charge pump capacitor
C_3	100 μF	lag capacitor
C_4	47 μF	lead capacitor
Op amp	LM324N	quad operational amplifier

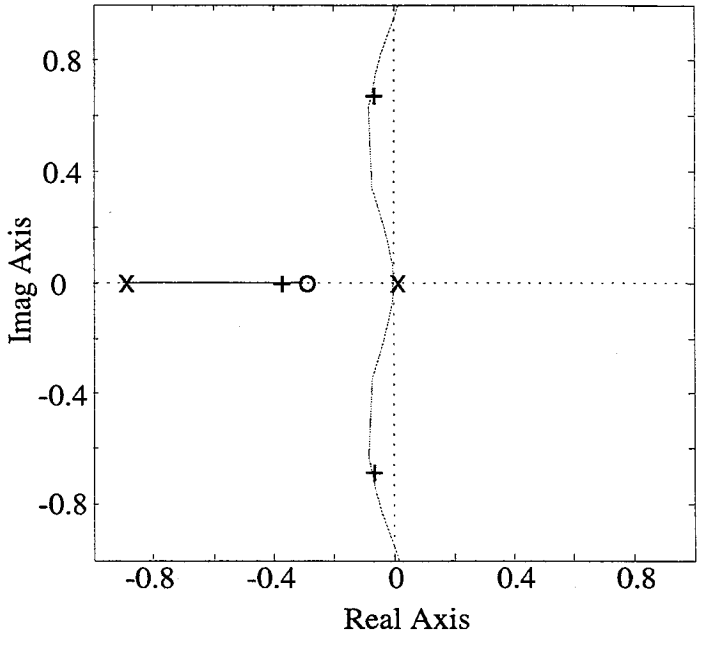

Figure A-7 Root locus of PLL transfer function

Using Equ. (A-6), the root locus of the system is plotted in Fig. A-7. Note that the scale of the plot has been reduced such that the region of interest about the origin is the only part of the graph that is displayed. The nominal operating point is shown by the '+' marks.

Along with the root locus plot, the Bode plots can also be examined. Figure A-8 shows both the magnitude and phase plots associated with the PLL with a root locus gain of 0.39, which is the nominal operating gain. The root locus reveals that the damping ratio is low with a value of approximately 0.12, and the natural frequency is about 0.66 rad/sec. These results are reflected in the Bode plots as well. The phase margin is only approximately 10° at a cross-over frequency of 0.67 rad/sec, indicative of small damping.

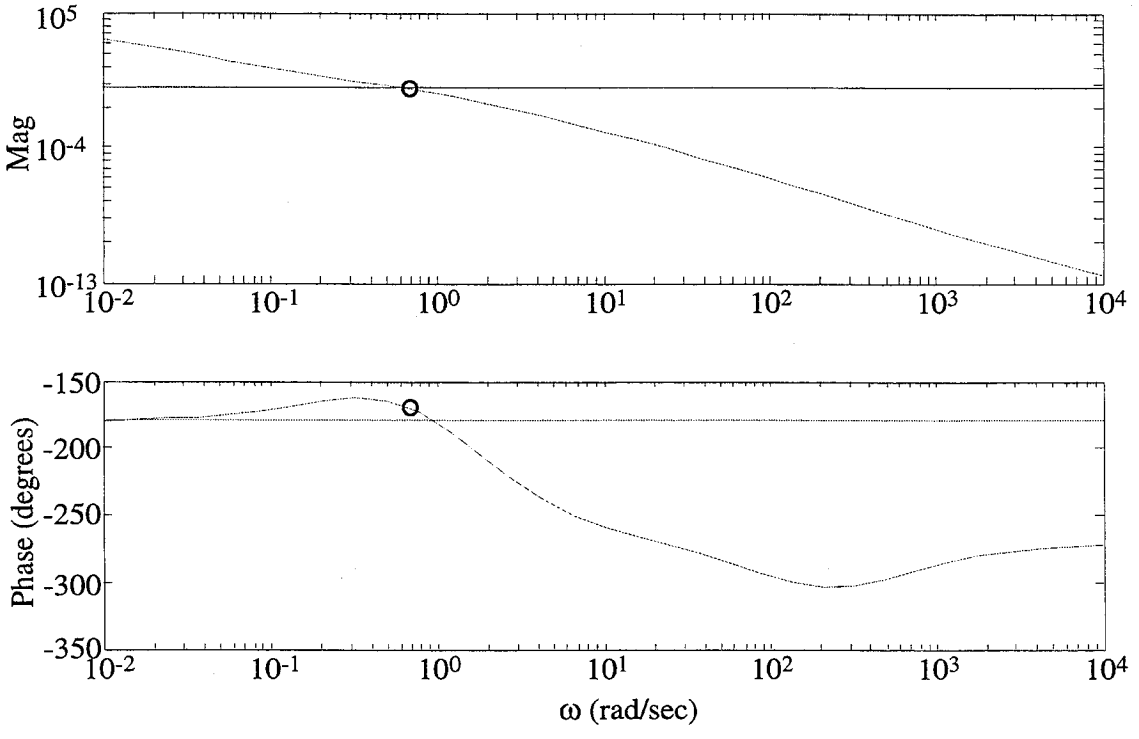

Figure A-8 Bode plot of PLL system with a root locus gain of 0.39

The design is a result of compromises between stability, speed of acquisition, and steadiness once the desired frequency is achieved. The final product proved to have small jitter with good reference frequency following characteristics as long as the change was done relatively slowly; i.e. no more than about 1.7 Hz (10.7 rad/sec) per minute.

Appendix B

Additional Steady Flow Experiments

There are three other experiments that show the continuation of the steady flow beyond a critical Re where periodic flow can exist. Two earlier experiments have critical Re estimates lower than the later experiment presented in § 4.2 (hence referred to as the Feb. 11 experiment) with a value between 2665 and 2775. These experiments were conducted before the dumbbell was attached to the motor shaft. The difference between these critical Re can mostly be attributed to the fluid temperature probe. In the earlier experiments, the thermistor used in the stationary endwall of the cylinder was a metal sheathed probe. The length of the sheath did not allow the whole probe to be immersed in the test fluid. Therefore, the temperature measured was not the fluid temperature, but rather a combination of the fluid and air bath temperatures. Although these temperatures are close, there is enough difference to affect the viscosity estimate. The sheathed probe was eventually replaced by an element probe covered by a small bead of epoxy which allowed complete immersion in the test fluid within the fill/drain hole. This technique enabled accurate measurements of the test fluid temperature, thereby giving a good estimate of kinematic viscosity.

The three experiments will be presented in chronological order with Re history graphs and images depicting the steady flow at the beginning and end of the observation period along with a sequence showing the unsteady flow with the same Re. One final image of steady flow at or just below the critical Re is shown last.

B.1 June 25, 1995 Experiment

Figure B-1 is the Re history of this experiment. The Re of the steady flow was slowly increased by 1.1 per minute and held at Re ≈ 2690 (Ω = 8.5264 rad/sec, ν = 28.99 cS) for approximately 7200 endwall rotations. Figure B-2 shows the steady flow at the start and end of the holding period. The second image shows the form of the azimuthal wave evident in the downstream fringes. As can be seen in Fig. B-1, the Re for this portion of the experiment drifted slowly upward from 2688 to 2695 due to a slow increase in the fluid temperature, which had a destabilizing affect on the steady flow. Also recall that the

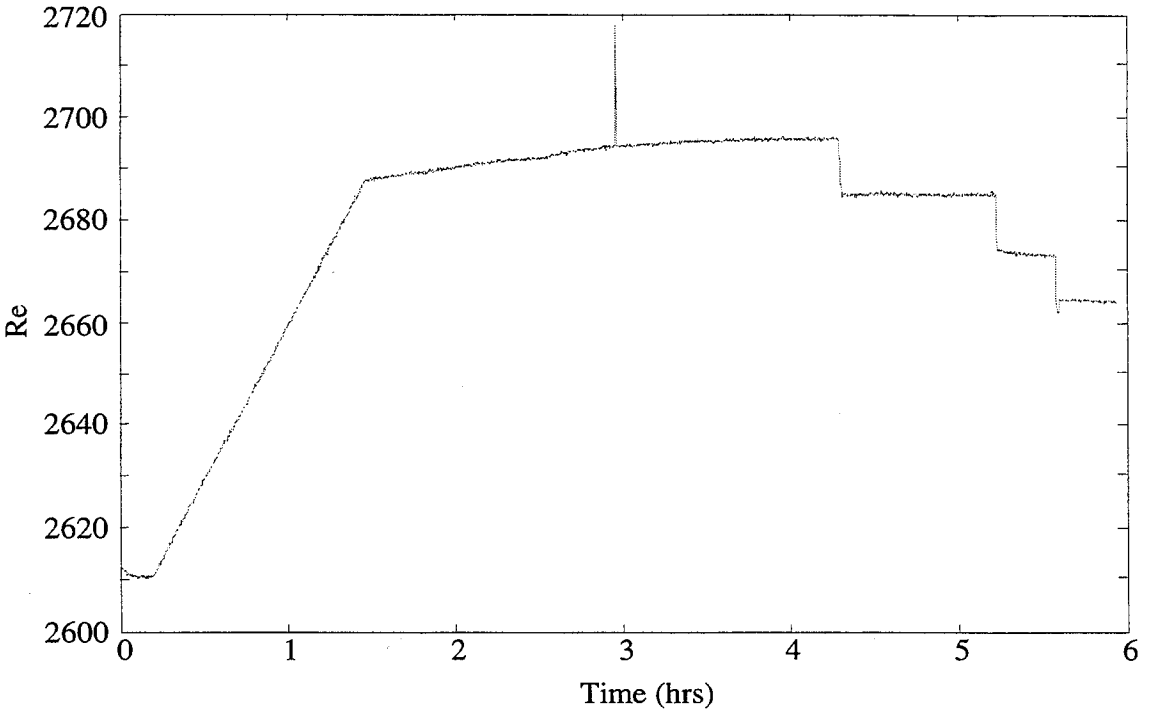

Figure B-1 Re history of June 25, 1995 experiment

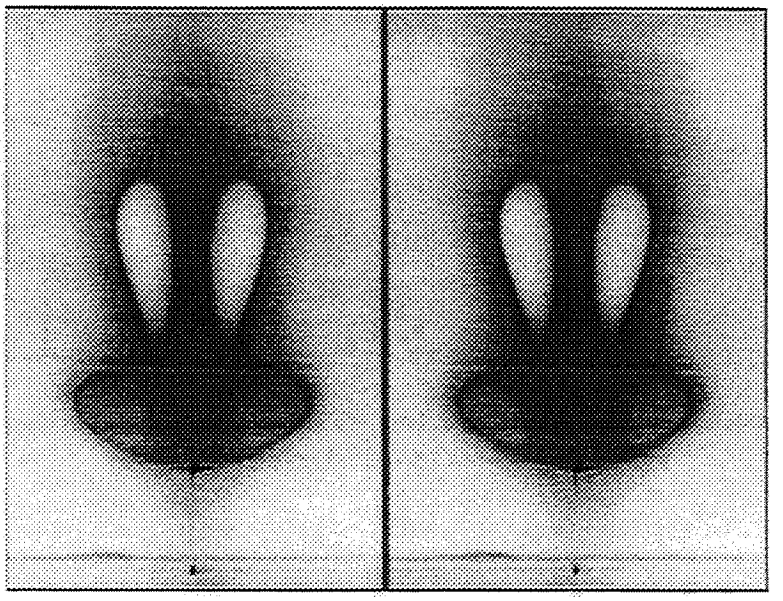

Figure B-2 Steady flow for Re ≈ 2690 (June 25, 1995)

dumbbell system had not been incorporated yet and the perturbations in Re due to disk speed fluctuations was an order of magnitude greater than the Re fluctuations during the Feb. 11 experiment.

Figure B-3 is a sequence of one complete period of the unsteady flow which was induced by applying a disturbance in Re from 2695 to 2720 and back to 2695. The unsteady flow at Re = 2695 was observed for 6425 endwall rotations after which the Re was reduced to 2685 (Ω = 8.4910 rad/sec, ν = 28.92 cS). Periodic flow at a Re of 2685 was recorded for 4700 endwall rotations. After reducing the Re to 2675 (Ω = 8.4561 rad/sec, ν = 28.91 cS), the periodic flow was observed for only 1810 endwall rotations before reducing the Re to 2665 (Ω = 8.4282 rad/sec, ν = 28.92 cS). After 1720 endwall rotations, the steady flow shown in Fig. B-4 was recovered.

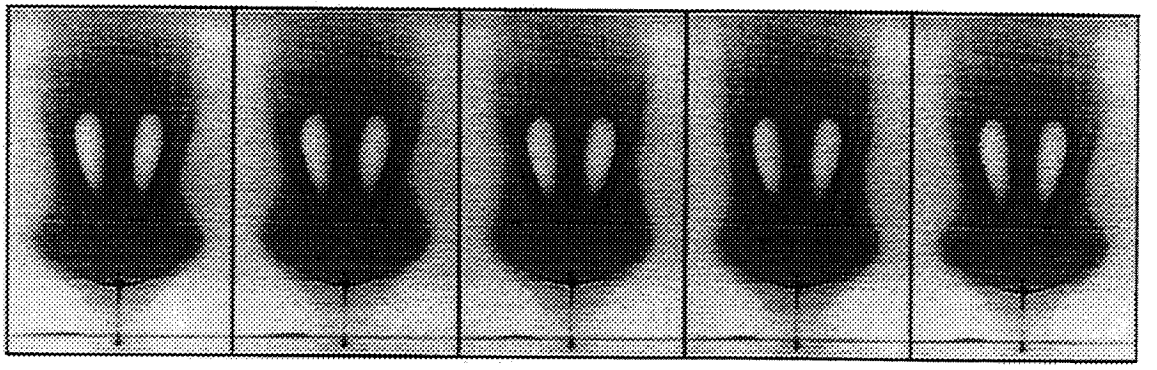

Figure B-3 Unsteady flow at Re = 2695. Images are equally spaced in time within a total period of 4.27 sec (τ = 36.4) (June 25, 1995).

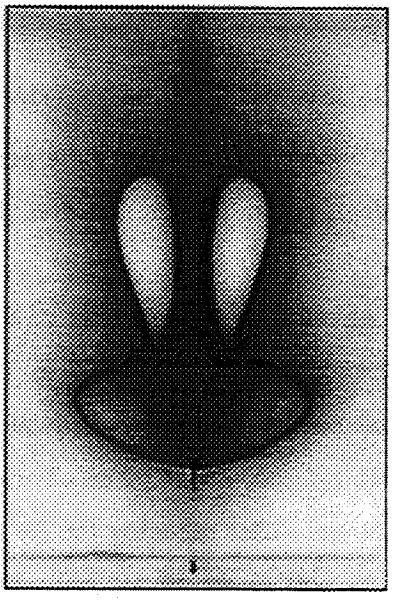

Figure B-4 Steady flow for Re = 2665 after 1720 endwall rotations (June 25, 1995).

B.2 July 9, 1995 Experiment

From the Re history shown in Fig. B-5, it can be seen that the Re was increased by 0.43 per minute until 2690 (Ω = 8.3390 rad/sec, ν = 28.35 cS) was achieved. Re control for this particular experiment was exceptional evidenced by the lack of drift during the constant Re periods. The steady flow was observed for 4800 endwall rotations at

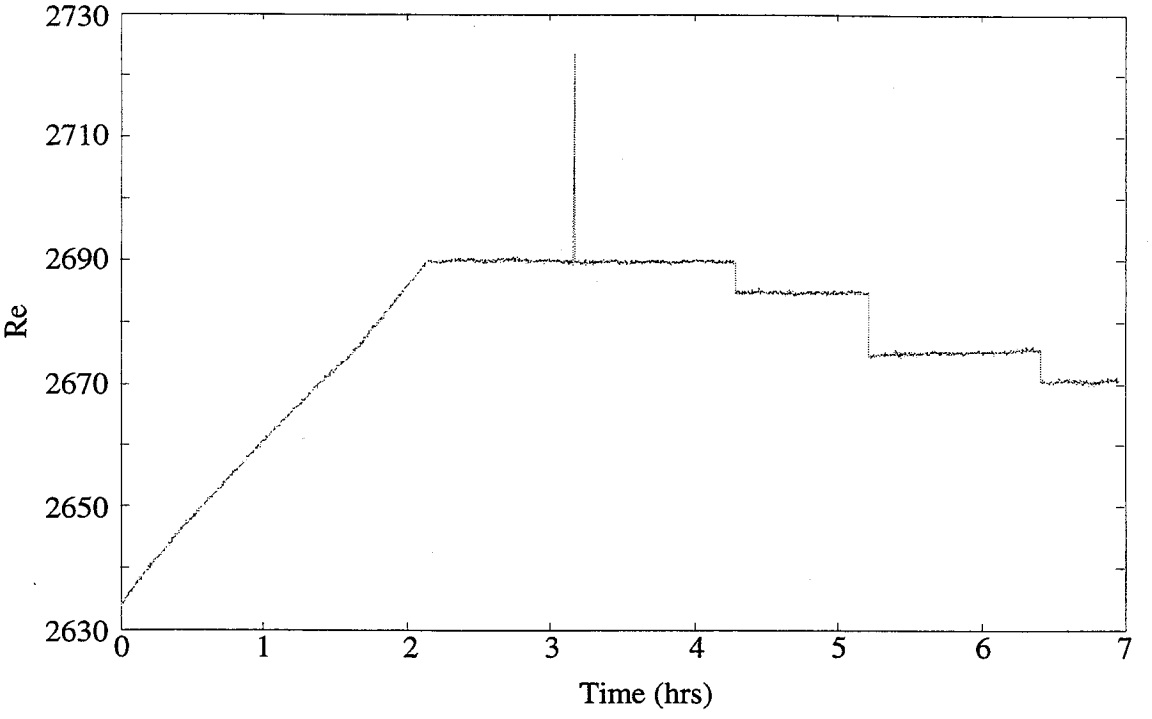

Figure B-5 Re history for the July 9, 1995 experiment.

Re = 2690, and the end points of this period are shown in Fig. B-6. After disturbing the flow with a momentary increase in Re to 2724, oscillations were observed for 5300 endwall rotations with a typical period shown in Fig. B-7. Periodic flow at Re = 2685 (Ω = 8.3196 rad/sec, ν = 28.34 cS) was allowed to develop for 4400 endwall rotations before the Re was reduced to 2675 (Ω = 8.2869 rad/sec, ν = 28.33 cS). Although the

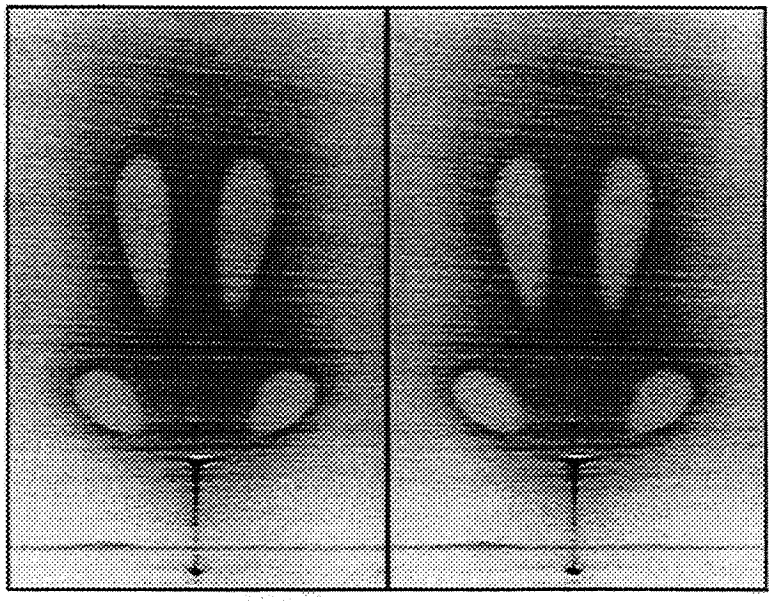

Figure B-6 Steady flow for Re = 2690 (July 9, 1995)

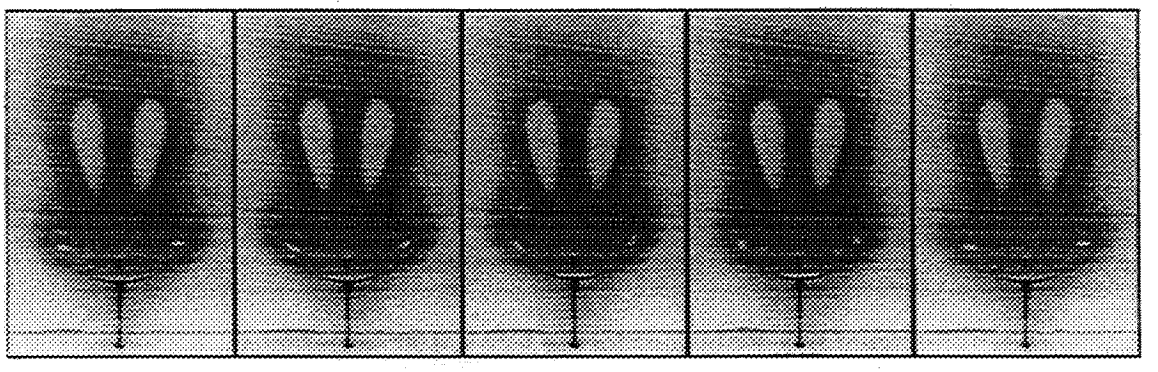

Figure B-7 Unsteady flow at Re = 2695. Images are equally spaced in time within a total period of 4.39 sec (τ = 36.6) (July 9, 1995).

motions were small towards the end of the period, oscillations were observed for 5600 endwall rotations at Re = 2675. Steady flow for Re = 2670 (Ω = 8.2693 rad/sec, ν = 28.32 cS) was achieved after approximately 2400 endwall rotations, and is shown in Fig. B-8.

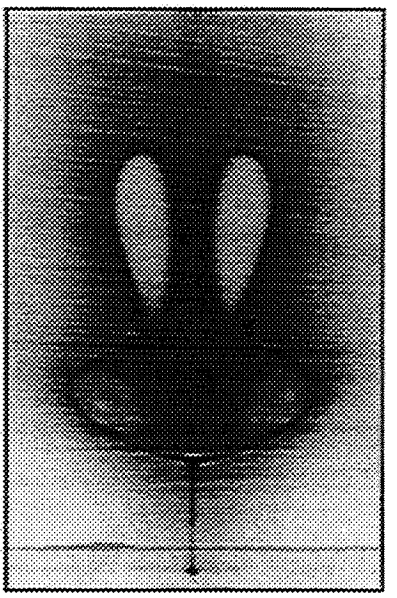

Figure B-8 Steady flow for Re = 2670 after 2400 endwall rotations (July 9, 1995).

B.3 February 7, 1996

Before this experiment was conducted, the dumbbell was incorporated into the PLL control system, and the sheathed thermistor probe was replaced with the element probe. Therefore, this experiment had less fluctuations in Re and better estimates of Re.

Figure B-9, the Re history, indicates that the Re was increased from 2658 to 2720 at a rate of 0.6 per minute. The steady flow at Re = 2720 (Ω = 9.2865 rad/sec, ν = 31.22 cS) was held for 5500 endwall rotations before being disturbed. Figure B-10 shows images from the beginning and end of the period. Towards the end of this period, significant azimuthal waves were present indicating that the limit of the basin of attraction of the steady flow was being approached. This was the reason that the Feb. 11, 1996 experiment (§ 4.2) was observed at a Re of 2715 instead of 2720.

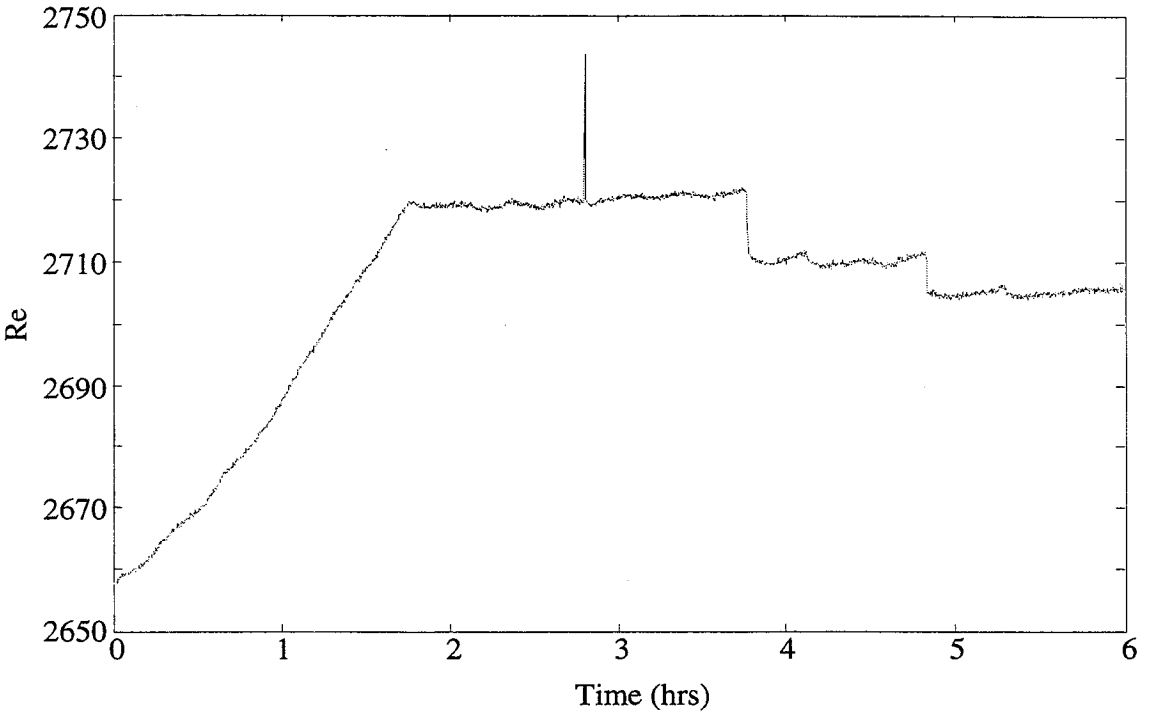

Figure B-9 Re history for the February 7, 1996 experiment.

After the 5500 endwall rotations with steady flow, the disturbance was applied with a momentary increase in Re to 2745. The periodic flow that ensued (Fig. B-11) was observed for 5000 endwall rotations before the Re was decreased to 2710 (Ω = 9.2243 rad/sec, ν = 31.13 cS). The periodic flow continued throughout the holding period of 5500 endwall rotations, but after reducing Re to 2705 (Ω = 9.1898 rad/sec, ν = 31.07 cS), the oscillations died out after approximately 6000 endwall rotations. The large number of endwall rotations required for steady flow (Fig. B-12) indicates that Re = 2705 is very close to the critical Re.

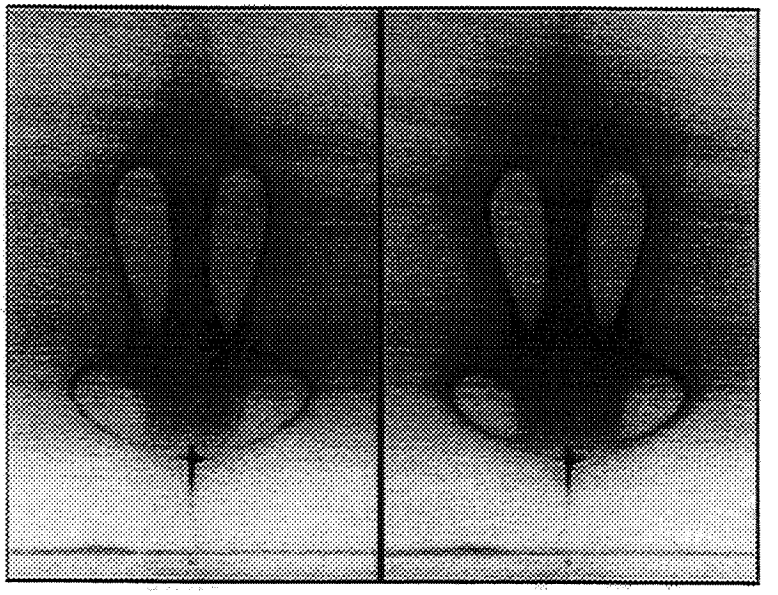

Figure B-10 Steady flow for Re = 2720 (February 7, 1996)

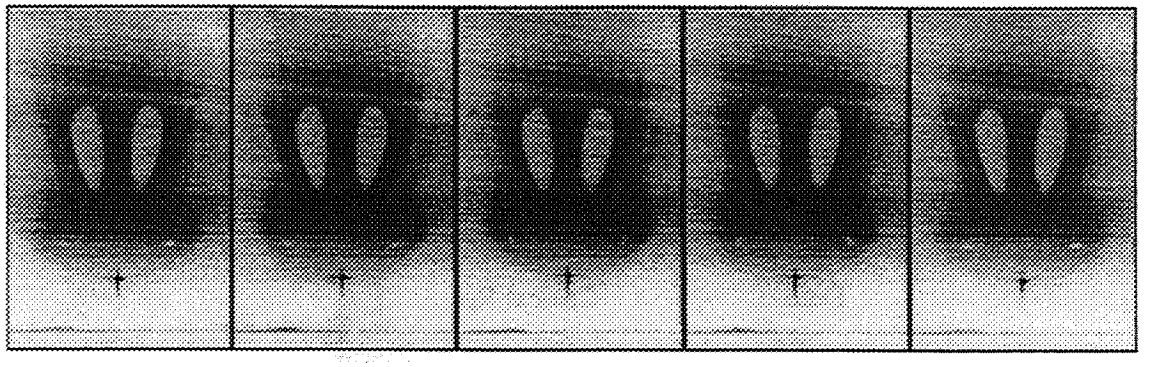

Figure B-11 Unsteady flow at Re = 2695. Images are equally spaced in time within a total period of 3.95 sec (τ = 36.6) (February 7, 1996).

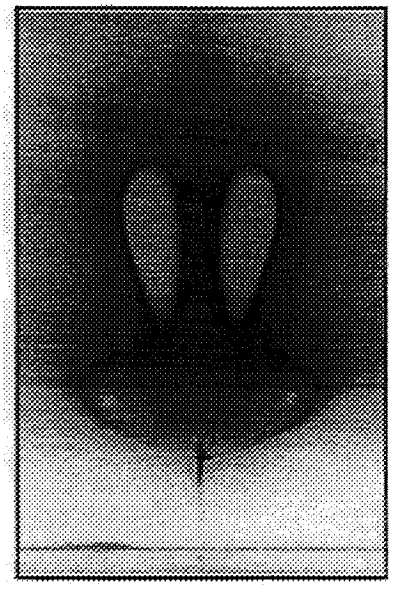

Figure B-12 Steady flow for Re = 2705 after 600 endwall rotations (February 7, 1996).

B.4 Summary of Experiments

Table B-1 Experiment results

Date	Critical Re	Highest Steady Re
June 25, 1995	$2665 < Re_c < 2675$	2690
July 9, 1995	$2670 < Re_c < 2675$	2695
February 7, 1996	≈ 2705	2720
February 11, 1996	$2702 < Re_c < 2705$	2715

Appendix C

Image Processing

There are two types of image processing used to present the data. First, a qualitative procedure is used to obtain the images shown in Chapter 4 and Appendix B. Second, a quantitative method is used to produce the signal and power spectral density (PSD) figures presented in Chapter 4.

C.1 Qualitative process

In order to present the most clear and easiest images to interpret without resorting to invasive enhancements, several video frames are used for each image. While invasive enhancements rely on the interpretation of a video, a composite image of several frames naturally brings out hard-to-see detail. Each individual frame contains information, but since the data is from a low light video, it is inevitable that some of the detail will be missed. The interpreter, who must judge which areas of the image to highlight or de-emphasize, is taken out of the process. The frame overlaying method can be tailored such that each frame enhances the whole image, building up detail where appropriate. Depending on the particular circumstances of an image, the number of frames used to create the image is varied. For very low light, up to thirty frames are used; whereas for brighter pictures, five frames may be enough to produce high quality images. In some cases, the dye contaminates the experiment to a degree that precludes sharp detail, i.e. Fig. B-11 from the February 7, 1996 experiment.

For the steady images, frames are chosen at random to form a complete image. The periodic images require overlaying frames depicting the same phase of the oscillation. Some images, though, only contain one frame because of the quasi-periodic nature of the flow. The result of the quasi-periodic oscillations is that each frame is unique, and combinations of frames would produce confusing ghost images. Figure 4-13 and 4-20 are sequences of quasi-periodic flows made of individual frames.

C.2 Quantitative process

To create the signal and PSD figures in Chapter 4, the periodic flow video must be quantified. By using a video capture board, sequential, evenly timed frames are digitized. Also, instead of capturing the entire frame, which significantly reduces the frame rate and length of record, a region of interest about the stagnation point and injection port is selected.

Once the frames have been collected, they are cross-correlated with a reference frame, which is the first frame of the sequence. In a correlation, the location of a prominent feature, i.e. the dye line emanating from the injection port and ending at the stagnation point, is calculated. The cross-correlation compares the difference of the clustering location between two data sets. Therefore, a cross-correlation performed on the periodic flow will reveal how the dye line moves from frame to frame.

A PSD analysis of the signal obtained from the cross-correlation will show which frequencies contain the most power, which signify the prominent modes of oscillation. The PSD is calculated by taking the fast Fourier transform (FFT) of the signal data and multiplying by the complex conjugate of the FFT, then dividing by the length of the FFT, which should be a power of two. Windowing of the data is important to prevent the folding back of higher frequencies into the domain of interest.[42] Also, care must be taken in generating the proper frequency scale by taking into account the sample rate at which the original signal was captured.

A certain amount of error is introduced into these data capturing techniques, especially due to the slightly non-uniform dye injection, which causes discrepancies in the calculated position of the dye line. As the Re is increased, especially through quasi-periodic regimes, the technique becomes less accurate. But, overall, the method proved adequately robust for the purposes of mode identification.

Bibliography

[1] G.L. Brown and J.M. Lopez, "Axisymmetric vortex breakdown. Part 2. Physical Mechanisms", J. Fluid Mech., *221*, pp 553-576 (1990)

[2] J.P. Smart and R. Weber, "Reduction of NO_x and optimisation of burnout with an aerodynamically air-staged burner and an air -staged precombustor burner", J. Inst. Energy, pp. 237-245 (1989)

[3] R.-H. Chen and J.F. Driscoll, "The role of the recirculation vortex in improving fuel-air mixing within swirling flames", Twenty-Second Symp. (Intern'l) on Comb./The Comb. Inst., pp. 531-540 (1988)

[4] M. Van Dyke, An Album of Fluid Motion, The Parabolic Press, Stanford, CA (1982)

[5] D.H. Peckham and S.A. Atkinson, "Preliminary results of low speed wind tunnel tests on a gothic wing of aspect ratio 1.0", A.R.C. Technical Report C.P. No. 508, TN No. Aero. 2504 (1957)

[6] J. K. Harvey, "Some observations of the vortex breakdown phenomenon", J. Fluid Mech., *14*, pp. 585-592 (1962)

[7] I. Gursul and H. Yang, "On fluctuations of vortex breakdown location", Phys. Fluids, *7*, 229, (1995)

[8] M.P. Escudier and J.J. Keller, "Recirculation in Swirling Flow: A Manifestation of Vortex Breakdown", AIAA Journal, *23*, No. 1, pp. 111-116 (1985)

[9] H.B. Squire, "Analysis of the 'vortex breakdown' phenomenon, Part 1", Imperial College of Sci. and Tech. Dept. of Aero. Rep. no. 102 (1960)

[10] S. Leibovich, "Vortex stability and breakdown: survey and extension", AIAA Journal, *22*, pp. 1192-1206 (1983)

[11] M.P. Escudier, "Observations of the flow produced in a cylindrical container by a rotating endwall", Experiments in Fluids, *2*, pp. 189-196 (1984)

[12] M.P. Escudier, "Vortex Breakdown: Observations and Explanations", Prog. Aerospace Sci., *25*, pp. 189-229 (1988)

[13] H.J. Lugt and M. Abboud, "Axisymmetric vortex breakdown with and without temperature effects in a container with a rotating lid", J. Fluid Mech., *179*, pp. 179-200 (1987)

[14] N.C. Lambourne and D.W. Bryer, "The bursting of leading-edge vortices — some observations and discussion of the phenomenon", Aeronautical Research Council, Reports & memoranda R. & M. No. 3282, pp. 1-36 (1961)

[15] M.G. Hall, "Vortex Breakdown", Annual Review of Fluid Mechanics, *4*, pp. 195-218 (1972)

[16] G. P. Neitzel, "Streak-line motion during steady and unsteady axisymmetric vortex breakdown", Phys. Fluids, *31*, 958, (1988)

[17] K. Hourigan, L. J. W. Graham and M. C. Thompson, "Spiral streaklines in pre-vortex breakdown regions of axisymmetric swirling flows", Phys. Fluids, *7*, 3126, (1995)

[18] H.U. Vogel, "Experimentelle Ergebnisse über die laminare Strömung in einem zylindrischen Gehäuse mit darin rotierender Scheibe", Max-Planck-Inst. für Strömungsforschung, Bericht 6/1968 (1968)

[19] B. Ronnenberg, "Ein selbstjustierendes 3-Komponenten-Laserdoppleranemometer nach dem Vergleichstrahlverfahren, angewandt für Untersuchungen in einer stationären zylindersymmetrischen Drehströmung mit einem Rückstromgebiet", Max-Planck-Inst. für Strömungsforschung, Bericht 20/1977 (1977)

[20] H. J. Lugt and H. J. Haussling, "Axisymmetric Vortex Breakdown in Rotating Fluid Within a Container", Journal of Applied Mechanics, *49*, pp 921-923, (1982)

[21] J. N. Sorensen and O. Daube, "Direct simulation of flow structures initiated by a rotating cover in a cylindrical vessel", In *Advances in Turbulence*, H. H. Fernholz & H. E. Fielder, pp. 383. Springer (1989)

[22] J.M. Lopez, "Axisymmetric vortex breakdown. Part 1. Confined swirling flow", J. Fluid Mech., *221*, pp. 533-552 (1990)

[23] O. Daube, "Numerical simulations of axisymmetric vortex breakdown in a closed cylinder", Lectures in Applied Math., *28*, 131 (1991)

[24] J.M. Lopez and A.D. Perry, "Axisymmetric vortex breakdown. Part 3. Onset of periodic flow and chaotic advection.", J. Fluid Mech., *234*, pp. 449-471 (1992)

[25] N. Tsitverblit, "Vortex breakdown in a cylindrical container in the light of continuation of a steady solution", Fluid Dynamics Research, *11*, pp. 19-35 (1993)

[26] J.M. Lopez, "Note on the Nature of the Onset of Periodic Flow in an Enclosed Cylinder with a Rotating Endwall", Penn State Dept. of Math., Report No. AM131 (1993)

[27] J. N. Sørensen and E. A. Christensen, "Direct numerical simulation of rotating fluid flow in a closed cylinder", Phys. Fluids, *7*, 764, (1995)

[28] A. Yu. Gelfgat, P. Z. Bar-Yoseph and A. Solan, "Stability of confined swirling flow with and without vortex breakdown", J. Fluid Mech., *311*, 1 (1996)

[29] T. B. Benjamin, "Bifurcation phenomena in steady flows of a viscous fluid I. Theory", Proc. R. Soc. Lond. A, *359*, pp. 1-26, (1978)

[30] T. B. Benjamin, "Bifurcation phenomena in steady flows of a viscous fluid II. Experiments", Proc. R. Soc. Lond. A, *359*, pp. 27-43, (1978)

[31] Omega Engineering, Inc., The Temperature Handbook, (1992)

[32] N.K. Sinha and N.H. Bailey, "Speed Control of a DC Servomotor Using Phase-Locked Loop: Some Test Results of a Practical Design", IEEE Transactions, *IECI-23*, No. 1, pp. 22-26, (1976)

[33] A.W. Moore, "Phase-locked loops for motor-speed control", IEEE Spectrum, April (1973)

[34] J. P. Holman, Experimental Methods for Engineers, McGraw-Hill Book Company, (1984)

[35] V. Rom-Kedar, A. Leonard and S. Wiggins, "An analytical study of transport, mixing and chaos in an unsteady vortical flow", J. Fluid Mech., *214*, 347, (1990)

[36] J. L. Stevens, J. M. Lopez, and B. J. Cantwell, "Periodic flow states in an enclosed cylinder with a rotating endwall", Phys. Fluids (to be submitted 1996)

[37] J. M. Lopez, "Unsteady vortex breakdown in an enclosed cylinder flow", Tenth Australasian Fluid Mechanics Conference, University of Melbourne, December 1989, Paper 9A-1 (1989)

[38] P. G. Drazin and W. H. Reid, Hydrodynamic stability, Cambridge University Press, (1981)

[39] J. M. Lopez, Private communication, Jan. 1996.

[40] J. J. D'Azzo and C. H. Houpis, Linear Control System Analysis and Design: Conventional and Modern, Third Edition, McGraw-Hill, p. 90 (1988)

[41] J. K. Roberge, Operational amplifiers : theory and practice, Wiley, p. 95 (1975)

[42] W. H. Press, B. P. Flannery, S. A. Teukolsky, and W. T. Vetterling, Numerical Recipes, the Art of Scientific Computing (FORTRAN Version), Cambridge University Press, pp. 423-429 (1989)